ABSTRACT

Title: FIN-GUIDED FUEL INJECTION
ENHANCEMENTS FOR LOW ASPECT
RATIO SCRAMJET COMBUSTORS

Rama Ashok Balar, Master of Science, 2007

Directed By: Associate Professor, Dr. Kenneth H. Yu,
Department of Aerospace Engineering

Characterization of a three-dimensional Mach 2 scramjet combustor with aspect ratio one has been conducted in order to provide baseline performance data. The maximum combustion performance was achieved at an equivalence ratio of 0.25 due to poor mixing. Subsequent fuel injection studies investigated transverse and ramped parallel mixing schemes in a Mach 2 duct. It was shown ramped injection required too high of flow blockage to be practical for efficient mixing. From these studies a new Fin-Guided fuel injection technique was established. Substantial improvement in mixing performance was observed through pressure traces, Schlieren and Mie-scattering.

With the use of Fin-Guided Injection the fuel penetration height was increased by 100~120% and the flow losses associated with jet-induced shocks were reduced by 13~30% over injection without a fin. The results open up the possibility of further increasing performance by optimizing the fin height and the fuel injection angle behind the fin.

FIN-GUIDED FUEL INJECTION ENHANCEMENTS FOR LOW ASPECT RATIO SCRAMJET COMBUSTORS

By

Rama Ashok Balar

Thesis submitted to the Faculty of the Graduate School of the
University of Maryland, College Park, in partial fulfillment
of the requirements for the degree of
Master of Science
2007

Advisory Committee:
    Dr. Kenneth Yu, Chair
    Dr. Ryan P. Starkey
    Dr. Ryan P. Starkey

DEDICATION

To my friends and family.

ACKNOWLEDGEMENTS

I would like to first acknowledge my advisor Dr. Ken Yu, for his guidance and instruction throughout my undergraduate and graduate career. As well as my committee members Dr. Christopher Cadou and Dr. Ryan P. Starkey, their input and advice was paramount to the completion of my thesis. I would also like to acknowledge Dr. Bin Pang and Gregory Young for the continued help throughout my graduate studies. The assistance my lab mates and office mates provided me also played a large role in my success as a graduate student.

Finally would like to acknowledge the funding which made this research possible. This work has been sponsored by the Maryland Industrial Partnership Program and the Space Vehicle Technology Institute, under grant NCC3-989, one of the NASA University Institutes, with joint sponsorship from the Department of Defense. Additional funding was provided by the Office of Naval Research grant N000140110698. Appreciation is expressed to Claudia Meyer, Mark Klem, and Harry Cikanek of the NASA Glen Research Center, Dr. John Schmisseur and Dr. Walter Jones of the Air Force Office of Scientific Research, and Dr. Gabriel Roy of the Office of Naval Research.

TABLE OF CONTENTS

LIST OF TABLES

LIST OF FIGURES

TABLE OF NOMENCLATURE

A	Area
a	Speed of sound
b	channel height
CH*	CH radical
Const	Arbitrary constant
C_2*	Dicarbon radical
C_δ	Change in shear layer growth
$(C_\delta)_0$	Change in shear layer growth for incompressible shear layer
d	injection diameter
h	Characteristic height
J	Transverse jet injection parameter
ℓ	Fin length
M	Mach number
$\dot{m}$	Mass flow
P	Pressure
s	entropy
T	Temperature
U,V	Velocity
W	Fin width
x/d	Normalized distance downstream
y/d	Normalized height
z/d	Normalized width
Greek Symbols	
β	Wave Angle
γ	Ratio of specific heats
δ_m, δ'	Shear layer height
δ_0	Shear layer height, incompressible flow
η_A	Fuel-area efficiency
η_h	Penetration height efficiency
ρ	Density
Δu	Change in velocity
ϕ	Equivalence ratio
Acronyms	
CAD	Computer Aided Drawing
CFD	Computational Fluid Dynamics
EISP	Estimated specific impulse
HTHL	Horizontal Take-off Horizontal Landing
ICCD	Intensified Coupled Charged Device
NPT	Normal Pipe Thread
RBCC	Rocket Based Combined Cycle
SSTO	Single Stage to Orbit

TCP/IP	Transmission Controlled Protocol/Internet Protocol
TPS	Thermal Protection System
VI	Virtual Interface
VTHL	Vertical Take-off Horizontal Landing
2D	Two-dimensional
3D	Three-dimensional
<u>Subscripts</u>	
air	Air
c	Convective
f,fuel	Fuel
IT	Inward turning
m	Mixing
n	Normal
o	Freestream condition
s	Shock
sep	Separated
t	Throat
w	Wall
0	Stagnation/total condition
1	Properties upstream of a shock
2	Properties downstream of a shock
∞	Freestream condition

1 Introduction

1.1 Background and Motivation

The development of safe, affordable, reliable and reusable launch vehicles will usher in an age which will unlock the vast potential of space. Space travel will become routine and intercontinental travel will be as easy intercity travel is today.[1] Only when a system which is orders-of-magnitude safer and more affordable than current space launch methods is devised will this vision be realized. As rocket-powered vehicles are approaching their limit in terms of these parameters, switching to airbreathing launch systems is the only way to achieve significant improvements.[2] On March 27th, 2004 NASA's X-43 successfully flew, under its own power, at Mach 6.83 and then Mach 9.68 in second test later the same year. Thus becoming the first airbreathing vehicle to break the hypersonic barrier, proving that scramjet (supersonic combusting ramjet) powered vehicles can meet the performance demands of next generation air vehicles.[1] The scramjet's potential to reach near orbital speeds has always brought attention to hypersonic cruise missions and, in particular, the elegant yet elusive single-stage-to-orbit (SSTO).[3] However on the path to this ultimate application the X-43 is only one small step.[1]

In order to use airbreathing hypersonic flight to usher in a new age of transportation and space travel many unresolved issues must be addressed. Effective performance at hypersonic Mach numbers demands the highest component efficiencies, which have not yet been obtained.[3] It is the drive of this work to understand mechanisms of combustor efficiency and to introduce methods by which to increase it; mainly by enhancing mixing.

1.1.1 Scramjet Development

In the late 1950s various papers[4,5] were published reviewing the history of conventional ramjets and exploring new methods to increase airbreathing flight speeds; leading to the concept of a supersonic combustion ramjet or scramjet. The first concept of supersonic combustion was introduced by Roy[6] in 1946 when he proposed the possibility of directly adding heat to a supersonic stream by means of a standing wave. Ferri[7] and Ferri, et al.[8] validated Roy's theory by accomplishing steady combustion in a Mach 3.0 supersonic stream, without strong shocks and easily emerged as the major leader in exploring scramjet technology in the United States during the 1960s.[9] Contemporaries of Ferri, Weber and MacKay[10] pointed out the superiority of scramjet engines over conventional ramjets with flight speeds in excess of Mach 7 and were able to anticipate major hurdles in the development of scramjet technology. Weber and MacKay[10] listed fuel injection and mixing without severe shock loses, combustor gasdynamics, wall cooling, frictional losses and nozzle performance as complications involved with supersonic combustion. Druger[11] listed similar issues as Weber and MacKay[10] including the need for a diverging combustor shape to avoid thermal choking from heat addition as found in constant area ducts.

More than 40 years after the introduction of scramjet technology, the problems outlined early in its history still plague its development. Shortcomings in the ability to control heating problems and the performance of combustors are a crippling hindrance in the design progress. Curran[9] points out that the hypersonic airbreathing community has come to generally accept the 2D airframe-integrated lifting body configuration in which these problems seem currently unsolvable. Billig[12] has pointed out that examining the possibility of a radical change in the engine flow path and, in turn, the overall vehicle configuration could produce a vehicle which addresses and eliminates these problems.[9] Billig[13] has presented alternate vehicle configurations derived from the streamline tracing of inward turning flowfields as one such radical design change. Such vehicles are generally referred to as “inward turning” and promise to potentially reduce drag and heating loads while increasing the overall engine efficiency.

1.1.2 Inward-Turning Concepts

Vehicle geometries produced by carving out an airframe using the streamsurfaces of a known flowfield are known as inward turning.[14] Inward turning inlets were first proposed by Busemann in 1942, when he called for a three dimensional axisymmetric isentropic surface to produce a uniform exit flow after a standing conical shock. Busemann first defined the exit flow, and then numerically integrated the isentropic surfaces in reverse by exploiting the hyperbolic nature of the supersonic flow.[15] The inverse design provides excellent total pressure recovery, low pressure drag, and a low aspect ratio exit, making it ideal for supersonic combustion applications.[16] However, the complexity of analytical solutions and high computational design effort compared to two dimensional, 2D, ramp and axisymmetric designs has restricted exploration of inward turning designs.[17-19]

Traditional wedge derived wave riding designs for hypersonic vehicles utilize two dimensional flow paths to take advantage of theoretical two dimensional uniform flows through the inlet. These designs reduce the complexity of computing hypersonic flow fields, manufacturing and have good on-design characteristics, making them the current frontrunner for hypersonic vehicle design. However, their two dimensional nature create large aspect ratio inlets which in turn result in large aspect ratio combustors. These combustion chambers thus have large surface areas for thermal conduction and require thermal protection which adds significant mass to a vehicle. Inward turning designs address this problem.

The exit perimeter of an inward turning inlet will always be smaller than that of a standard 2D inlet given similar contraction ratio and capture aspect ratio; thus resulting in a smaller area requiring thermal protection.[20] Figure 1.1 shows two SSTO configurations with actively cooled areas shaded in red. The vehicle on the left is a standard 2D lifting body design, while the vehicle on the right is an inward turning vehicle designed by Kothari, et al.[21] Work done designing other inward turning vehicles have come to similar findings.[22,23]. The difficulties associated with thermal management grow exponentially, as does the severity of the thermal environment, as aircraft speeds increase beyond the supersonic range and into the hypersonic regime. Van Griethuysen, et al.[24] and Billig[13] have shown that the cooling systems required to manage the heat loads at these velocities can significantly influence the overall performance and operability of the aircraft.

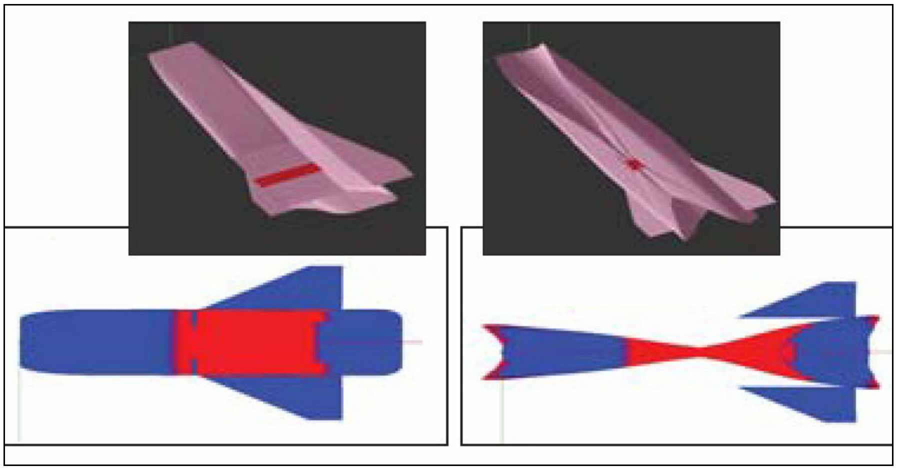

Figure 1.1: Two dimensional and inward turning SSTO vehicle configurations (from Kothari[21]).

As flight mach numbers increase past Mach 4 the ambient air temperature relative to the aircraft is too hot to utilize ram air as an effective cooling mechanism.[24] Even when designs are considered for the lower end of the hypersonic realm, in the range of Mach 6-8, these material limits and thermal protection are major concerns. One specific location of concern is the isolator and combustor as airflow with already high static temperatures, above approximately 900K, is reacting exothermically with fuel being injected. The need to cool the surface walls of the combustor can become a very demanding requirement as flight Mach numbers increase. Conservative estimates have predicted that the fuel cooling requirements (for a fuel cooled system) will exceed the combustion requirements of the system by as much as 4 times for a Mach 20 flight system, meaning that 4 times as much fuel is required for cooling as is required to power the vehicle.[24] Naturally this increase of needed fuel flow along with the associated plumbing and systems will dramatically affect the flight weight of such a system or drastically reduce the range.

With its smaller inlet exit perimeter (i.e. combustor entrance) the inward turning SSTO design has been shown to halve the heat load of a comparable rocket based combine cycle (RBCC) vehicle using a 2D inlet.[21,25] This reduction in heating load has been shown to result in on-design EISP increase of 200-400s, approximately 2 Mach number increase in maximum speed, and a 30% decrease in empty and gross vehicle weight over vehicles employing equivalent two-dimensional compression.[21,25] Analysis of other vehicle configurations such as HTHL and VTHL also show inward turning inlets yielding vast improvements over 2D inlets, primarily due to this lower heat load.[26]

While evidence is mounting that Inward turning designs can provide vast improvements over two-dimensional designs, they have yet to be embraced, as the only proof in the greater performance is provided by analytical tools.[27] Many assumptions are made when developing computational models of hypersonic vehicles, particularly within the combustor and the designers of models are beginning to question themselves.[27,28] Often quasi-one-dimensional and simplified chemical kinetics are required to reduce the computational demands associated with reaction chemistry. CFD models based on the Reynolds averaged Navier-Stokes equations use models for turbulent fluxes that employ many ad hock assumptions and empirically determined coefficients.[29] Although required to make the computational problem tractable, these simplifications often reduce the accuracy of the model. Furthermore the large number of adjustable parameters typically leads to a low confidence in the models prediction when they are applied to classes of flows for which they have not been experimentally validated. An example of these issues is documented by Cutler, et al.[29,30] where computational models fail to fully correspond to measurements of the combustion of hydrogen fuel made under flight enthalpy conditions in NASA Langley's Direct-Connect Supersonic Combustion Facility. Their calculation underestimated the length of the ignition region and indicated that there were problems with uncertainty in their kinetics model and/or a need to account for turbulence-chemistry interactions. These errors are a major motivator in acquiring empirical data, both for CFD validation and general characterization of supersonic combustion systems.

Zang[31] had attempted to generate a baseline characterization of the combustion in a supersonic duct with an aspect ratio of one. This characterization was to serve as the benchmark against which the testing of combustion configurations developed by novel vehicle designs, specifically those produced by the inward turning designs, could be compared. The work was incomplete and was resumed by this author in order to accomplish the tasks originally set.

Another difficulty with inward turning designs is fuel injection within the combustor. Scramjet combustor design requires development of a fuel injection system that can rapidly mix fuel while permitting sufficient fuel residence times to achieve ignition.[32] This process must be coupled with the engine inlet system, such that the pressure rise due to the combustion and fuel injection process does not lead to engine unstart. However, the low aspect ratio design that reduces total temperature loading by minimizing the total surface area and exit perimeters also increases the amount of fuel penetration needed to provide uniform fuel injection. Figure 1.2 shows the respective penetration heights required in 2D and inward turning combustors with the same area.

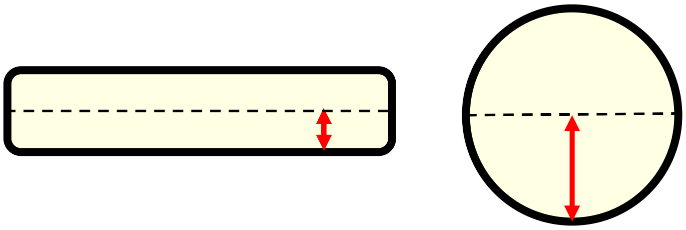

Figure 1.2: Penetration heights for 2D and inward turning combustors.

The penetration height required for the inward turning design is significantly greater than that of the 2D design. As the aspect ratio of the 2D design is increased, the disparity becomes more evident. Assuming a circular combustor cross section with aspect ratio one for the inward turning design, the of fuel penetration height and perimeter ratios between inward turning and 2D designs are shown in Figure 1.3. As the 2D combustor aspect ratio is increased, the relative penetration height for the inward turning (IT) design grows significantly, following the h_{IT}/h_{2D} (inward turning penetration height over 2D penetration height) curve. The figure also demonstrates how inward turning designs have increasingly smaller perimeters over 2D designs.

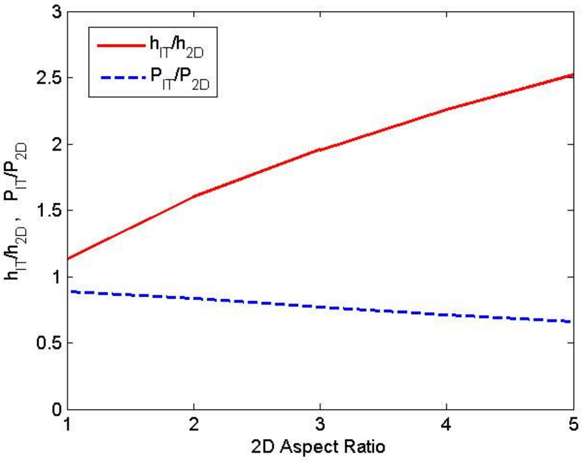

Figure 1.3: Ratio of penetration heights and perimeter of inward turning designs over 2D combustor designs.

It is clearly much more difficult to provide uniform mixing in an inward turning combustor than with a 2D design. If the same techniques are used to inject fuel into a low aspect ratio combustor as in a 2D combustor, the pressure rise would be too great, and efficiencies would suffer. Before any of the benefits of an inward turning scramjet can be realized the mixing issue must be addressed. This work attempts to provide a new and effective way to inject fuel in supersonic streams as applicable in an inward turning design.

1.2 Objectives

There are two areas of interest in this investigation: the characterization of supersonic combustion in a diverging duct with an aspect ratio of one and the enhancement of fuel injection into supersonic streams when penetration height is paramount as with low aspect ratio inward turning designs.

The objective of the combustion characterization study was to continue the work started by Zang[31] and to establish a baseline set of data points for the simple combustor configuration. The characterization was conducted using static pressure measurements, high speed visual imagery as well as C_2* and CH* chemiluminescence. This baseline is necessary to enable further experimental study of non-traditional geometries as applied to novel hypersonic vehicle designs such as the inward turning inlet.

The main finding in the combustion investigation was that the performance suffered due to very poor fuel-air mixing, leading to the next objective, to develop an effective means to inject and mix fuel in a low aspect ratio combustor, where fuel penetration is critical as in the case of inward turning designs. The goal is to provide a solution to the mixing problem delaying and hindering the progress of hypersonic airbreathing designs.

In order to arrive at a new injector design, first the investigation of two prevalent injection schemes was conducted. Normal or transverse injection and a ramped parallel injection scheme were experimentally studied and compared. The goal of the study was to use to use pressure traces and instantaneous and time averaged Schlieren and Mie-scattering images to evaluate both the degree of mixing, as well as the flow losses incurred by each scheme. The mixing performance enhancing aspects of each injection scheme was to be examined and used to create a new injection scheme.

From the baseline injection investigation a new Fin-Guided fuel injection technique was developed. This technique combined penetration ability of normal injection with the mixing enhancement due to the wake of the ramped parallel injection. The studies conducted were to evaluate the mixing enhancements and flow losses incurred with Fin-Guided injection in the same manner the baseline injections were studied. Normal injection and 45° angled injection schemes were to be employed using the new Fin-Guided scheme to see if the angled injection could perform as well as the normal Fin-Guided injection while adding fuel momentum in the creation of vehicle thrust.

2 Background

2.1 Scramjet Combustion Issues

2.1.1 Fuel Choice

In many applications, volume constraints provide a strong motivation for the use of hydrocarbon fuels over hydrogen fuels in scramjet engines since due to their increased density they require smaller tanks for storage and typically reduced overall vehicle weight. Several studies[33,34] involving scramjet propulsion have shown that hydrocarbons could be a suitable substitute for hydrogen. On the other hand, the relatively long ignition delay time of hydrocarbons compared to hydrogen provides a key obstacle in the development of the hydrocarbon-fueled scramjet. In order to utilize hydrocarbons, cracking of the fuel into smaller more reactive hydrocarbons, such as ethylene is often required,[35] however this is not always sufficient. In the Mach 6 scramjet flight regime there is general consensus that storable JP-type hydrocarbon fuels can be used.[36] Hydrocarbon fuel characteristics such as good energy density and relative ease in handling over hydrogen are the reason it was selected for these investigations. It should be noted, however, that higher flight Mach numbers will most likely require the use of gaseous or liquid hydrogen due to its higher heating value as well as the necessity of using it for active cooling.

2.1.2 Staged Injection

At scramjet flight conditions, the static temperature of the air in the combustor flow after being shocked down to one third its original Mach number is generally high enough to auto-ignite fuel with very little added energy and start the chemical reactions in combustion; however the reactions may not be sustained for very long after ignition.[37] Cain and Walton[38] has shown in studies that the flame speeds produced by these reactions are often an order of magnitude slower than the combustor flow velocity. This difference in the flame speeds and the flow velocity means the traditional flame holding techniques will not work in supersonic combustors, and the creation of highly turbulent and subsonic pockets must be established in the flow for flameholding.

Ignition and flameholding difficulties are compounded in subscale ground tests because of relatively low static temperatures and pressures, the small scales of the combustors and the combustion configurations themselves.[39] In fact, air at 300K accelerated to Mach 2.0 the will drop to a temperature of 166K, making any reactions very difficult to achieve and sustain.

In order to account for these issues and provide a solution to allow proper ignition and flameholding the reactivity of the fuel and air must be increased. Methods to create high enthalpy conditions in ground testing can be achieved by preheating the flow air by the means of a vitiated, electric or pebble bed heater, etc. These systems are cumbersome and often require significant hardware to manage the high temperature and pressure loadings, as well as being expensive. However, Weidner and Drummond[39] have shown that the use of staged (multiple) transverse fuel injectors is an effective alternate method to increase the enthalpy and reactivity in ground tests. A pilot flame is used to locally heat the fuel and air in the mixing region to help start the chemical reactions. A diagram of a staged fuel injection system is presented in Figure 2.1:

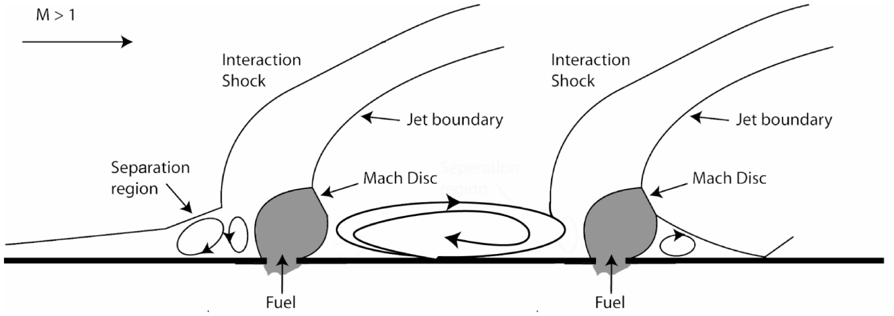

Figure 2.1: Schematic of staged injection flowfield adapted from Weidner.[39]

Generally the pilot flame is situated upstream of the main fuel injection to increase the reactivity of the air which it is about to mix with. The two transverse jets impinging on the cross flow create a very complicated flow structure. This structure allows the staged fuel injection to help create pockets of turbulence and subsonic regions to act as flameholders. Staged fuel injection not only increases the enthalpy of the flow to aid ignition, but the separated regions and recirculation zones in the boundary layer act as flameholders as well; thus addressing two difficulties found with ground testing, ignition and flameholding. Staged fuel injection has been chosen for these reasons to be used in the combustion tests described in this work.

2.2 Mixing

One of the most important aspects of scramjet technical development is the successful demonstration of an efficient combustion system.[32] In order for scramjet combustor to be efficient it will require a fuel injection system which does not cause large flow losses. At the same time, the injector must achieve rapid macroscale mixing of fuel with oxidizer, promote generation of small-scale turbulence for micromixing when sufficient reactants have macromixed and control pressure rise due to heat generation.[32] All of this must be done in milliseconds, as combustor velocities can be in the thousands of meters per second in a scramjet, creating extremely short combustor residence times.[40]

The ignition and micromixing of reactants taking place on a molecular scale and is very fast, compared to the macroscopic mixing of fuel and oxidizer, which takes place on the turbulent dissipation scale.[32] Therefore the combustion time is dominated by the large scale mixing of fuel and air. Heiser and Pratt[41] give a very thorough discussion of basic fuel-air mixing in their widely accepted textbook. One of the most basic ways mixing is occurs is through the mixing of parallel streams. Heiser and Pratt[41] examined and classified this type of mixing into three separate regimes: zero-shear mixing layer, laminar shear/mixing layer, and turbulent shear/mixing layer. The regimes are defined based on the difference between the two streams velocities or Δu. When Δu is zero and the velocity of the two parallel streams is equal it is known as zero-shear mixing layer, as Δu increases from zero the mixing layer progress to laminar and then turbulent. A diagram of the parallel stream flows is presented in Figure 2.1 for reference. The "shear layer" is defined by the shear stress created by the two streams and the "mixing layer" is defined by the change in mole fraction of air or fuel by one percent from their respective values in the freestream.

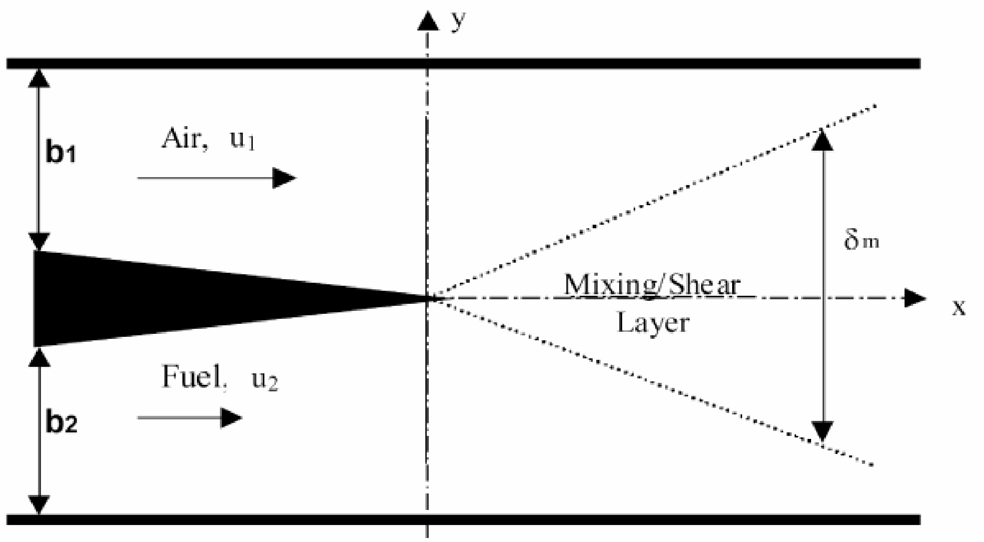

Figure 2.2: Parallel stream mixing/shear layer from Heiser and Pratt.[41]

The first two regimes are not very effective for rapid mixing. Further detail and equations defining these regimes can be found in the aforementioned text. The third regime, turbulent shear/mixing layer, occurs at high values of Δu and becomes an unsteady process as the flow goes from laminar to turbulent, this is the case in which mixing takes place the fastest. The unsteady turbulent flow causes large vortex shedding, sometimes referred to as "roller bearings", which occur at a period rate. Gutmark, et al.[42] points out that the formation of the vortex structures is initiated by Kelvin-Helmholtz instability; governed by Rayleigh's equation for inviscid flows. The exponential growth of the velocity and vorticity perturbations leads to a nonlinear process that eventually causes the roll-up of the shear layer into vortices, which are then shed. This phenomenon is exploited in many mixing schemes.

Turbulent mixing through shear layers has been studied by numerous authors.[43-46] Brown and Roshko were two early pioneers in this field and investigated the density effects and role of large structures in turbulent mixing layers.[43] The authors found through their studies that compressibility is the controlling factor in supersonic turbulent mixing layers, is uncoupled from the density ratio and velocity ratio of the streams. In studies where density ratio and velocity ratio of the two streams was held constant the amount of mixing deviated up to ten times for compressible fluids versus incompressible fluids.

Through their work, Brown and Roshko developed the convective velocity, U_c, parameter; defined as the speed of a point traveling with the large structures formed in the shear layer. Papamoschou[46] and Papamoschou and Roshko[47] investigated the convective velocity parameter and defined a series of convective terms. Consider a stagnation point moving at convective velocity, U_c, on an infinitely thin shear layer structure between the two parallel flows. This definition is explained graphically in Figure 2.3 (a) in the stationary frame of reference and in (b) the convective frame of reference.

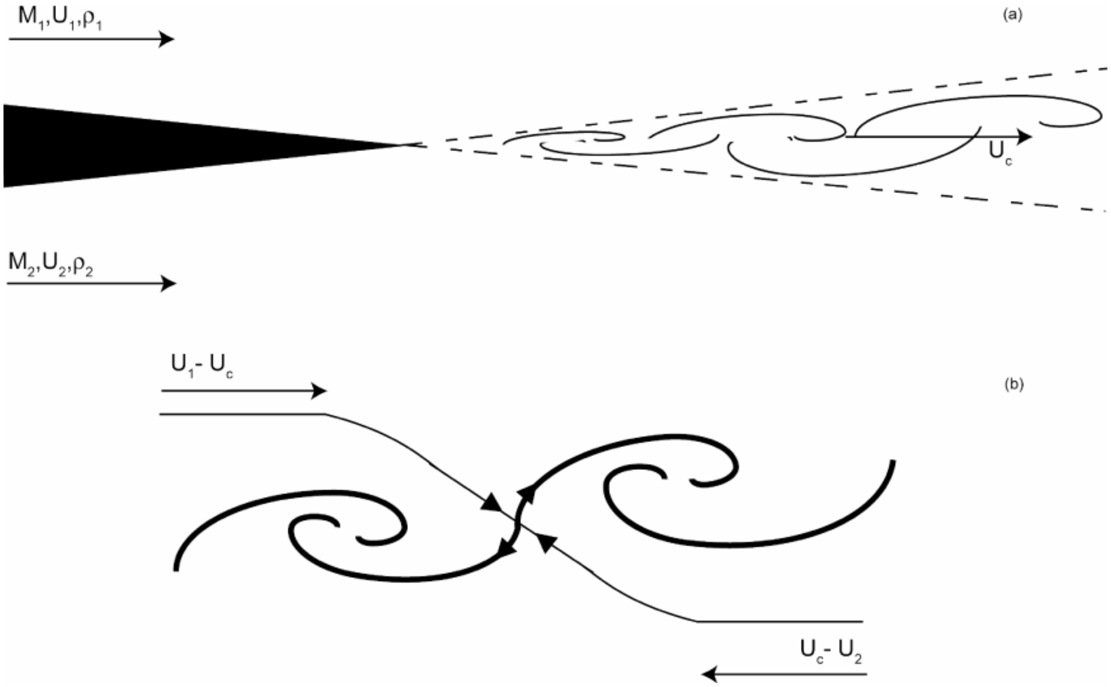

Figure 2.3: Turbulent shear layer in a.) stationary frame of reference b.) convective Frame of reference with streamlines.

The convective Mach number is defined as:

$$M_C = 2\frac{(U_1 - U_2)}{(a_1 + a_2)} \qquad [1]$$

where a_1 and a_2 are the respective speeds of sound in each stream. Seiner, et al.[32] relate the reduced shear layer growth at compressible speed to incompressible shear layer growth as:

$$\frac{C_\delta}{(C_\delta)_o} = \frac{C_\delta a_1 M_c}{const(U_1 - U_2)} \qquad [2]$$

where C_δ is the change in shear layer growth over distance and $(C_\delta)_o$ is the incompressible growth rate. The constant (*const*) is a function of their measurement technique and was found to be 0.14 for Pitot tube measurements and 0.17 for shadowgraph visualization measurements. The compressibility effect and the rapid decrease in mixing efficiency in supersonic flows as Mach number increases have been thoroughly studied and the need to devise ways to enhance mixing in order to have sufficient combustion is clear.[32] The following section reviews some techniques currently studied to enhance mixing.

2.2.1 Mixing Enhancements

The performance of a fuel injection system is defined by its effectiveness and efficiency, and is the driving factor in combustor efficiency. Efficiency is reflected in the degree of fuel-air mixing achieved, while effectiveness is associated with the minimization of the combustor exit stream thrust losses incurred in the mixing process and the extent of the additional wall cooling or thermal protection risk associated with the fuel injector concept.[48] Generally speaking, efficiency will always come at a cost of effectiveness as a trade off. Different injection schemes are used depending on which aspect of the fuel injection is most important.

Kutschenreuter[48] classifies fuel injector concepts into two general types: 1) wall jets and 2) instream injectors. A wall jet injector does not protrude into the combustor crossflow, instead the fuel jet is injected flush to the wall. An instream injector employs the use of some device which extends into the combustor crossflow to inject fuel. Most commonly a wall jet injection scheme will have greater effectiveness since no protruding structure, causing shock losses and possible requiring cooling, is used. However, these structures found in instream injector schemes are generally more efficient. Both schemes are examined further.

2.2.1.1 Efficiency

Mixing efficiency is a measure of the amount of fuel-air mixing achieved. Efficiency can be quantified in numerous ways, some techniques quantify nearfield mixing, others farfield mixing, while others take into account both. One of the most rigorous definitions of mixing efficiency is defined as the measure of fuel which would react if no further mixing occurred, divided by the amount of fuel that would react if uniform mixing had been achieved.[41] In the current study the efficiency of nearfield or large scale stirring is quantified by measuring two injection characteristics; the fuel penetration and the fuel-area.

The fuel penetration efficiency, η_h, is defined as the fuel penetration height divided by the total duct height, as shown in equation [3]. This efficiency varies at different axial locations of the combustor. The fuel penetration height is measured as the mixing boundary between the fuel and core air flow.

$$\eta_h = \frac{Fuel\ Penetration\ Height}{Duct\ Height} \qquad [3]$$

The fuel-area efficiency, η_A, is defined as the area within the combustor in which fuel has spread divided by the total combustor cross sectional area at a give axial location, shown in equation [4].

$$\eta_A = \frac{Area\ Occupied\ by\ Fuel}{Total\ Cross\text{-}\sec tional\ Duct\ Area} \qquad [4]$$

The two parameters above are used to define the mixing efficiencies in the subsequent studies. They are measures of the large scale stirring achieved by each fuel injection method.

2.2.1.2 Effectiveness

The effectiveness of a fuel injection method is a measure of the penalties associated with the fuel injection technique. The complexity added to the combustor due to fuel injection, increased number of heating surfaces, the need to provide thermal protection, total pressure losses, increase in weight are all items which can be evaluated in the effectiveness of a mixing scheme. The current study uses pressure traces to evaluate the effectiveness of a given method. Because only static pressure measurements can be taken, total pressure loss can not be directly evaluated without some analysis. The static pressure rise can occur due to shock or viscous losses, as well as through isentropic compression.

The pressure rises due to changes in geometry and shocks has been thoroughly studied. Anderson[49] provides a detailed summary of the compressible effects in supersonic flows. Equation [5] shows the Area-Mach number relationship. For isentropic flows the Mach number will vary based on the geometry alone. Once the flow Mach number is found using the Area-Mach number relation, the static pressure over stagnation pressure is easily calculated using isentropic equation [6].

$$\frac{A}{A_t} = \frac{1}{M}\left[\frac{2}{\gamma+1}\left(1+\frac{\gamma-1}{2}M^2\right)\right]^{\frac{\gamma+1}{2(\gamma-1)}} \qquad [5]$$

$$\frac{P}{P_0} = \left(1+\frac{\gamma-1}{2}M^2\right)^{\frac{-\gamma}{\gamma-1}} \qquad [6]$$

The procedure described above allows for one to predict the static pressure rises and drops due to isentropic area changes. These changes in static pressure do not result in a loss of stagnation or total pressure. Total pressure losses occur when there are shocks in the flow. The pressure loss across shock waves has also been well studied. Equations [7]-[11] are normal shock equations, and are used to evaluate the change in static pressure (*P*), temperature (*T*), entropy (*s*) and total pressure (P_0) across a normal shock. The subscript 1 denotes flow properties upstream of the shock, while the subscript 2 corresponds to conditions downstream of the shock.

$$\frac{P_2}{P_1} = 1 + \frac{2\gamma}{\gamma+1}\left(M_1^2 - 1\right) \qquad [7]$$

$$\frac{T_2}{T_1} = \left[1 + \frac{2\gamma}{\gamma+1}\left(M_1^2 - 1\right)\right]\frac{2+(\gamma-1)M_1^2}{(\gamma+1)M_1^2} \qquad [8]$$

$$s_2 - s_1 = c_p \ln\frac{T_2}{T_1} - R\ln\frac{P_2}{P_1} \qquad [9]$$

$$\frac{P_{0,2}}{P_{0,1}} = e^{-(s_2 - s_1)/R} \qquad [10]$$

$$M_2^2 = \frac{1+[(\gamma-1)/2]M_1^2}{\gamma M_1^2 - (\gamma-1)/2} \qquad [11]$$

In order to evaluate the flow changes across an oblique shock wave of angle β one must find the flow Mach number normal to the shock wave, M_n. Because the changes across an oblique shock wave are governed only by the component of velocity normal to the wave, M_n can be substituted into the normal shock equations to find the strength of the oblique shock.[49] The normal Mach number is found using equation [12], where M_1 is the full Mach number of the flow.

$$M_{n,1} = M_1 \sin\beta \qquad [12]$$

To evaluate the pressure further downstream of the shock, the method used to predict the static pressure over the total pressure can be reused, however, a new throat area, A_t, must be calculated first. Using the equations provided, when can perform a simple quasi one dimensional analysis of the flow losses incurred through an injection scheme by estimating what the resulting shock structures will be. One can also determine which pressure changes result in total pressure loss by comparing pressure traces to isentropic models.

2.2.1.3 Wall Jets

The most common and widely studied form of wall jet injection is transverse injection, or injection normal to the wall surface. Orth, et al.[50] was one of the first to examine the interaction and penetration of transverse injection into supersonic flows. However, many further studies[51-53] have been conducted. The complex interaction between in the gaseous jet and supersonic flow is shown in Figure 2.4 taken from Rogers.[53]

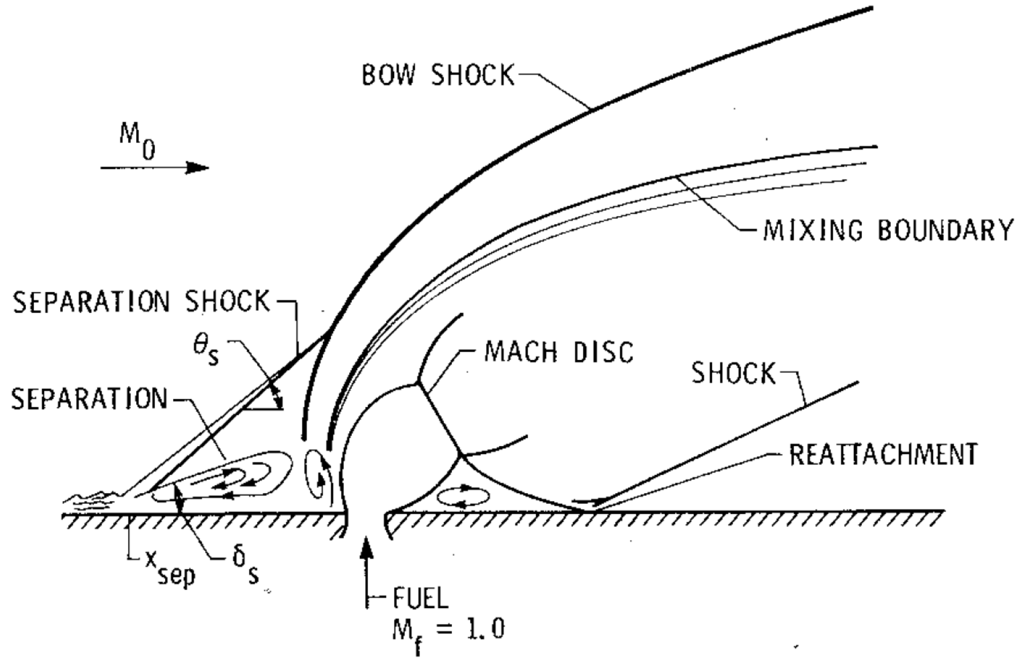

Figure 2.4: Aerodynamics of transverse injection into supersonic flow (from Rogers[53]).

The figure shows the structures formed when fuel is injected sonically into a supersonic crossflow. The fuel jet can be modeled as circular rod in the supersonic flow. The fuel jet causes recirculation zones and boundary layer seperation upstream and downstream of the injection location. A separated shock forms upstream of the boundary layer separation zone and coalesces with the bow shock which is formed by the fuel jet. The most common parameter to quantify the fuel injection is the height of the penetration, generally associated with the mach disk shock. A shock forms after of the boundary layer separation downstream of the fuel injection. The greater the momentum flux of the fuel being injected, the larger and further reaching the separated zones in the boundary layer will becomes. The strength of the bow shock will also vary with the fuel jet momentum.

Many, including Gruber, et al.[54] have defined the key parameter governing the flow field jet in a cross flow is the square of the momentum flux ratio, which is defined as:

$$J = \sqrt{\frac{\rho_f V_f^2}{\rho_\infty V_\infty^2}} \qquad [13]$$

where the subscripts *f*, and ∞ refer to the fuel stream and the free stream respectively. Gruber, et al.[54] suggests the following power law, obtained from planar Mie-scattering, for determining the penetration of a sonic jet into a Mach 2 cross flow:

$$\frac{y}{dJ} = 1.23\left(\frac{x}{dJ}\right)^{0.344} \qquad [14]$$

where *y* is the penetration distance, *d* is the circular orifice diameter, and *x* is the axial distance downstream. Many studies have shown that this penetration depth is a key parameter in the amount of mixing that takes place in transverse injection model.

There have also been numerous studies on angled wall injection.[55-59] Angled injection schemes are used to limit the amount of flow losses incurred with transverse injection and also to add axial momentum to create thrust.

2.2.1.4 Instream Injectors

Instream injection is the second major scheme used to mix fuel in combustors. There are many variations of instream injection. Most involve some type of ramp introduced into the supersonic flow from which the fuel is injected. The physics behind the instream injectors follows the shear layer mixing laid out earlier. A detailed summary of many instream injection schemes can be found in Rogers, et al.[60] These schemes include swept and unswept ramps, cantilever ramps, as well as compression and expansion ramped injectors. Northam, et al.[62] investigated swept and unswept wall mounted ramps, they found that the swept ramps provided greater vortex shedding aiding the fuel mixing then the unswept cases. Schumacher and Sislian[64] found that angled injection was better than parallel injection and that wall mounted ramps more effective and efficient than cantilevered ramps. In all of the instream injection schemes where the fuel is injected parallel or at an angle less than 90° the fuel momentum flux was added directly to the vehicle thrust.

2.2.1.5 Pylon-Aided Injection

The use of pylons has recently been shown to enhance mixing in supersonic streams.[65-68] The pylons, which are generally small blade-like triangular wedges, are placed upstream of wall jet injectors so that its wake can enhance mixing. Pylon-aided injection schemes fall in between wall jet and instream schemes, as the fuel injected through the wall, however a pylon is introduced instream to aid injection. Primary use of pylons has been to aid pre-injection of fuel in the inlets of scramjets, to provide uniform fuel-air mixtures in the combustor. Livingston and Segal[66] used pylons to aid in the penetration and spreading of liquid jets in the inlet of scramjet. The pylons were used to create low-pressure regions at the liquid injection station to increase penetration, thus avoiding the presence of low-speed combustible mixture in the inlet/isolator boundary layers providing a mechanism to eliminate potential flashback. Montes, et al.[65] and Owens, et al.[67] conducted similar tests with gaseous fuel. Pylons were used to aid the pre-injection of fuel upstream of the main combustion zones and to lift fuel out of low speed boundary layers to avoid flashback and flame holding in undesired locations. The pylons also had an added benefit of reducing the pressure losses associated with transverse injection,[65-67] providing that the aerodynamic drag and shock losses are minimized by keeping the pylons relatively small compared to the overall duct sizes. It was concluded that combined with injection, the shock-jet interactions created by the pylons caused vorticity via baroclinic torque and cross-stream shear and may improve mixing.

Gouskov, et al.[68] conducted numerical studies to determine optimal dimension for pylons. The study showed that the pylon height should be no more than 4 times the injector diameter and 1.12 times as wide. The angle of inclination for the pylons was found to be best at 30°. This inclination angle is later used in the Fin-Guided injection schemes described in later chapters of this thesis.

3 Scramjet Combustion Characterization

An experimental study of a three-dimensional Mach 2 scramjet combustor with aspect ratio one has been conducted. The combustor featured a square cross-section and a three-dimensional expanding section and was designed to mimic low aspect ratio nature of inward turning vehicle designs. The combustor achieved its maximum performance when the equivalence ratio was only 0.25, this was found to be due to poor mixing. This study aims to provide performance data for a three-dimensional supersonic combustor using wall normal injection to be used in comparisons in future studies utilizing different combustor geometries and injection schemes.

3.1 Apparatus and Experimental Setup

The following experiments were carried out on the reacting test stand in the Advanced Propulsion Research Laboratory (APRL) located at the University of Maryland, the work was done jointly with Gregory Young. Combustion characterization tests were conducted in a supersonic duct designed by Zang.[31] A rough schematic of the setup is shown Figure 3.1. Supply air is brought through a converging-diverging nozzle which accelerates the flow to Mach 2. A short, constant area isolator separates the nozzle from the combustor test section, where all four walls of the duct are expanded at a constant angle. Two injection ports are located immediately downstream of the duct expansion point from which fuel and a pilot flame are introduced to the duct air flow. A quartz window makes up one of the test section walls to allow optical access. The combustor exhaust passes through a water cooling system and is vented into the atmosphere. A greater description of the rig is found in the subsequent sections, and can also be found in Zang.[31]

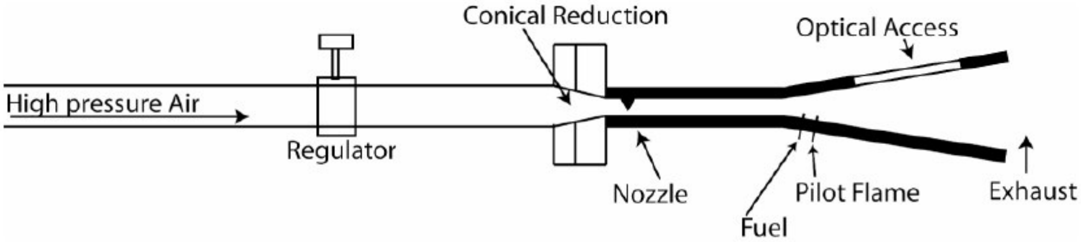

Figure 3.1: Basic schematic of supersonic combustion rig.

3.1.1 Hardware and Design

An Atlas Copco Compressor was used to deliver the necessary airflow in the combustion experiments. The compressor line is fed through a settling tank and dryer before being passed through a gas/air filter mated to the 2 inch (5 cm) laboratory supply lines. The settling tank removes any oil or debris caught in the airflow, and the dryer removes moisture in the air by lowering the air temperature below freezing. A ball valve is placed on the supply line when it has reached the laboratory. A Wilkerson screw type regulator valve with an operating range of 0-180 psi follows the ball valve and is used to control the mass flow and stagnation pressure upstream of the test section. The pressure is measured directly downstream of the regulator with a Setra Model 206 static pressure transducer with a range of 0-250 psi and monitored on a calibrated Datum 2000 dual channel display. The compressor is able to supply a maximum mass flow of 358 cubic feet per minute at 150 psi to the laboratory.

A 2 meter long 5 cm steel pipe brings the supply air to the supersonic duct from the regulator. The pipe is then mated to a custom milled, aluminum transition block via a 12.065 cm (4.75 in) bolt circle. The transition block uses a 5.08 cm (2 in) long conical reduction to bring the airflow cross-section from a 5.08 cm circle to a 1.27 cm (0.5 in) square cross section. Connected to the transition block is another milled aluminum block referred to as the front block. The front block mates the transition block to the combustor test section. The block also houses a 0.7 inch by 0.7 inch flow straightener which has hexagonal cells approximately 0.005 square inches in area. The flow straightener extends the full thickness of the front block, 2 inches. The supply pipe, transition block and front block are all sealed via o-ring connections. The transition and front blocks are also used in the fuel injection experiments explained in Chapter 4. Schematics of the front block and the transition block can be found in the Appendix.

The supersonic duct used for the combustion characterization is made from three components, a solid combustion block, a nozzle plate, and a quartz window held in place by a window holder. All three parts are milled from 306-stainless steel to withstand the heating loads incurred during testing. The combustion block makes up three walls of the duct, the nozzle plate and window holder combine to make up the forth wall. The supersonic duct begins with a 1 inch long, 0.5 inch by 0.5 inch constant area section and is followed by a 1 inch long converging-diverging nozzle with throat area of 0.148 square inches. The nozzle accelerates the flow to Mach 2. Downstream of the nozzle is a 4 inch long, 0.5 inch by 0.5 inch constant area section.

At the end of this constant area section all four walls of the combustor expand at an angle of 3.6°. Throughout the full length of the combustor the aspect ratio is fixed at one.

Along with the quartz window which allows optical access for diagnostics, the combustion block contains 52 static pressure ports on its top and side walls, with 26 on each wall. The pressure ports are perpendicular to the combustor surface and have a diameter of 0.04 inches. There are 4 pressure ports located on each of the top and side walls of the duct, beginning 2.0 inches upstream of the expansion point spaced 0.5 inches apart. A second series of 22 pressure ports begins 0.25 inches downstream of the expansion point, also spaced 0.5 inches apart. The second and fourth pressure ports in the expansion zone are used to introduce the pilot flame and fuel injection into the combustor from either the top or side wall. These ports have been drilled to 3/16 inches in diameter and also have a 1/8 normal pipe thread (NPT) tap on the outer surface used for interfacing. A schematic of the supersonic duct is shown in Figure 3.2, and CAD drawings of the combustion block, nozzle plate and window holder can be found in the Appendix.

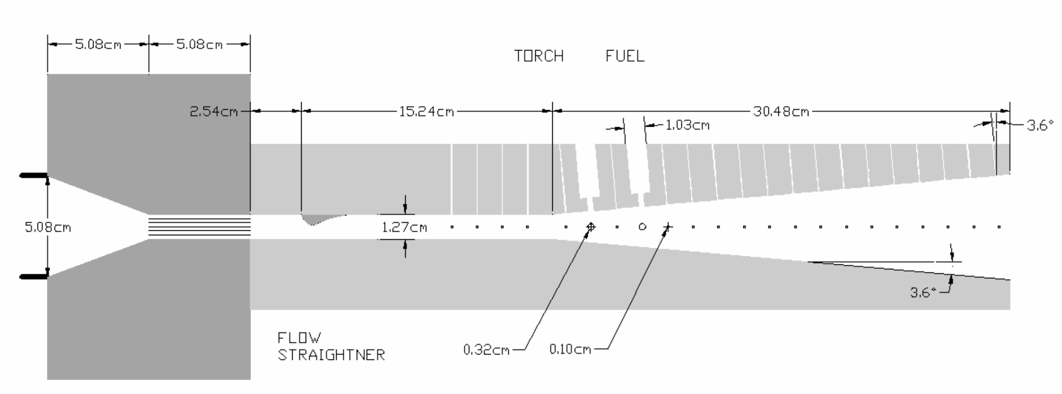

Figure 3.2: Basic drawing of supersonic combustor.

The pilot injector was a 4.8-mm-diameter sonic orifice supplying pre-combustion products of a fuel-rich ethylene-oxygen reaction. The pilot torch, also called a gas generator, was mated to the combustor via a 1/8 inch NPT nipple. The torch acted as an ignition source and was operated fuel rich to introduce hot pre-combustion products to the duct. A sparkplug was located at one end of the torch. There were four 1/8 inch NPT taps drilled into the torch, which were used for fuel injection. Two injection ports were located 1 inch from the sparkplug, the other 2 were located another 0.5 inch down. The top two injection ports were used for oxygen and ethylene, while the other two were used for a nitrogen purge and for pressure measurements. The torch cavity is 0.540 inches in diameter for 2 inches, before being stepped down to 0.405 inch for the last inch. A schematic of the torch is shown in Figure 3.3.

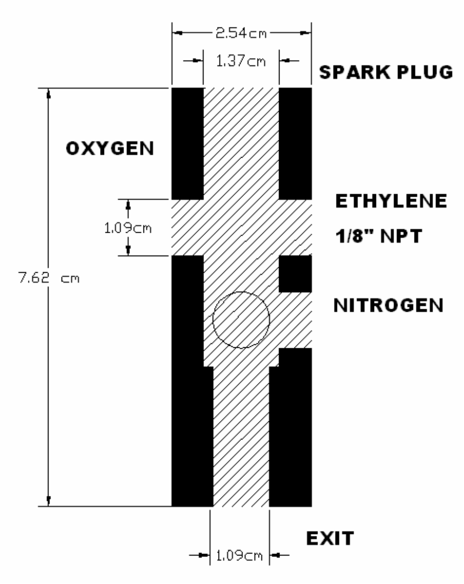

Figure 3.3: Basic diagram of gas generator.

3.1.2 Diagnostics

3.1.2.1 Pressure Measurements

A Scanivalve Corporation DSA-3217 Digital Sensor Array was used to make static pressure measurements at all of the pressure ports along the top wall of the combustor. This array consists of 16 temperature compensated piezoresistive pressure sensors with a pneumatic calibration valve. The 16 sensors, or channels, all have a range of 0-1.5 MPa. Their associated error is ±0.2% of scale for pressures less than 0.1 MPa, ±0.12% of scale for pressures between 0.1 and 0.14 MPa, and ±0.05% of scale for pressures above 0.14 MPa. This error is smaller than the standard deviation of the data collected. The measured pressures are sent via a TCP/IP connection to a desktop computer and into a LabView virtual control panel. This virtual interface (VI) allowed for monitoring of all 16 channels and the DSA's settings, while also writing the data and saving it for later processing. The default settings for the DSA were manually changed to give better temporal resolution and to provide data for determination of error. Settings which were changed were the period, or time between scans, which was set to the minimum setting of 250 μs and the average which was set to 5 scans. There are over 50 pressure taps on supersonic duct, because only 16 can be monitored at once, the others were capped.

3.1.2.2 Chemiluminescence

To further characterize the flame front and combustion characterization CH* and C_2* chemiluminescence images were collected. Chemiluminescence appears when a chemical reaction in a chain of reactions mainly produces some molecules in an electronically excited level.[69] These molecules undergo transitions from higher to lower energy states that result in fluorescent emissions at specific frequencies depending on the molecule that has been excited. The emissions can be isolated and visualized by using narrow-band pass optical filters, for CH* chemiluminescence a 430±3 nm centered filter is used and a 516±3 nm centered filter is used to capture C_2* radicals. Chemiluminescence can be used to quantitatively find the heating value of a flame, as wells to qualitatively measure the flame structure, since the intensity of the chemiluminescence is directly related to the amount of radicals produced in the combustion process. The chemiluminescence images presented in this work were taken using a Cooke Corporation Dicam Pro Intensified CCD (ICCD) camera in conjunction with the appropriate filters. The ICCD has a shutter speed as short as 3 ns and can operate at a framing rate up to 12 Hz. The images make it possible to estimate the instantaneous and time-averaged flame areas and thus quantify the area affected by the injected fuel and are used to verify the data found in the images collected with the high speed camera.

3.1.2.3 High Speed Images

Flame front dynamics were qualitatively characterized using a FASTCAM-Ultima1024 model 16K high speed camera. In typical experiments, a framing rate of 250 Hz and a shutter speed of 1/500 sec were employed to capture instantaneous images of the flame. Images were taken with the pilot flame and injection on the top and back walls, to give two separate views of the flame. When the pilot and fuel injection was done through the side wall a neutral density filter with an optical density of 1.0 was placed in front of the pilot injection site so the image obtained would not become over saturated. For calibration and measurement purposes one image of the test section was taken prior to testing with a grid containing cells of 0.25 inch by 0.25 inch (0.635 x 0.635 cm) attached to the quartz window. This image was then superimposed on all of the images taken of the reacting flow field for analysis.

3.1.3 Experimental Procedure

The test procedure started with supplying air to the supersonic duct, followed by flowing oxygen and ethylene to the gas generator. The oxygen and fuel was then ignited in the gas generator using an automotive sparkplug. Once the pilot injection had been established in this manner the main fuel would be injected into the duct. To end the test, the main fuel and pilot injection were stopped simultaneously as a nitrogen purge was initiated. A typical test lasted between 2 and 3 seconds, with the pilot injection starting a quarter of a second prior to the main fuel injection; the nitrogen purge lasted 4 seconds after the test was concluded. The main air would be allowed to run for several minutes after the combustion test to aid in cooling.

The air flow was established using the Wilkerson regulator and the Setra static pressure transducer described earlier. Gaseous oxygen (O_2), ethylene (C_2H_4), and a nitrogen (N_2) purge were supplied to the gas generator via steel piping from reservoir tank. The main fuel ethylene was supplied to the duct in a similar fashion. Choked orifices in each gas supply line regulated the inlet mass flows. The oxygen and fuel stagnation pressures were measured and recorded to ensure the validity of each test.

Solenoid valves were used to open and close the fuel and nitrogen purge lines to the rig and were controlled by a custom built LabView virtual interface (VI) and electronic switchbox. The sequence in which the fuels were injected into the torch/combustor, as well as the duration for which they flowed were all controlled to fractions of a second using the LabView interface. The LabView interface also recorded all of the pressure data collected by the DSA described earlier and the pressure transducers on the gas supply lines. The spark plug used to ignite the oxygen and fuel in the gas generator was also controlled by the LabView VI.

Table 3-1 provides mole fractions of the pilot injection species for two cases, calculated using the NASA CEA 2000 computer code. Any species not accounted for, occurred in molar concentrations of less than 1%. The main fuel injector was also a sonic orifice of the same size as the pilot injector, and supplied cold ethylene (C_2H_4) to the combustor at 25.4-mm downstream from the pilot injector.

Table 3-1: Summary of test flow conditions.

Core Air			Pilot Injection (C, CO, H_2)				Main Fuel (C_2H_4)	
P_o(MPa)	$\dot{m}$ (kg/s)	T_o (K)	P_o (MPa)	T_{ad} (K)	T* (K)	$\dot{m}$ (kg/s)	T_o (K)	$\dot{m}$ (kg/s)
0.86	0.193	298	0.23	2310	2039	$4.08\text{x}10^{-3}$	298	$0 - 3.97\text{x}10^{-3}$
0.93	0.208	298	0.34	2313	2040	$4.46\text{x}10^{-3}$	298	$0 - 4.27\text{x}10^{-3}$

Table 3-1 summarizes the flow conditions used in this study. In each test, the equivalence ratio of the pre-combustion reaction in the gas generator, leading to the pilot injector, was held constant at 3.1. The excess fuel from the pilot injection alone accounted for an equivalence ratio of 0.1 in the main combustor. Details of two different flow conditions with the core flow stagnation pressure of 0.86 MPa and 0.93 Mpa are shown in Table 3-2. They represent the two highest air flow rates reached during the experiments. The stagnation conditions for the air and the main fuel flows were measured while calculated adiabatic conditions are listed for the pilot injection condition. The total mass flow rates were based on experimental measurements through flow metering orifices for all flows including the pilot injection. Pressure measurements were taken under reacting conditions of only the pilot on, and both the fuel and the pilot on. Also, non-burning cases with the air flow only as well as both the pilot and main fuel on but without ignition were characterized. Main fuel pressures were varied to produce a range of equivalence ratios in the combustor section.

Table 3-2: Pilot injection species mole fraction.

Core P_o (MPa)	C	CO	H_2
0.86	.0068	.4898	.4964
0.93	.0066	.4901	.4968

3.2 Results

3.2.1 Wall Pressure Traces

The Scanivalve Digital Sensor Array described earlier was used in all of the tests to measure the combustor wall pressure. Figure 3.4 is one such plot of the pressure traces collected. The *x*=0 cm corresponds to the location of the pilot injection. Examining the core air case shows that the wall pressure is initially dropping in the expansion zone of the combustor, however close to 40 mm downstream of the pilot injector location boundary layer separation effects occur and the pressure begins to rise. The "cold flow" condition is defined as fuel and oxidizer flowing in the pilot combustor as well as primary fuel flowing in the main combustor un-lit, whereas core air is simply the wind tunnel air flow with no addition of fuel. Figure 3.4 clearly shows the addition of mass in cold flow effect the location at which the flow changes from supersonic to subsonic, which is now pushed to near 50 mm downstream of the pilot injection. While the addition of fuel in reacting flow maintains the extended region of supersonic flow, but does so at a higher pressure. This higher pressure is due to the combustion process taking place in the region. One would expect that has a greater amount of combustion takes place the greater the pressure rise notice will be.

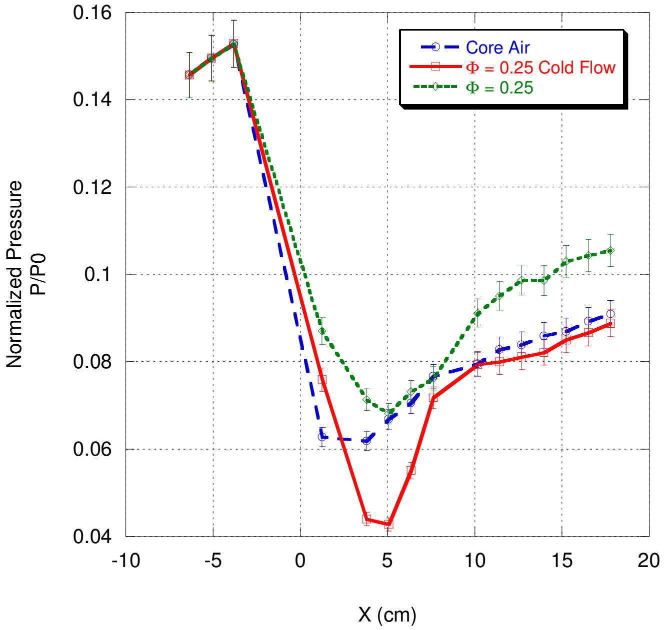

Figure 3.4: Sample normalized wall pressure distribution (P_0=0.93 MPa).

The “peak” pressure rise associated with the lit fuel tests was used to evaluate the combustor performance at varying equivalence ratios. The equivalence ratio was increased from Φ=0.10, provided by the pilot injection, to Φ=0.40 by supplying cold ethylene into the combustor through the main fuel injector to observe the effect of fuel addition. Figure 3.5 provides a summary of the tests conducted at an upstream stagnation pressure of 0.93 MPa. While both the visual images and the wall pressure measurements clearly indicated that the reacting flow remained supersonic near the injectors, it appeared that the combustor flow might be transitioning to subsonic flow beyond x=50 mm. Downstream of this point, the measured wall pressure indicated adverse pressure gradient, even though the area was still expanding. Flame images indicated that this may be due to shock rather than thermal choking. However, the measured pressure increases in this region were substantially smaller than a pressure rise induced by a normal shock. Thus, it appears that the flow field was highly three-dimensional and there could have been partial thermal choking as well as boundary layer separation. Figure 3.6 shows similar results for tests conducted at an upstream stagnation pressure of 0.86 MPa.

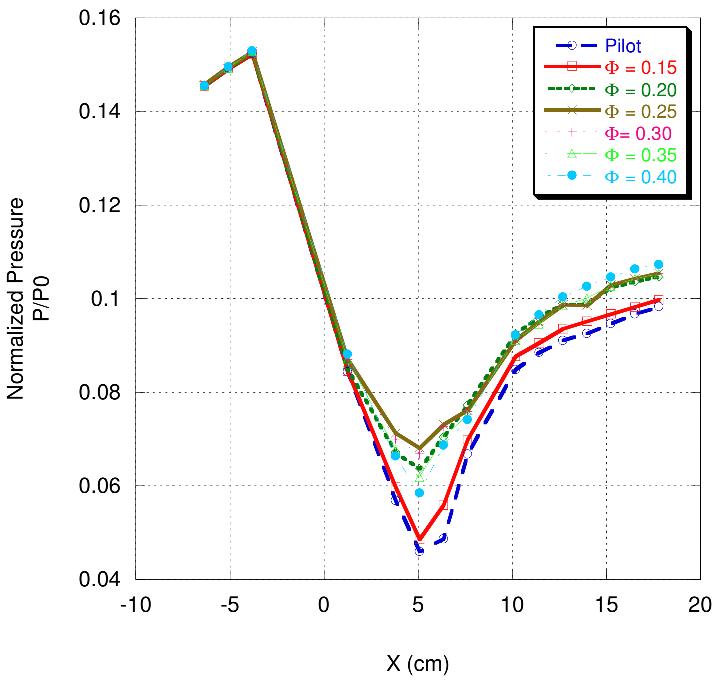

Figure 3.5: Normalized wall pressure distribution for all conditions (P_0 =0.93 MPa).

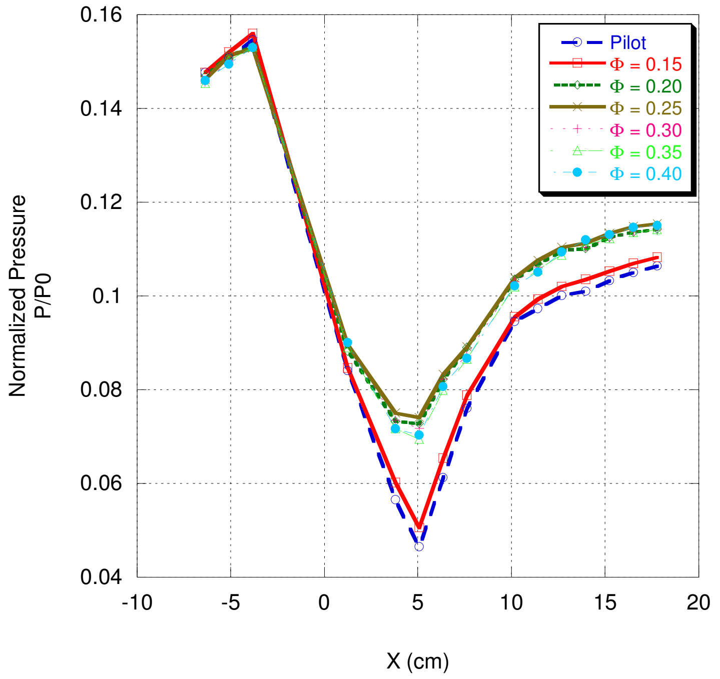

Figure 3.6: Normalized wall pressure distribution for all conditions (P_0 = 0.86 MPa).

The peak pressure rise associated with the combustion varies with each equivalence ratio tested. A zoomed-in view of the pressure rise due to the combustion is shown in Figure 3.7 for the 0.93 MPa upstream stagnation pressure condition. The peak pressure is lowest when only the pilot flame is ignited; the pressure slowly rises from this point as the equivalence ratio is increased. The peak pressure continues to increase until an equivalence ratio of Φ=0.25 is reached and the highest pressure is obtained. When the equivalence ratio is increased beyond this point the pressure begins to incrementally decrease. This would seem to show that the combustor performs the best at an equivalence ratio of Φ=0.25, rather than the expected Φ=1.0. Figure 3.8 displays the extreme equivalence ratios to further emphasize the trend.

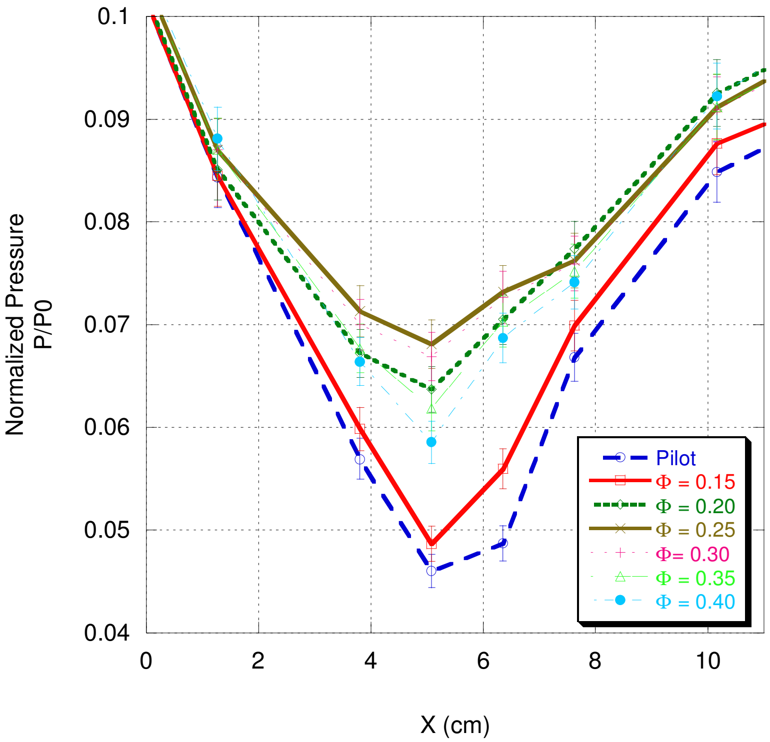

Figure 3.7: Zoomed-in normalized wall pressure distribution for all conditions (P_0 = 0.93 MPa).

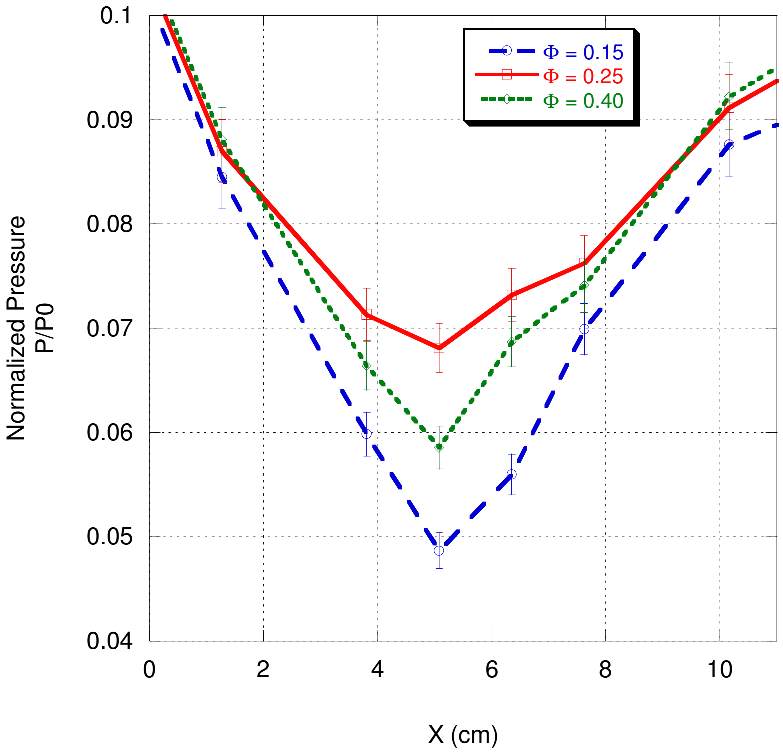

Figure 3.8: Zoomed-in normalized wall pressure distributions for extreme conditions (P_0 = 0.93 MPa).

The decrease in the peak pressure past equivalence ratios of Φ=0.25 suggests that the additional fuel injected is not burning. The extra fuel dilutes the hot combustion products and cools the flame down, resulting in the lower peak pressures. This trend is also noticed at other upstream stagnation pressures. Figure 3.9 and Figure 3.10 illustrate the initial increase in peak pressure until Φ=0.25 and the decrease thereafter for an upstream stagnation condition of 0.86 Mpa. The notion that the greatest amount heat release occurs at Φ=0.25 is further examined using C_2* and CH* chemiluminescence. The data from these tests are presented in the following section.

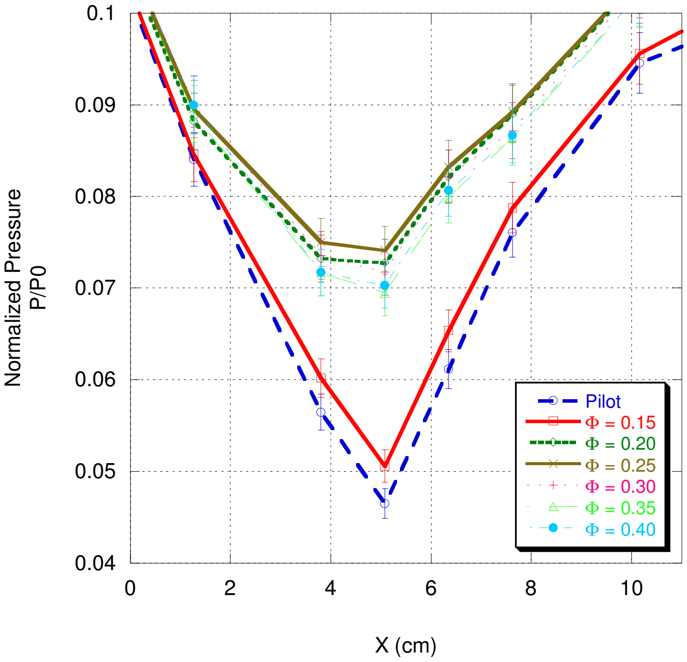

Figure 3.9: Zoomed-in normalized wall pressure distribution for all conditions (P_0 = 0.86 MPa).

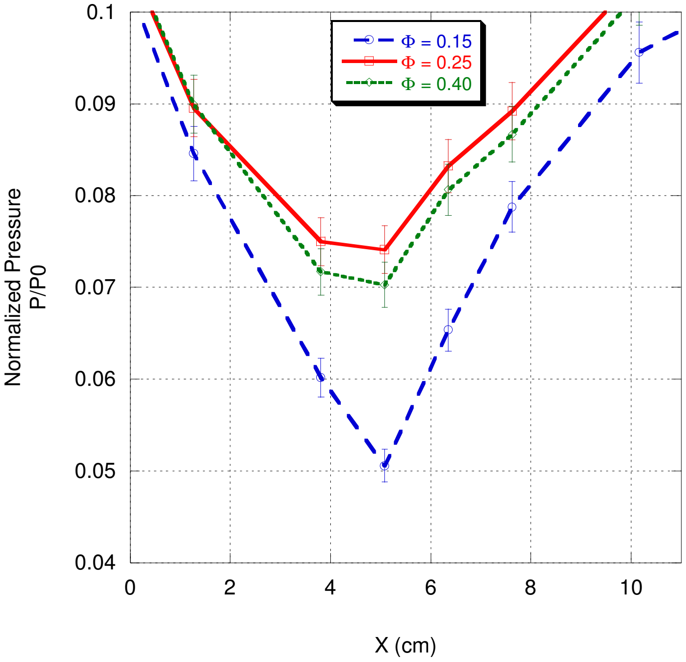

Figure 3.10: Zoomed-in normalized wall pressure distribution for extreme conditions (P_0 = 0.86 MPa).

3.2.2 Chemiluminescence

Images of the chemiluminescence given off by the combustion flame were collected for several of the equivalence ratios presented in the pressure traces. CH* and C_2* chemiluminescence were both measured to qualitatively observe the amount of heat release emitted by each flame, by correlating it to the image intensity. A large set of instantaneous images were collected using the appropriate filters. Figure 3.11 shows instantaneous images of the C_2* chemiluminescence given off during a test at Φ=0.25 with an upstream stagnation pressure of 0.93 MPa. Figure 3.12 shows the CH* chemiluminescence emitted for the same test condition. The images clearly show the flame is turbulent and highly unsteady.

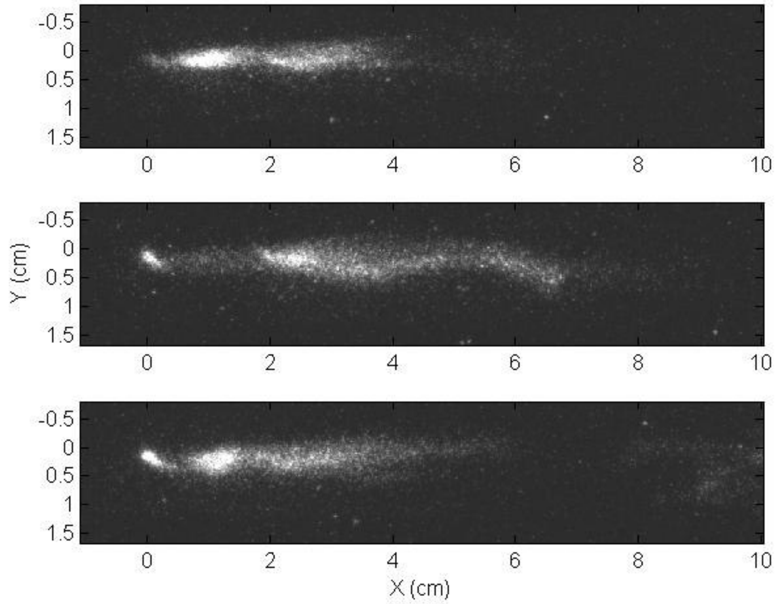

Figure 3.11: Instantaneous C_2* chemiluminescence images (P_0 = 0.93 Mpa, Φ=0.25).

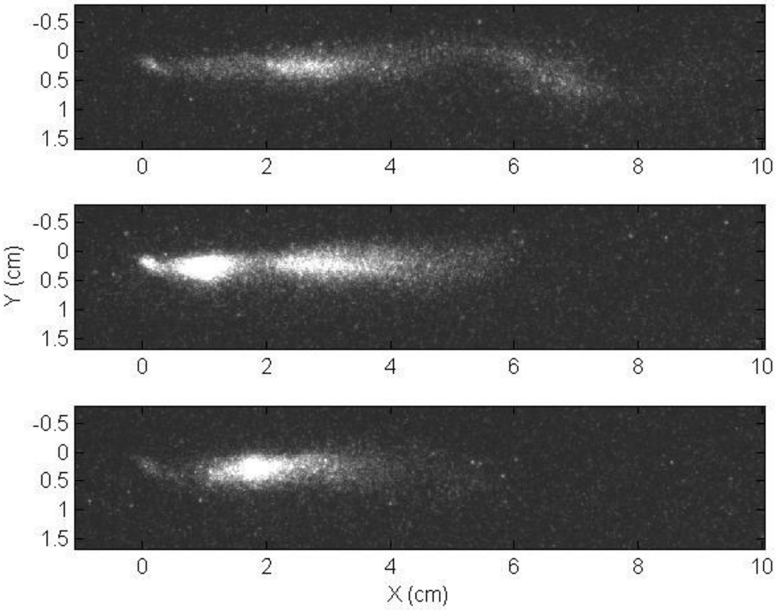

Figure 3.12: Instantaneous CH* chemiluminescence images (P_0 = 0.93 Mpa, Φ=0.25).

In order to evaluate the chemiluminescence intensity and heat release of each flame all instantaneous images for each test condition were averaged together to form one time-average image. Contour plots of the intensity in the time-averaged images were plotted using Matlab to examine the relative flame sizes and intensities for each equivalence ratio. The C_2* and CH* chemiluminescence images for the upstream stagnation pressure of 0.93 Mpa with equivalence ratios ranging between Φ=0.10 to Φ=0.30 are presented in Figure 3.13 and Figure 3.14 respectively.

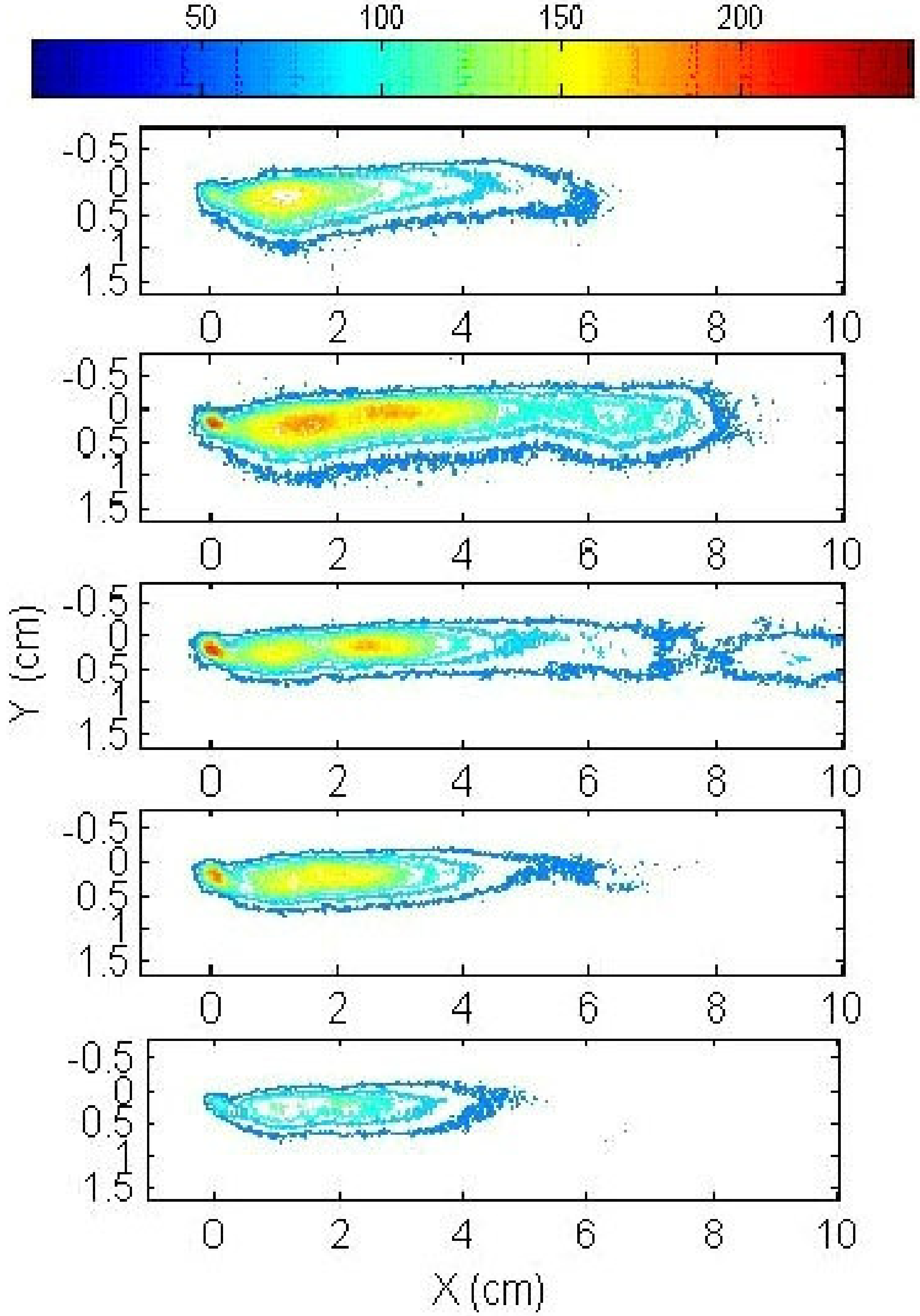

Figure 3.13: C_2* chemiluminescence intensity for Φ = 0.10, 0.15, 0.20, 0.25, 0.30 (top to bottom) and stagnation pressure of 0.93 MPa.

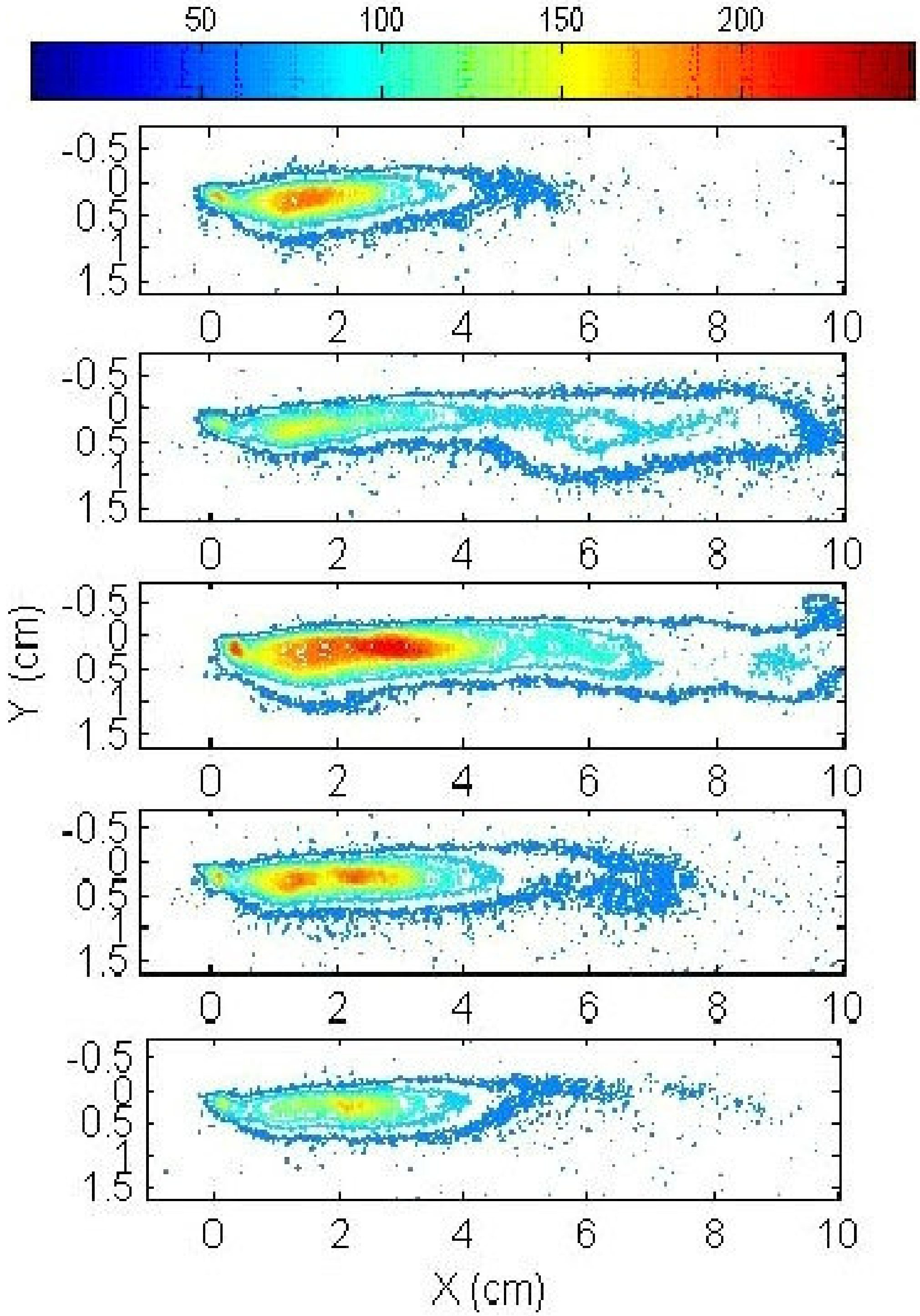

Figure 3.14: CH* chemiluminescence intensity for Φ = 0.10, 0.15, 0.20, 0.25, 0.30 (top to bottom) and stagnation pressure of 0.93 MPa.

It is clear from these figures that the lower equivalence ratios (0.15 and 0.2) experienced more C_2* and CH* chemiluminescence in the subsonic portion of the combustor compared to the higher equivalence ratio cases. It is also clear from the figures that the two extreme cases (Φ = 0.10 and 0.3) have considerably less intensity compared to the Φ = 0.2 and 0.25 cases for both radicals. The C_2* intensity is similar for the two cases, but the CH* intensity is clearly greatest for Φ = 0.2 in the supersonic region. The pressure traces also showed these two conditions to be quite similar as well. This chemiluminescence data is consistent with the observations from earlier, in that the optimum equivalence ratio for this combustor is somewhere between 0.2 and 0.25. Chemiluminescence images were also collected for the upstream stagnation pressure of 0.86 MPa and similar results were found shown in Figure 3.15 and Figure 3.16. There are few high intensity spots in the pilot torch images, however the largest flames are still found when the equivalence ratio is Φ = 0.2 or Φ = 0.25.

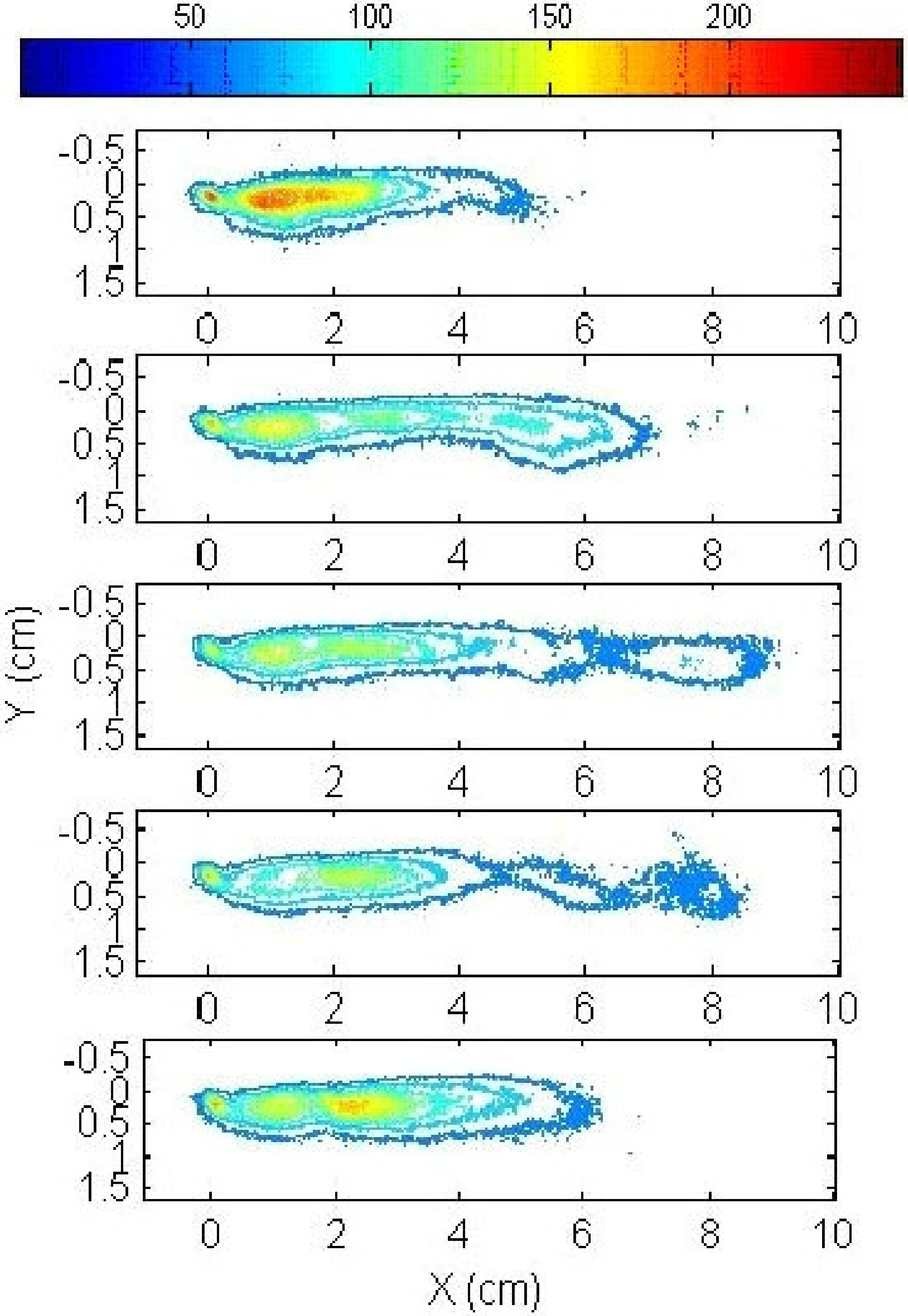

Figure 3.15: C_2* chemiluminescence intensity for Φ = 0.10, 0.15, 0.20, 0.25, 0.30 (top to bottom) and stagnation pressure of 0.86 MPa.

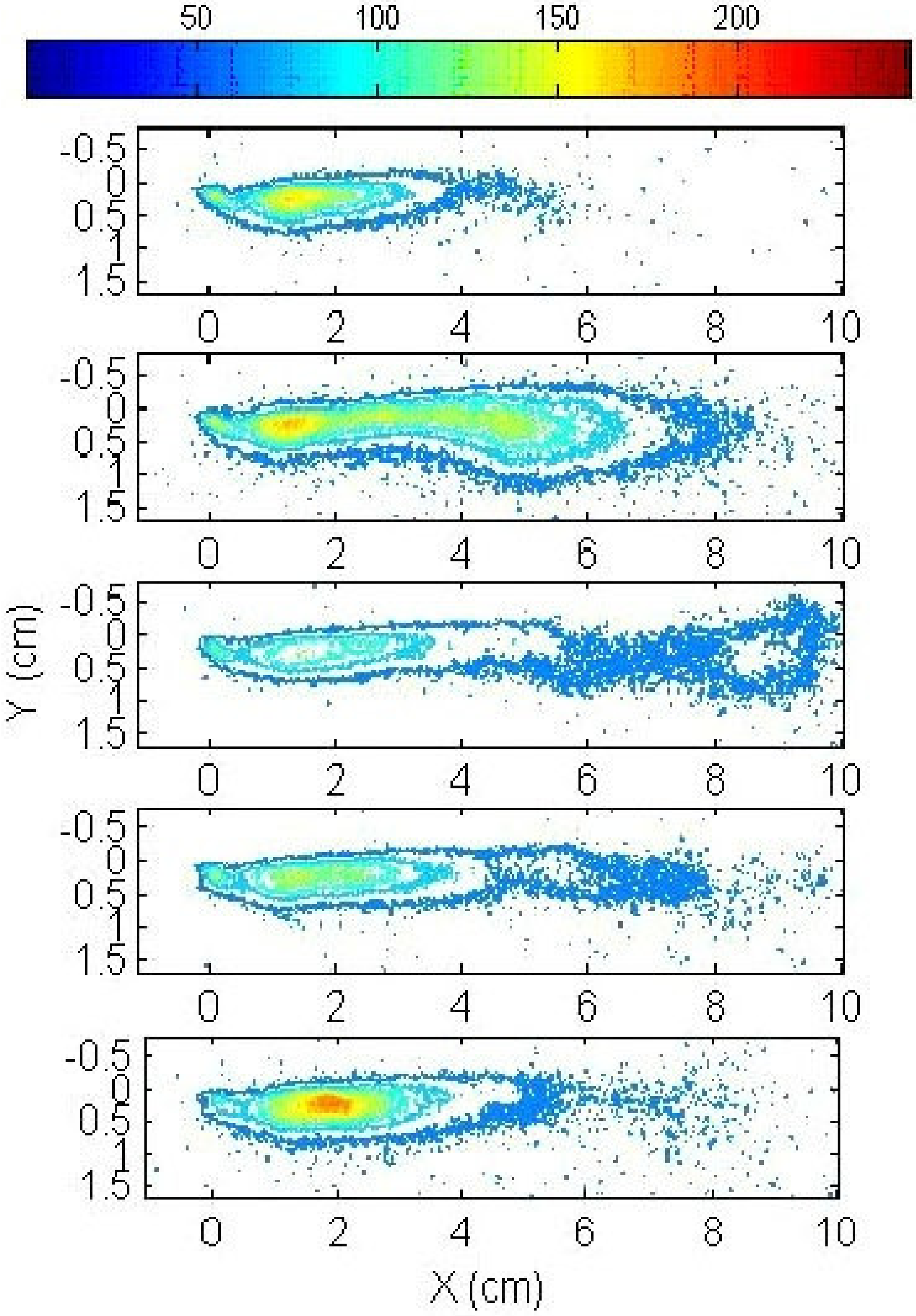

Figure 3.16: CH* chemiluminescence intensity for Φ = 0.10, 0.15, 0.20, 0.25, 0.30 (top to bottom) and stagnation pressure of 0.86 MPa.

3.2.3 Flame Penetration

It is clear from both the pressure traces and the chemiluminescence data that the combustor operates at its maximum when the equivalence ratio is between 0.20 and 0.25 contrary to the belief that the highest performance should occur at an equivalence ratio of one. This is true for combustors in which the fuel has spread throughout the entire combustor. It is likely that the fuel injected does not penetrate the entire combustor flow field. Therefore, the local equivalence ratio in the area of the combustor where the fuel has spread could be much greater than the measured equivalence ratio. If the area which the flame occupies is near 25% of the total combustor area, the local equivalence ratio would be near one for Φ=0.25, explaining the peak performance. Evidence of this is seen in the chemiluminescence images, the flame does not occupy the entire height of the combustion test area.

3.2.3.1 High Speed Images

With the pressure traces and chemiluminescence images collected, the high-speed camera was employed in visualize the flame and to estimate the area it occupied. A neutral density filter with an optical density of 1.0 was placed in front of the pilot injection site so the image obtained would not become over saturated. One image of the test section was taken prior to testing with a grid containing cells of 0.635 by 0.635 cm attached to the quartz window. This image was then superimposed on all of the images taken of the reacting flow field for analysis. Figure 3.17 shows an example of an image collected using the injection ports on the backside of the combustor. In other words Figure 3.17 looks directly into the pilot flame. The view gives details about the amount of lateral spreading the flame experiences. Figure 3.18 is an example of an image collected under the same test conditions but with the injection at the top of the combustor. In Figure 3.18 it can be seen that the flame begins to have a distinct change in shape. This is behavior is believed to be a result of a shock terminating the supersonic flow. The grid provides confirmation that this behavior is occurring approximately 50-mm downstream of the pilot injection, the same location an adverse pressure gradient is measured on the combustor wall.

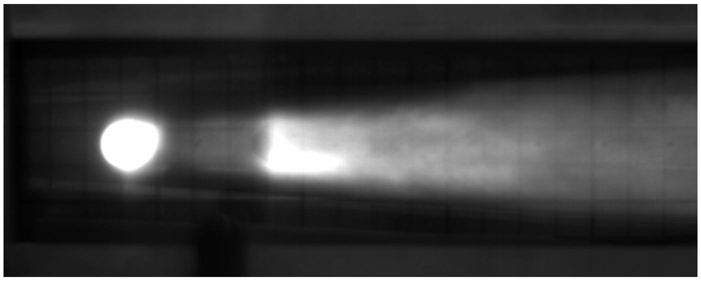

Figure 3.17: Φ=0.25 side injection, stagnation pressure of 0.93 Mpa.

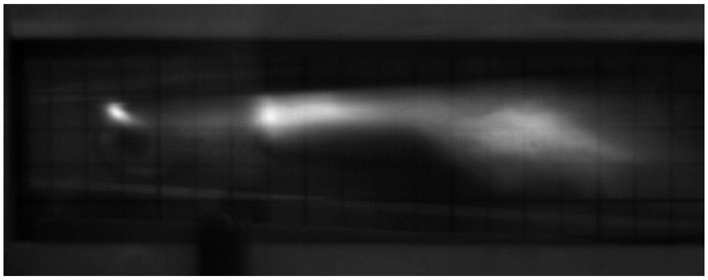

Figure 3.18: Φ=0.25 top injection, stagnation pressure of 0.93 Mpa.

Analysis of Figure 3.17 and Figure 3.18 provides an estimate of the amount of area the flame occupied compared to the total amount of area available in the combustor. This is accomplished by determining how much of the grid is occupied by a visible flame. The estimate indicates that roughly 27±2% of the total area of the combustor was occupied by the flame at x=50mm where the flow was deemed still supersonic. The estimate is based on creating a “rectangular flame shape” shown in Figure 3.19, whose extent was determined by the local flame characterization. This could over-estimate the affected area since the fuel penetration and spreading would most likely result in an elliptic shape. For this reason, the pressure traces showing an optimum combustion process occurring near an equivalence ratio of 0.25 are validated. Since penetration and lateral spread of the fuel only occupies one-fourth of the combustor, one could only expect to have optimum combustion near an equivalence ratio of 0.27, since this would correspond to a local equivalence ratio of 1.0. Images from other test conditions showed similar flame coverage. This is because the pilot flame is held constant in all cases for any given core air stagnation pressure. Furthermore, since the penetration of the pilot flame and fuel only allows for flame coverage of 25-30% of the combustor area, any further addition of fuel will not change the amount of fuel that can be combusted within the supersonic region; explaining why tests with equivalence ratios above $\Phi = 0.25$ all showed a decrease in combustor performance.

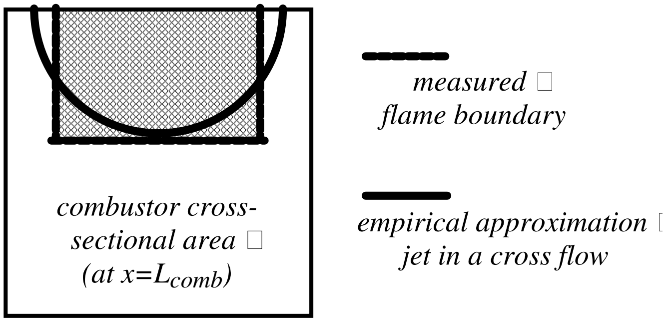

Figure 3.19: Diagram of estimated flame shape.

3.2.3.2 Empirical Analysis

To further validate this finding, an analysis was performed utilizing some existing empirical data to determine penetration depths. The estimates from the images suggested a penetration depth of about 8.3 mm at an axial location of approximately 50 mm. The key parameter governing the flow field a jet in cross flow is the square root of the momentum flux ratio, defined by Equations [13] and [14] in section 2.2.1.3.

Table 3-3: Pilot jet penetration summary.

	Fuel	Free Stream (Upstream)	Free Stream (Downstream)
ρ (kg/m^3)	0.268	2.24	1.07
V (m/s)	1210	726	949
Penetration, y, (mm)	N/A	9.6	8.9
Penetration Measurements (mm)			
High Speed Image	8.3	Chemiluminescence	8.0

The fuel stream properties were determined using the calculated and measured gas properties as shown in Table 3-1 and Table 3-2. The free stream properties were determined by using the pressure traces and isentropic relationships since the area ratios were known. The properties were determined at two locations, the pressure port just upstream and just downstream of the injection of the pilot flame. The penetration distances at an axial location of 50 mm were then calculated using Equation [14] and tabulated in Table 3-3. As Table 3-3 shows, Gruber's, et al.[54]

empirical correlation provides very reasonable agreement to what was observed in these experiments. For the upstream location, the correlation is within 13% of the observed, and the downstream location is within 7% of the observed. This analysis seems to support the idea that a relatively low equivalence ratio would be optimum for this configuration since the penetration of the pilot flame and main fuel injection can only influence 25-30% of the combustor area, meaning that the air in the remaining portion of the combustor is not utilized.

4 Fuel Injection Studies

Experimental investigation of two common fuel injection schemes, normal and ramped parallel into a Mach 2 flow was conducted. The characteristics of both fuel injection schemes was studied and used to create a new injection method, Fin-Guided Injection. The Fin-Guided injection was developed to take advantage of the positive characteristics of each injector, including penetration from the normal injection scheme and mixing enhancement caused by the ramp in the parallel injection schemes. By injecting fuel at an angle the Fin-Guided tests were also able to add axial momentum to the overall vehicle thrust. The Fin-Guided tests increased the amount of fuel penetration while at the same time reducing the flow losses incurred from injection, and easily outperformed the two baseline tests studied.

4.1 Apparatus and Experimental Setup

A study of various schemes to inject fuel into a supersonic crossflow was conducted on the non-reacting test stand in the APRL. In total, four different schemes were investigated; two baselines schemes, normal injection and parallel injection through a ramp, and two novel Fin-Guided injection schemes. All four schemes were tested in the same supersonic duct. The duct receives shop air and expands it through a Mach 2 nozzle. Figure 4.1 shows a basic diagram of the rig. Downstream of the nozzle the top and bottom walls diverge as in a supersonic combustor. The four injection schemes are tested upstream of a second expansion and are monitored using pressure traces, Schlieren and Mie-scattering.

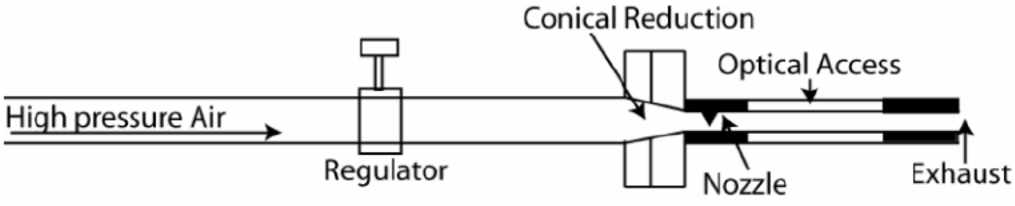

Figure 4.1: Basic schematic of fuel injection rig.

4.1.1 Hardware and Design

The nonreacting test stand in the APRL is supplied compressed air in the same manor in which the reacting test stand described in section 3.1.1. An Atlas Copco Compressor is used to deliver high pressure air to the 5.1 cm steel pipe air lines in the laboratory. The air mass flow is controlled using a similar ball valve and Wilkerson screw type regulator as in the reacting test stand. A Setra Model 206 static pressure transducer is used in conjunction with a Datum 2000 dual channel display to monitor the air pressure. The maximum flow rate of air to the lab is 0.23 kg/s at 1.14 Mpa.

A 2 meter long 5.1 cm steel pipe brings the supply air to the supersonic duct from the regulator. The pipe is then mated to the same custom milled, aluminum transition block used in the scramjet combustion rig. The transition block uses a 5.1 cm long conical reduction to bring the airflow cross-section from the pipe diameter to a 1.27 cm square cross section. Connected to the transition block is the front block. As with the Scramjet Combustion rig, the front block mates the transition block to the combustor test section and houses a flow straightener. Figure 4.2 shows the Fuel Injection rig on test stand. A greater detail description of the air supply and transition and front blocks can be found in section 3.1.1.

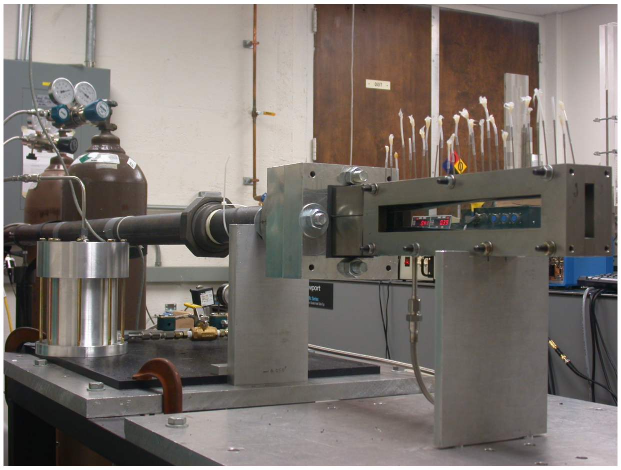

Figure 4.2: Picture of fuel injection rig on the nonreacting test stand in the APRL.

The Fuel Injection Rig is put together using four parts; a top plate, bottom plate and 2 window holders. When assembled the flow path created by the rig starts with a 1.27 cm by 1.27 cm. The width of the flow path remains at 1.27 cm throughout the entire length of the rig, however the height of the rig varies; starting with the converging-diverging. The nozzle is located 3.81 cm downstream of the front block and restricts the flow path to a 1.27 cm by 0.75 cm rectangle. The nozzle diverges back to 1.27 cm by 1.27 cm, accelerating the flow to Mach 2.0. The top and bottom walls expand by 3.5° for 3.80 cm, increasing the duct height to 1.72 cm. The area remains constant for 3.18 cm before the top and bottom walls resume expanding by 3.5° for the remaining length of the duct, 28.56 cm. The fuel injection for all schemes studies is located at the edge of the constant area section, tangent to the second bottom wall expansion. Figure 4.3, while not to scale, provides a basic view of the fuel injection rig flow path and provides dimensions.

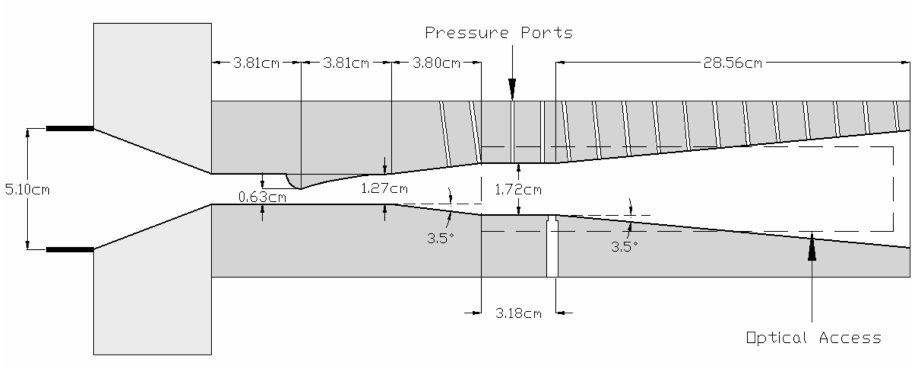

Figure 4.3: Basic diagram of the fuel injection rig.

As seen in Figure 4.3, the top plate houses the nozzle and 22 0.10 cm diameter pressure ports. The pressure ports are perpendicular to the top wall of the duct and are spaced 1.27 cm apart. The bottom plate houses the fuel injection scheme. Four bottom plates were fabricated, one for each fuel injection scheme. Shown in Figure 4.3 is the normal injection bottom plate. The injectors for each scheme are all located in the constant area section of the duct and have use 0.318 cm choked orifices for sonic injection of the fuel. The injector channel widens to 0.493 cm to allow a steel pipe with a 0.490 cm outer diameter to be inserted and welded in place. The welded pipe has standard pipe fittings and is connected to the fuel lines which bring the helium to the duct. Diagrams for each of the injectors are provided in the following sections.

4.1.1.1 Normal Injection

The geometry of the supersonic duct is not changed at all for normal injection, as displayed in Figure 4.4. The injector is located so that it is tangent with the 3.5° expansion along the bottom wall. The injector diameter is 0.318 cm. The injector port is the choked orifice which is used to create sonic fuel injection and to control the massflow.

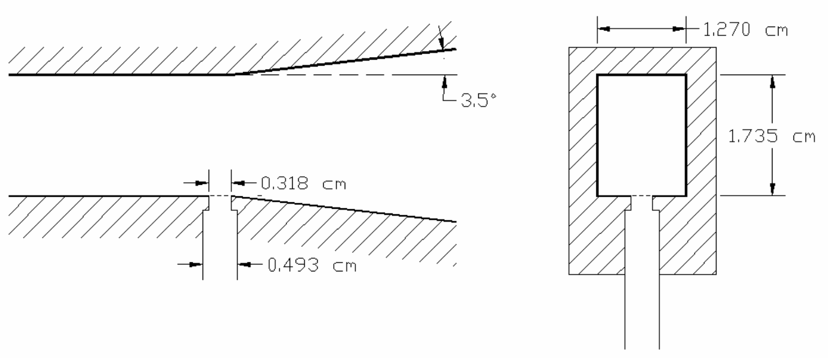

Figure 4.4: Basic diagram of normal injector.

4.1.1.2 Ramped Parallel Injection

The parallel injection bottom plate is more complicated. Figure 4.5 shows the parallel injection scheme in detail. A triangular ramp is located on the flat section of the combustor. It rises at approximately 28° until reaching a height of 1.185 cm, and expands laterally at 11° until reaching a width of 0.953 cm. The dimensions of the strut were determined by the desired height of injection as well as the structural requirements of housing the 0.318 cm injector. The injector is located at a height of approximately 0.868 cm, which is the center of the combustor.

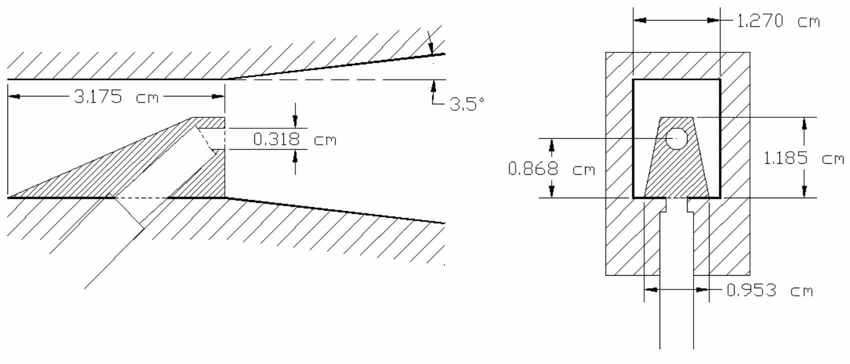

Figure 4.5: Basic diagram of ramped parallel injector.

4.1.1.3 90° Fin-Guided Injection

The fin is a thin wedge shaped blade with an inclination angle of 30°. The 30° inclination angle was chosen for reasons described in reference.[13] The fin has a maximum width (W) of 0.318 cm, same as the injection diameter, and a height (h) of 0.868 cm, which is half of the combustor height and 2.7 times the injection diameter. The length (l) of the pylon is 1.503 cm. Figure 4.6 shows the shape of the fin used. The fin inclination angle (theta) was fixed at 30°, this value was determined as the optimal angle by numerical studies done by Guoskov, et al.[68]

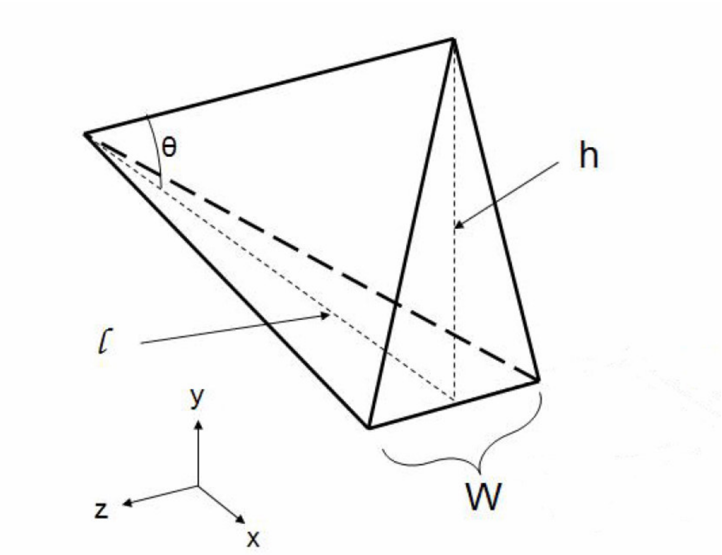

Figure 4.6: Diagram of fin geometry.

The injection orifice diameter for the 90° injector scheme is 0.318 cm, and is located such that it is tangent to the location of the second expansion and the edge of pylon, as seen in Figure 4.7.

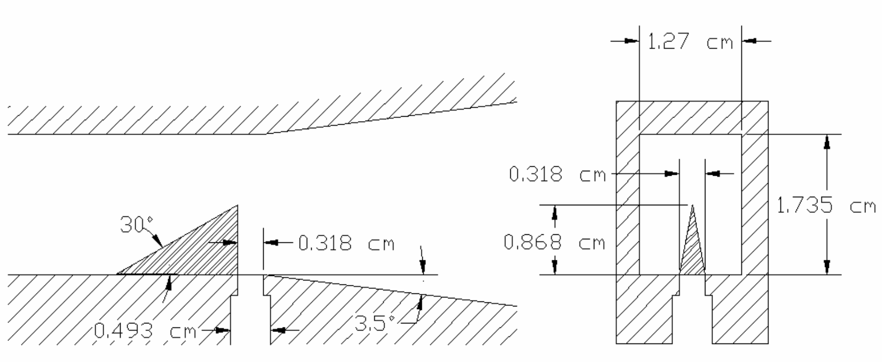

Figure 4.7: Basic diagram of 90° Fin-Guided injector.

4.1.1.4 45° Fin-Guided Injection

The fin geometry used for 45° injection is exactly the same as with the 90° Fin-Guided injector shown in Figure 4.6. The injection channel has a diameter of 0.318 cm as with the other injection schemes but is angled at 45° to duct wall. The projection of the 0.318 cm diameter orifice at 45° on the bottom surface creates an oval with major axis of 0.450 cm. Therefore in order to have the injection port tangent to the expansion edge and the pylon, the pylon must be moved back 0.450 cm from the expansion edge, 0.132 cm further than the 90° case, as depicted in Figure 4.8.

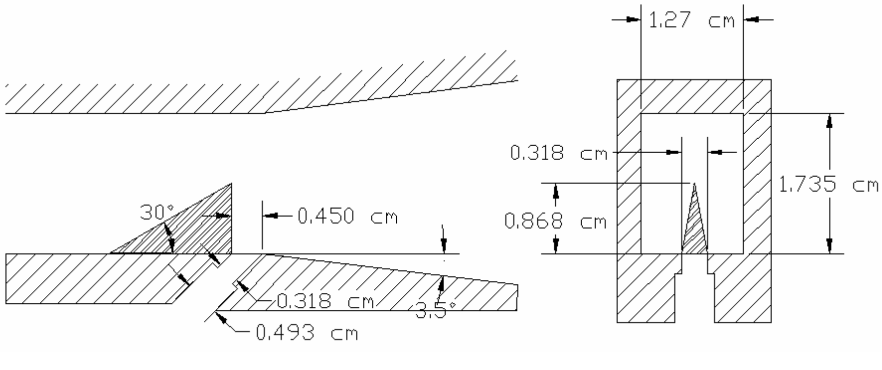

Figure 4.8: Basic diagram of 45° Fin-Guided injector.

4.1.2 Diagnostics

4.1.2.1 Pressure Measurements

A Scanivalve Corporation DSA-3217 Digital Sensor Array was used to make static pressure measurements at all of the pressure ports along the top wall of the combustor. This Array consists of 16 temperature compensated piezoresistive pressure sensors with a pneumatic calibration valve. The 16 sensors, or channels, all have a range of 0-1.5 MPa. Their associated error is ±0.2% of scale for pressures less than 0.1 MPa, ±0.12% of scale for pressures between 0.1 and 0.14 MPa, and ±0.05% of scale for pressures above 0.14 MPa. The measured pressures are sent via a TCP/IP connection to a desktop computer and into a LabView virtual control panel. This virtual interface (VI) allows for monitoring of all 16 channels and the DSA's settings as well as writing of the data to a text file to be read by post-processing software.

4.1.2.2 Schlieren

Schlieren visualization was employed to investigate the mixing characteristics of the fuel injection systems and the flow structures created by them. The Schlieren configuration consisted of a 20 watt continuous light source reflected by a 15.24 cm diameter concave mirror through the test section. The light was collected by an identical mirror perpendicular to the test section and directed to a horizontal knife edge where the light was filtered. A Cooke Corporation Dicam Pro ICCD camera was used to collect the filtered light from the knife edge and digitize the images using a desktop computer. The ICCD has a shutter speed as short as 3 ns and is operated at a frame rate of approximately 8 Hz. The shutter speed was varied between test to acquire instantaneous and time-averaged images. Figure 4.9 lays out the setup used to collect the Schlieren images. The images were analyzed using the image processing toolbox of MATLAB to plot the intensity maps as a measure of fuel penetration and fuel spreading.

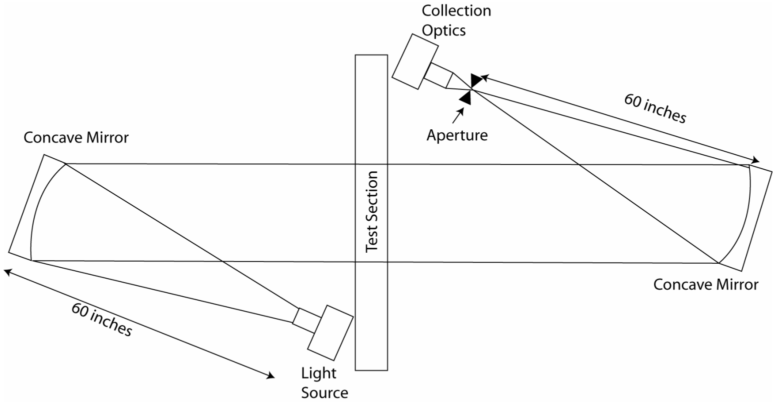

Figure 4.9: Basic diagram of the schlieren setup.

4.1.2.3 Mie-scattering

Two different schemes were employed to collect Planar Mie-scattering images for the fuel injection studies. The two methods varied in the manner in which the flow was seeded. The first method utilized ethanol as the seeding material. An ethanol spray was injected into the fuel on route for injection into the supersonic duct via a pressurized vessel with an exit orifice of 0.23 mm. The ethanol would vaporize in the fuel line before being injected into the duct crossflow. The ethanol condenses when it mixes with the supersonic crossflow which is at a temperature much cooler than the temperature of the ethanol. For the Mach +2 conditions run in the combustor tested in this experiment the static temperature of the crossflow is below 166K, when the ethanol mixes with air at this temperature its own temperature drops below its saturation temperature and condenses. This method know as, Product Formation, has been used by many, including Messersmith, et al.[70] and Clemens, et al.[71] who used a two color transmission measurement to determine the average size of condensed ethanol droplets. The measurement resulted in a conservative estimate of droplet sizes of 0.15μm as well as stokes numbers less than 0.005 indicating the particles are small enough to provide satisfactory flow visualizations according to Clumpner.[72]

The second seeding method used a Viper II smoke machine to seed entrained air into the combustor. The smoke was injected into the combustor through the injector port to simulate fuel injection, by utilizing the low pressure suction downstream of the fin. The average particle size of the smoke is roughly 10 μm, the calculated stokes numbers were less then 0.01 with a length scale of 3 mm.

A Solo Nd:YAG laser was used to create a thin laser sheet. The Solo Nd:YAG laser was operated at 532nm and a maximum energy output of 120mJ with pulse duration of 3-5 ns full width half maximum, short enough to freeze the flow field. The laser sheet was passed through the test section perpendicular to the crossflow through quartz windows on the combustor side walls. The light scatter from the smoke and ethanol particles passing through the laser was then captured using a FASTCAM-Ultima1024 model 16K high speed camera. The images show the lateral and vertical mixing of the fuel into the combustor crossflow. The laser sheet was aligned at the injection point and then traversed to locations ranging 1-12 injector diameters downstream to image both near field and far field mixing. For the parallel injection scheme 3 injector diameters is approximately equal to the ramp height.

4.1.3 Experimental Procedure

The Wilkerson regulator was used with the Setra static transducer and Datum 2000 digital display to set to set upstream stagnation pressure and flow conditions to within ±6.9 kPa. Data was collected using several upstream conditions, however only the 0.66 MPa upstream stagnation pressure tests are presented in this document. More on the other conditions can be seen in the Appendix. With a stagnation pressure of 0.66 MPa the massflow rate of air was 0.146 kg/s. Helium is used as the simulated fuel and is injected at sonic conditions through choked orifices of 0.318 cm diameter into the duct. The helium, referred to as the simulated fuel or fuel, is fed to the combustor by a pressurized supply bottle via 0.493 cm supply lines and is operated by a direct acting electronically controlled valve. The fuel pressure is monitored using a Setra static pressure transducer fed to TCP/IP desktop connection and recorded using LabView. The fuel was injected at varying massflow to create a series of test conditions shown in Table 4-1. The LabView is also used to collect and record the data measured by the 16 pressure channels on the DSA pressure module described earlier. All pressure ports on the duct which were not used were capped.

Table 4-1: Flow conditions tested in the supersonic duct.

$\dot{m}_{air}$ ($\frac{\text{kg}}{\text{s}}$) ± 0.002	$\dot{m}_{\text{fuel}}$ ($\times 10^{-3}\,\frac{\text{kg}}{\text{s}}$) $\pm 0.05\times 10^{-3}$	$\frac{\dot{m}_{fuel}}{\dot{m}_{air}}$	*Fuel x-Momentum Flux* $\times 10^5\,\frac{\text{N}}{\text{m}^2}$		*J* Momentum Flux Ratio	
			45°	Parallel	45°	90°
0.146	0	0	0	0	0	0
0.146	1.98	0.014	1.11	2.22	0.55	0.78
0.146	3.26	0.022	1.81	3.61	0.71	1.00
0.146	4.26	0.029	2.37	4.73	0.80	1.13

The 'Fuel x-Momentum Flux' parameter refers to the momentum flux added to the combustor by the fuel injection in the direction which produces thrust. Its value is 0 for all of the 90° injection cases, but has a value when fuel is injected at 45° or parallel to the air cross flow. In the parallel fuel injection scheme the full fuel momentum is added to the vehicle thrust. The value *J* in the table is the jet-to-freestream momentum flux ratio found using Equation [13]. The jet values correspond to the injected fuel parameters while the freestream terms are the combustor crossflow parameters.

The momentum flux ratio is a controlling parameter for transverse injection schemes; the greater the momentum flux the greater the penetration of the jet into the crossflow and has been used by Gruber, et al.[54] characterize transverse injection. Since used to describe normal, or 90° injection, the value is modified for the 45° injection schemes so only the fuel momentum flux in the *y*-direction is used in the ratio. For parallel injection schemes *J* has no value or meaning.

4.2 Baseline Fuel Injection Studies

4.2.1 Results

4.2.1.1 Wall Pressure Distributions

The duct wall pressures were recorded using the DSA described earlier. Of the 16 pressure channels available on the DSA for making measurements, 1 was used to measure the atmospheric pressure, while the remaining 15 were used to measure the wall pressures in the region downstream and upstream of the injection location. The pressure traces plotted are averaged from the data collected by the DSA. The DSA measurement error is less then the standard deviation of the data used for averaging, and therefore the standard deviation is used to make the error bars. A summary of the tests conducted for the normal injection scheme is presented in Figure 4.10. The core air mass flow is set to 0.146 kg/s while the fuel injection massflow is varied between 0 and 4.26 g/s. A true-scale schematic of the supersonic duct is provided in the figure in order to understand the flow properties. The x-axis has been normalized with the injection diameter. The $x/d = 0$ location corresponds with the back edge of the fuel injector as shown in Figure 4.10.

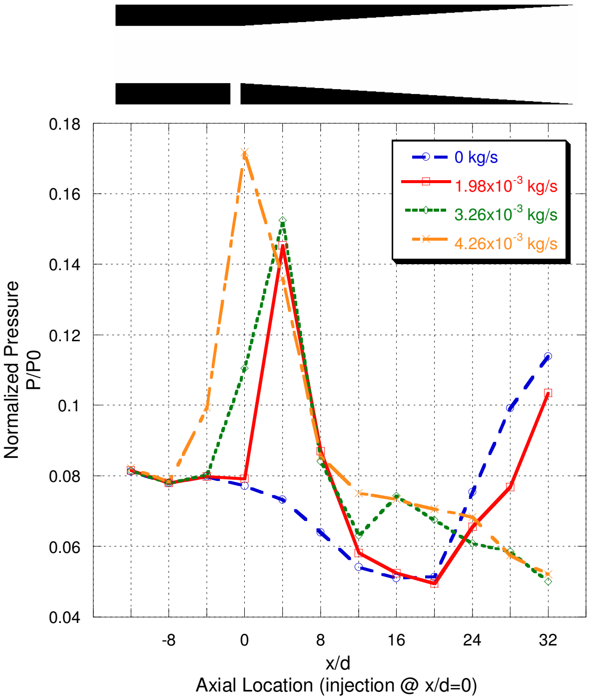

Figure 4.10: Normalized wall pressure distribution for normal injection.

When no fuel is injected into the combustor the pressure remains relatively unchanged in the constant area section upstream of the injection point. Downstream of the injector where the top and bottom walls begin to expand the pressure slowly decreases until *x/d*=20 when the pressure begins to rise. This pressure rise is most likely caused by the boundary layer separation effects as the flow is no longer supersonic everywhere and begins to transition to subsonic. When fuel is injected into the combustor the supersonic range is increased as the boundary layer separation is delayed. The flow does not begin its transition to subsonic conditions until *x/d*=32 in the conditions where the most amount of fuel is injected. However, there is a clear and prominent pressure spike located at the injection point for cases when fuel is injected. This is caused by the bow shock formed by the fuel column injected into flow. The pressure rise caused by the fuel column blockage and corresponding shock increases as more fuel is injected. The pressure rise also begins to propagate upstream of the injection location as more fuel is injected. Rogers[53] has done extensive studies on normal injection and have explained this to be caused by the separation zone located upstream of the bow shock which forms from the fuel column. This is illustrated in Figure 2.4.

The techniques described in section 2.2.1.2 can be used to analytically estimate what the pressure trace would look like. Using the Area-Mach relationship and the isentropic pressure relation the static pressure distribution can be determined for the geometry of the duct studied. Figure 4.11 shows the analytically estimated pressure distribution derived from the method described in section 2.2.1.2 versus the pressure trace found experimentally for the case where no fuel is injected into the cross flow. The analysis initially follows the experimental results closely, except for some peaks and troughs in the experimental data caused by reflected waves. However, at x/d=15 the two diverge drastically. This is because the boundary layer begins to separate, causing a large pressure rise, and eventually leads to the flow becoming subsonic. This is not accounted for in the analytical estimate, which shows the flow continuing to expand, dropping static pressure.

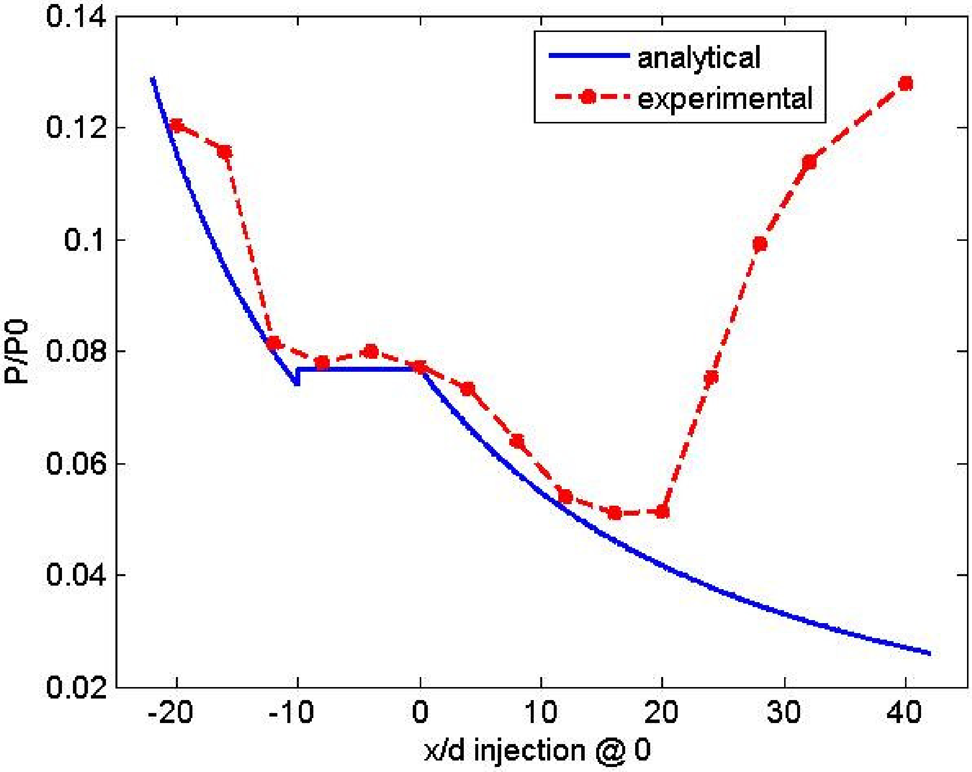

Figure 4.11: Analytical estimate versus experimental pressure trace with no fuel injection.

Figure 4.12 shows the analytically derived pressure distribution versus the pressure trace found experimentally with fuel injection at 4.26 kg/s. There are two analytical estimates shown, one matches the peak pressure caused by injection, the second matches the downstream expansion of the flow. Neither analytical estimate follows the experimental pressure distribution well. The analysis does not take into account the local boundary layer separation near the injection, causing pressure rises to propagate upstream. Peaks and troughs in the experimental results are seen for this test case as well, again caused by the reflected waves. While the experimental peak pressure can be matched by varying the strength of the estimated shock, the downstream data does not match well. In the case where the downstream condition is matched for both cases, the peak pressures for the analytical estimate is significantly lower than the experimental data shows.

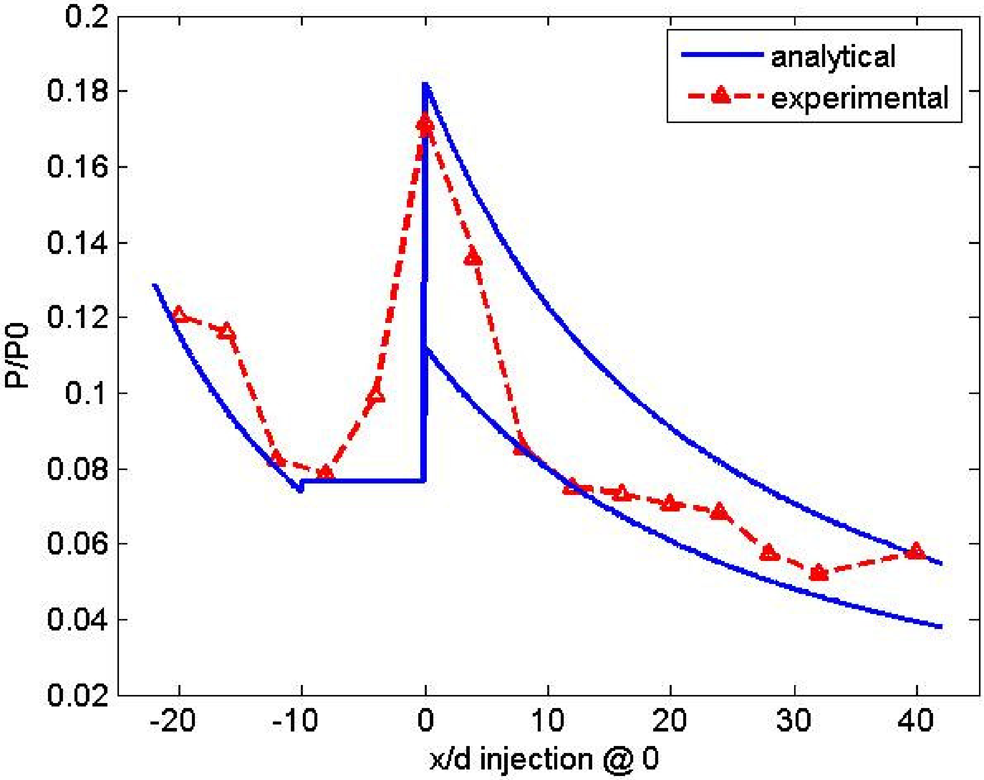

Figure 4.12: Analytical estimate versus experimental pressure trace with fuel injection at 4.26 g/s.

The quasi one dimensional analysis differs so greatly from the experimental data set, because it can take into account of the three dimensional effects of the fuel injection column, such as three dimensional relief. Nor does the analysis consider any viscous effects, such as the development of boundary layers, and eventual boundary layer separation. Also over looked in the analysis is the effect of reflected shock waves in the duct. These reasons make it difficult to successfully estimate the exact pressure distribution from a fuel injection system, without conducting a full computational model.

The wall pressure distributions for the parallel injection tests shown in Figure 4.13 are very different from the normal injection tests. There is a very high pressure rise upstream of the injector caused by the ramp. This pressure rise is followed by a very sharp drop in pressure downstream of the ramp. This is caused by the large expansion at the face of the ramp. The flow initially compressed by the ramp is not expanded supersonically in the region downstream of the ramp causing the pressure to fall. As with the normal fuel injection tests conducted, the flow remains supersonic for a greater distance when additional fuel in injected, in fact for the case where the greatest amount of fuel is injected the flow remains supersonic for the entire test section in which wall pressures are taken. There is a small pressure spike downstream of the injection which increases with the amount of fuel injected downstream of the injector, caused by the fuel flow blockage, however this spike is only a small fraction of the pressure rise associated with the pressure rise due to the ramp. The flow losses caused by the ramp are significantly greater than the losses from the parallel fuel injection; unlike in the normal injection tests where the pressure loses are directly influenced by the fuel injection massflow.

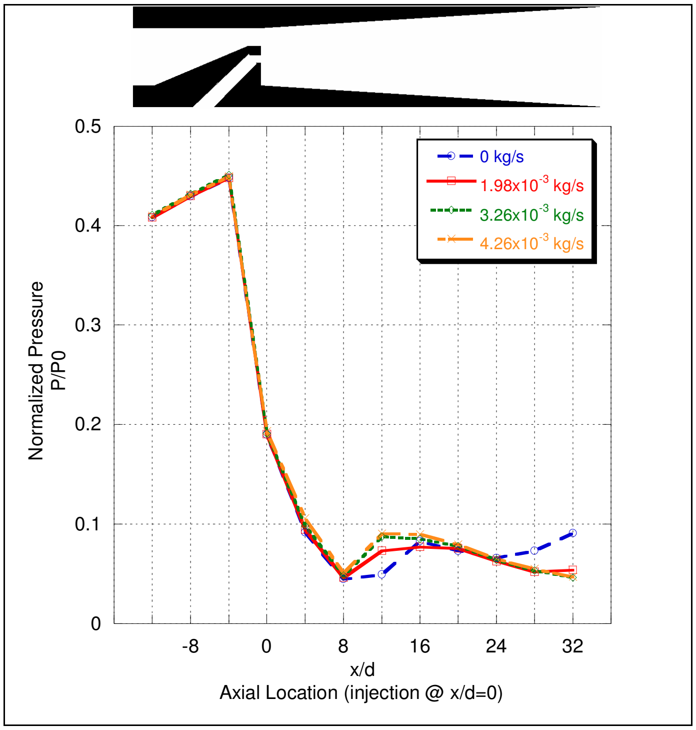

Figure 4.13: Normalized wall pressure distributions for ramped parallel injection.

The maximum pressure rise caused by the ramped parallel fuel injection is 250-300% larger than the maximum pressure rise found in the normal injection. Some of the pressure rise incurred in the parallel injection case is caused by the ramp compression, which decreases the Mach number of the flow over the ramp, thus causing the pressure to rise. While this pressure rise may occur without any loss in total pressure, the experimental pressure rise is much greater than if the ramp provided isentropic compression shown in Figure 4.14. This means that the pressure rise over the ramp is caused by the compression, and due to shocks forming on the ramp, the shocks are responsible for the majority of the pressure rise, and are associated with total pressure losses.

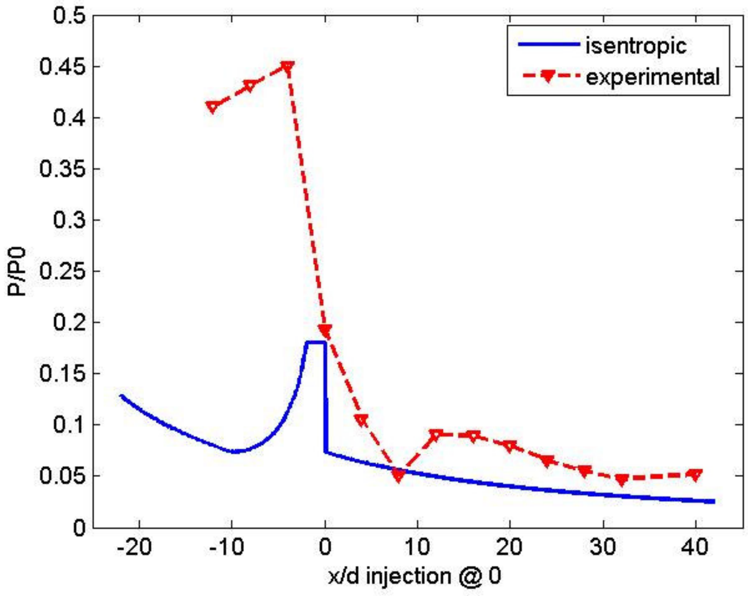

Figure 4.14: Experimental pressure trace versus isentropic static pressure rise.

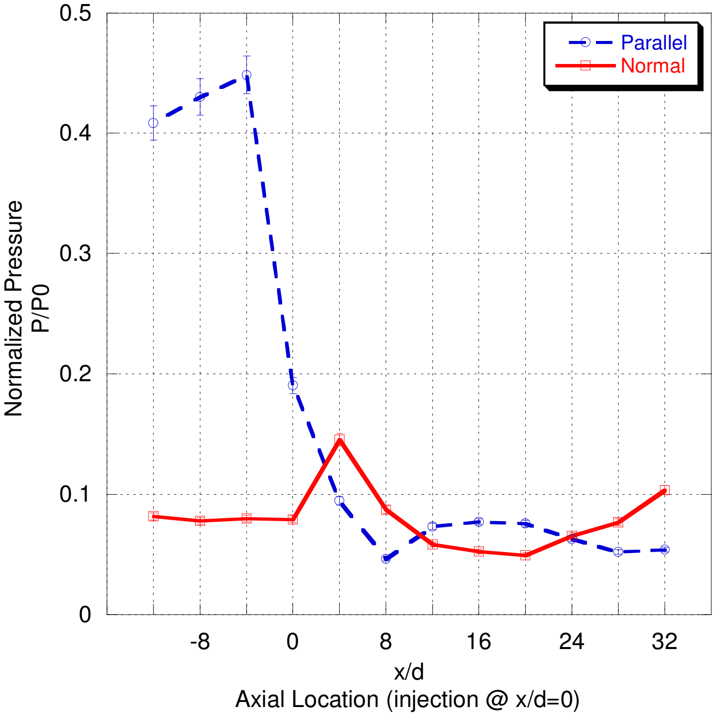

Figure 4.15: Comparison of normal and parallel injection wall pressure distribution ($\dot{m}_{\text{fuel}}$ = 1.98x10^{-3} kg/s).

Illustrated in Figure 4.15 are the pressure traces for both fuel injection schemes with the fuel injection massflow at 1.98 g/s for both tests. The stark contrast in the wall pressure is clearly observable. While the pressure spike in the normal injection tests varies with the momentum of the fuel injection the pressure rise in the ramped parallel injection is unchanging as it is fixed by the geometry of the ramp.

4.2.1.2 Schlieren

In order to visualize the flow structures within the combustor when each injection scheme is employed Schlieren images have been collected. The images show the location of expansion fans, oblique shocks, boundary layer effects, as well the location of the fuel once injected. As with the pressure traces, the x and y axes have been normalized with the injection diameter. Instantaneous Schlieren images were collected in the manner described in section 4.1.2.2. Instantaneous images taken of the normal injection tests are displayed in Figure 4.16.

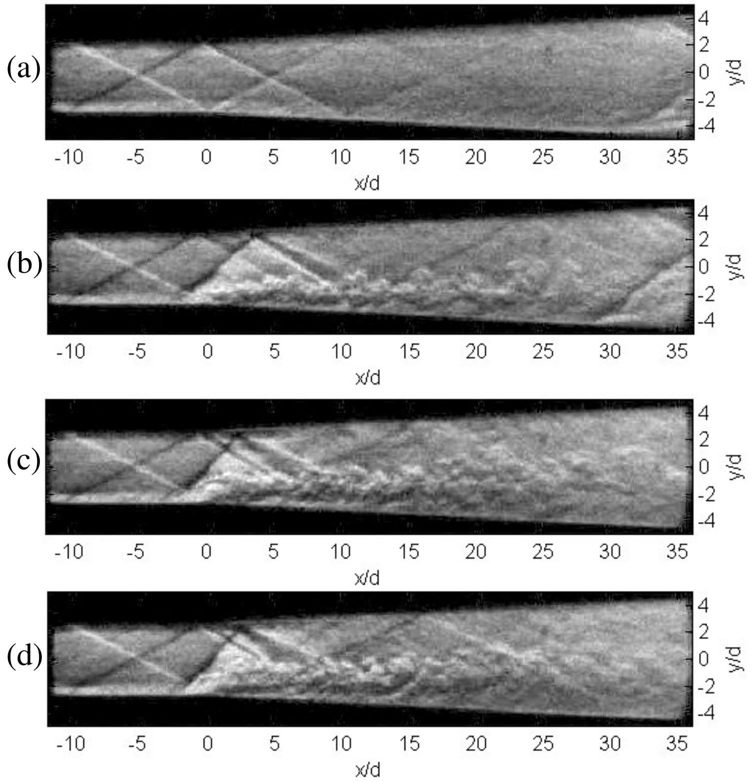

Figure 4.16: Normal injection instantaneous Schlieren images (a) no fuel (b) $\dot{m}_{\mathrm{fuel}}$ = 1.98x10^{-3} kg/s (c) $\dot{m}_{\mathrm{fuel}}$ = 3.26x10^{-3} kg/s (d) $\dot{m}_{\mathrm{fuel}}$ = 4.26x10^{-3} kg/s.

In Figure 4.16 (a), where no fuel is injected, the oblique shock waves beginning at the end of the first expanding section of the duct and start of the constant area section are seen; as are the expansion waves forming at the second wall expansion located at the fuel injector. The waves are reflected throughout the combustor. At approximately *x/d*=30 another shock can be seen, this shock the onset of the boundary layer separation and the flow's transition to subsonic. In the three images shown with fuel injection an oblique shock can be seen forming upstream of the fuel column. The shock angle becomes steeper as the fuel momentum is increased, as expected from the pressure traces. The fuel-air mixing is visualized as a turbulent process. The boundary of this mixing penetrated further into the combustor as the fuel momentum is increased. Figure 4.17 displays the instantaneous Schlieren images taken when the ramped parallel injection scheme is employed.

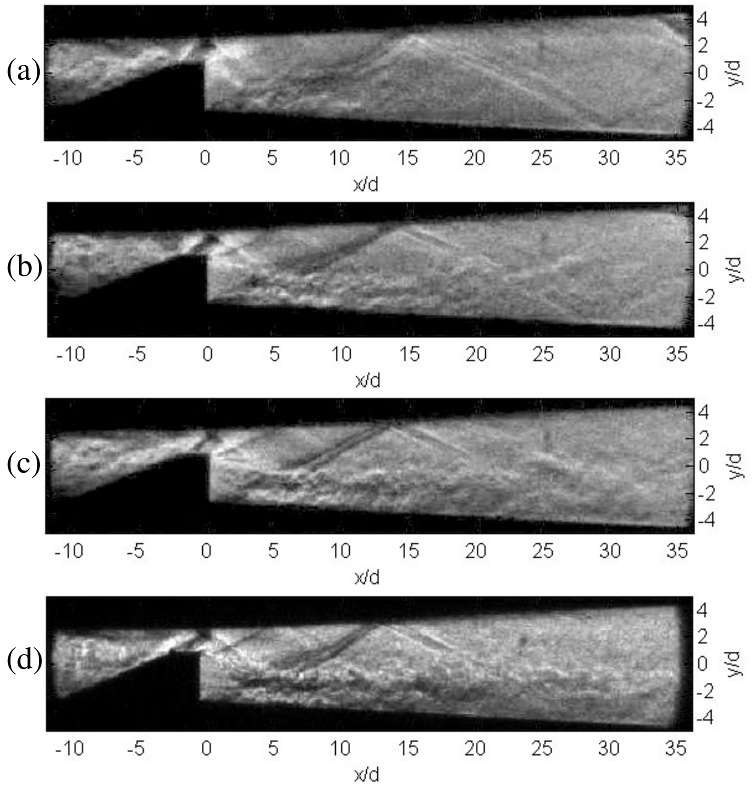

Figure 4.17: Parallel injection instantaneous Schlieren images (a) no fuel (b) $\dot{m}_{\text{fuel}}$ = 1.98x10^{-3} kg/s (c) $\dot{m}_{\text{fuel}}$ = 3.26x10^{-3} kg/s (d) $\dot{m}_{\text{fuel}}$ = 4.26x10^{-3} kg/s.

The condition where no fuel is injected shows a relatively turbulent flow compared to the normal injection case. The flow upstream of the ramp has large density gradients as shown by the Schlieren. The three dimensional effects of the shocks on the ramp have created a very complicated flow structure. The expansion fan on the top surface of the ramp is seen as is the fan on the bottom wall. The cases with fuel injection do not seem to vary at all; the flow structures all seem to remain constant. The fuel height does not seem to change with increased fuel momentum. This is because the level of penetration is achieved by the injection location on the ramp; the parallel fuel jet has no momentum to penetrate the crossflow by itself. In fact the fuel jet is pushed downwards by the core-air turning and expanding over the ramp in the parallel injection scheme. Time-averaged Schlieren images were take of the injection schemes as well. The time-averaged images of tests with fuel injection massflow of 1.98 g/s are presented in Figure 4.18 and Figure 4.19 for normal and parallel injection respectively.

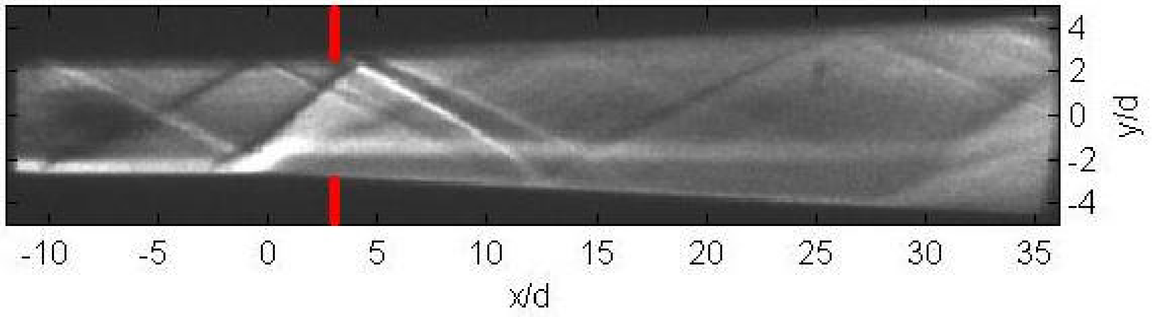

Figure 4.18: Time-averaged Schlieren image with normal injection ($\dot{m}_{\text{fuel}}$ = 1.98x10^{-3} kg/s).

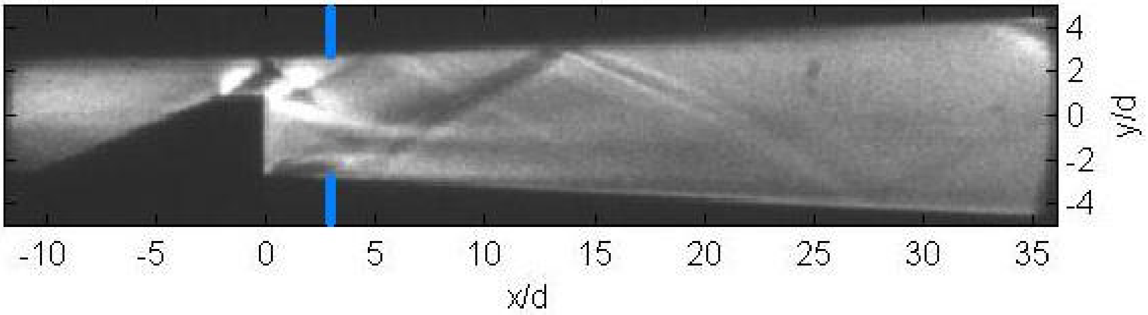

Figure 4.19: Time-averaged Schlieren image with parallel injection ($\dot{m}_{\text{fuel}}$ = 1.98x10^{-3} kg/s).

The white streaks shown in the time-averaged images are the locations of the fuel-air boundaries and correlate to the location of the fuel. The time-averaged image of the normal injection shows the fuel penetrating the crossflow until being turned in the direction of the combustor flow. In the parallel injection test the fuel jet is pushed downward after being injected in the combustor. The core air flowing over the ramp and then turning and expanding over the ramp when it ends flows down into the parallel fuel column and its momentum pushes the fuel down. There also seems to be a small amount of fuel which is pushed to the bottom of the combustor, as two fuel streaks are seen in the time-averaged image. The time-averaged images show the height of the fuel jet is greater in the parallel injection scheme than in the normal injection scheme. The intensity of the images between the red and blue bands are calculated and plotted versus the combustor height to further examine the fuel penetration for both injection schemes and is plotted in Figure 4.20. The strips defined by the red and blue bands represent the area roughly 3 injection orifice diameters downstream ($x/d = 3$) of the injection point.

The locations where the intensity is highest are the locations where the white streaks caused by the fuel-air boundary are located. Figure 4.20 verifies that the fuel penetration is much less for normal injection than parallel injection at $x/d = 3$. The technique used to generate Figure 4.20 is used to generate a map of the fuel-air boundary in the combustor until the location $x/d = 12$ and is shown in Figure 4.21.

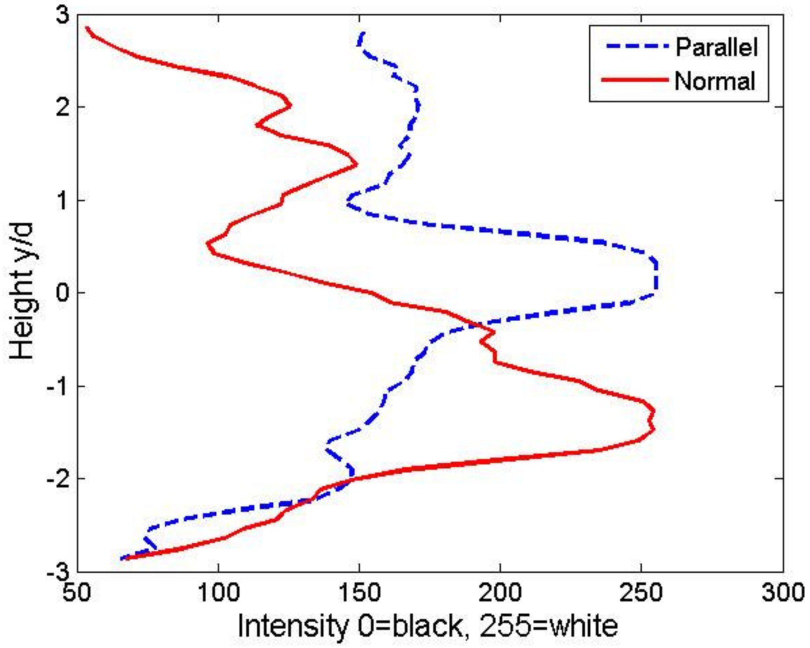

Figure 4.20: Intensity profile of time-averaged Schlieren images at *x/d*=3.

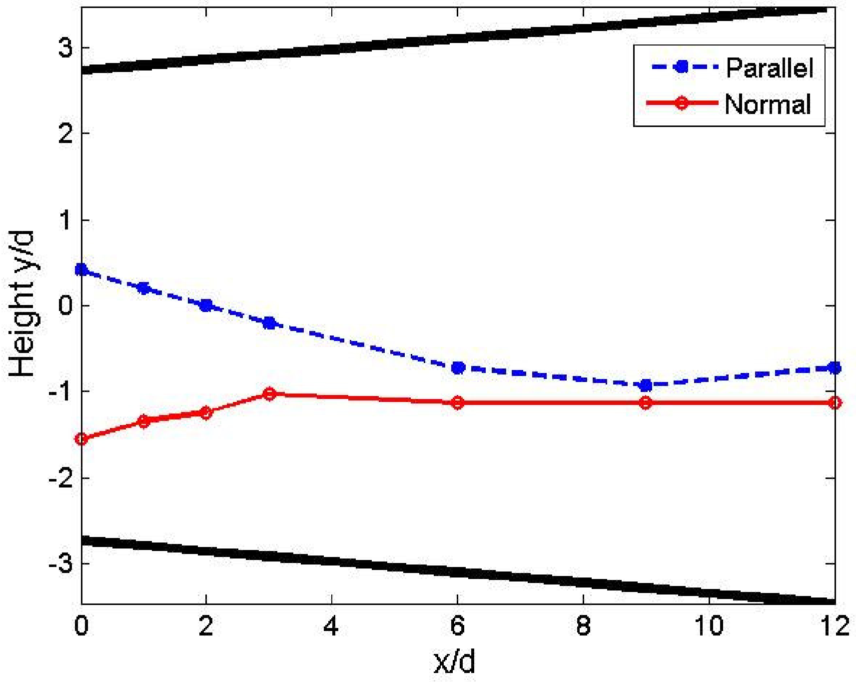

Figure 4.21: Fuel penetration versus axial location with $\dot{m}_{\mathrm{fuel}}$ = 1.98x10^{-3} kg/s.

The large black bands in the figure represent the location of the top and bottom walls within the combustor. The 0 location on the *y*-axis corresponds to exactly the half way point of the combustor height, as well as the center of the parallel injector. The 0 location on the *x*-axis still corresponds to the injector location on the bottom wall. The characteristics seen in the time-averaged images are better visualized. The fuel-air mixing boundary for the fuel injected parallel to the crossflow is initially located exactly at the edge of injector orifice. However the boundary begins to lose combustor height until it finally levels off at *x/d*=8. The normally injected fuel penetrated 1.5 diameters below the combustor centerline at the point of injection and penetrates to 1 diameter below the centerline before leveling out at *x/d* = 3. By *x/d*=12 the fuel heights of both injection schemes are very similar. However, in the near field the parallel injection achieves greater heights than normal injection.

4.2.1.3 Mie-scattering

The Mie-scattering images presented are not scalar conserved, and therefore all of the fuel in the combustor may not be visualized however, the images still provide a good estimate as to the location and spreading of the fuel as it flows through the combustor. Only the fuel has been seeded, therefore we can visualize how the fuel mixes in the combustor. The pulse of the Solo Nd:Yag laser used in the Mie-scattering images is 3-5 ns full width half maxim, sufficient enough to freeze the flow field for instantaneous images. Two such instantaneous images are shown in Figure 4.22. The images are taken at *x/d*=3 or 3*d* downstream of the injector. The images verify the penetration heights calculated from the time-averaged and instantaneous

Schlieren images and the corresponding intensity plot. The images also help visualize the various flow patterns the fuel injection takes on.

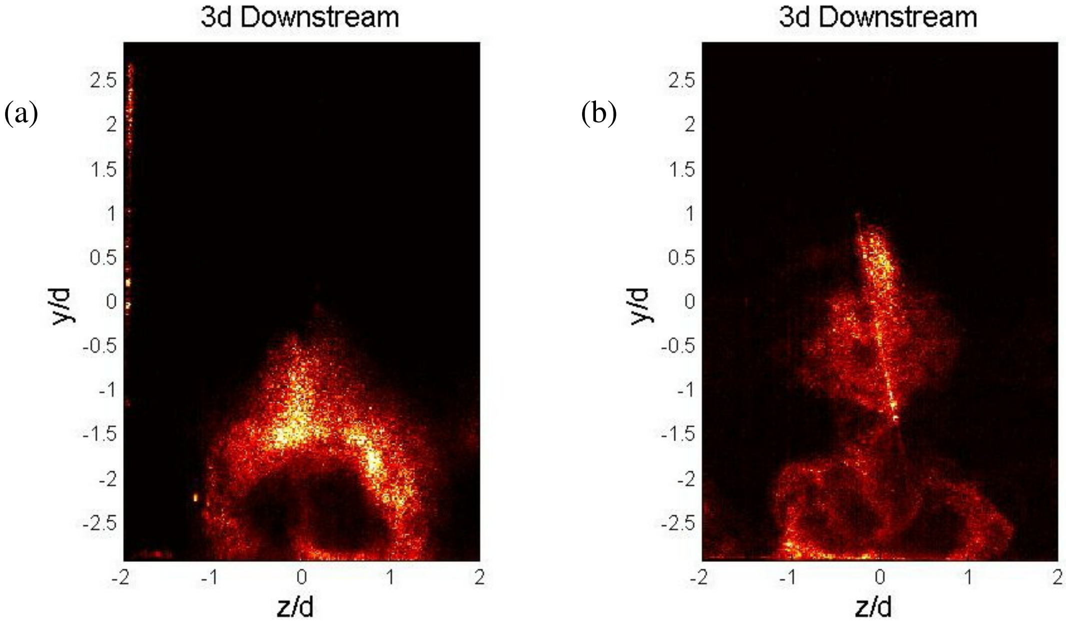

Figure 4.22: Instantaneous Mie-scattering images: (a) normal Injection, (b) parallel injection.

A large collection of instantaneous Mie-scattering images such as the ones shown in Figure 4.22 were gathered at 7 locations in the combustor. The locations spanned from the injection point, *x*=0*d*, to 3.81cm downstream of the injection point, or *x*=12*d*, for both injection schemes. The instantaneous images collected at each location for the normal injector and the parallel injector were then averaged and are shown in Figure 4.23 and Figure 4.24 respectively. The averaged images show the penetration of the fuel jet at the various locations, the lateral spreading and the flow structures of the fuel jet in the near field (0-3d) as well as the farfield (beyond 3d). The combustor height and width have been normalized with the injector diameter in the images. The bands at the top and bottom of the images are compensating for the changing aspect ratio of the combustor, and do not have physical meaning.

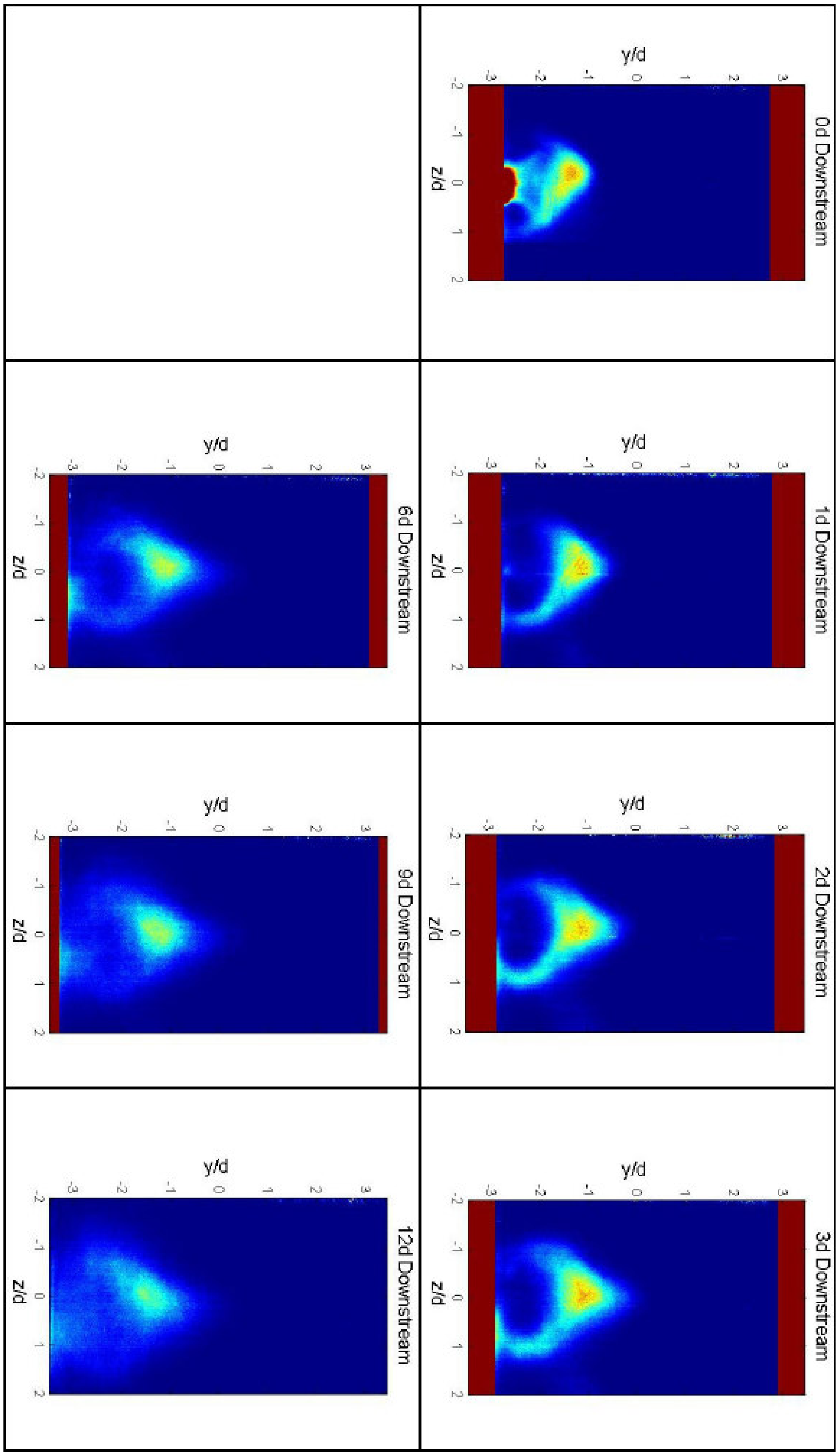

Figure 4.23: Time-averaged Mie-scattering images of normal injection test.

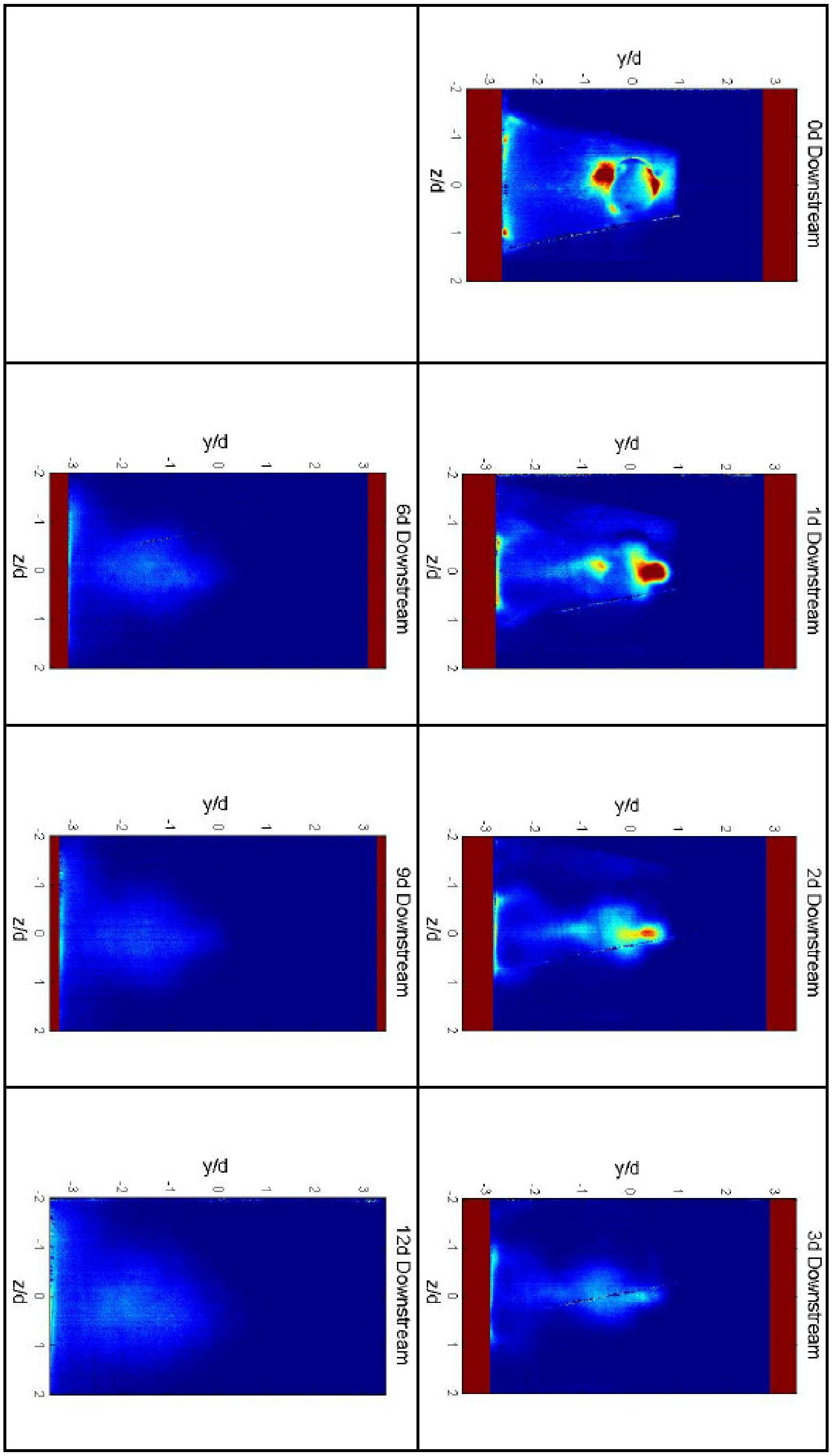

Figure 4.24: Time-averaged Mie-scattering images for ramped parallel injection tests.

Figure 4.23 shows the progression of the fuel mixing in the normal injection scheme. After injection the fuel penetrates to nearly the center of the combustor before it can no longer penetrate the flow. The fuel penetration seen in the Mie-scattering images follow exactly with the penetration seen in the time averaged Schlieren images. The fuel reaches a height slightly above the center of the combustor, and is no longer able to penetrate any further. A horseshoe vortex is formed below the main fuel jet and is visible in the near field however, beyond x=3d, the fuel begins to mix with the region below the main jet. The fuel also continues to spread laterally in the combustor, at x=12d the fuel has spread nearly to the walls of the combustor.

Figure 4.24 shows the fuel mixing as it progresses through the parallel injection combustor. The images in the near field are hard to interpret because of the combination of product formation seeding and scalar transport seeding, however it is obvious that as the fuel exits the injector it begins to lose penetration height, as shown in the Schlieren images. The fuel jet leaving the injector does not penetrate any further into the combustor. The main fuel jet is accompanied by some fuel that is trapped in the wake caused by the injection ramp at the very bottom of the combustor. In the farfield the fuel is a significantly lower height than when first injected. There fuel has spread laterally at the bottom of the combustor however spreading is minimal near the center jet. The fuel has mixed with a region of combustor significant to that of the normal injection scheme, however if we examine the rate of mixing the parallel injector performs much worse than the normal injector. The penetration achieved by the ramp is negated in the farfield, and the fuel is only able to mix with the combustor air trapped in the wake of the ramp. The poor lateral mixing and lack of any penetration beyond the injection point is expected since the mixing is achieved only through the shear layers between the fuel and combustor air. By using Matlab to process the Mie-scattering images the cross-sectional area of the combustor occupied by fuel was determined and is plotted as a percentage of the total cross-sectional area versus the axial location, *x/d*, in Figure 4.25. The parallel injection provides a greater area coverage initially, however the area reduces to match that of the normal injection. The reflection of the ramp in the first three images adds some error to the plots, however the general trend is still valid.

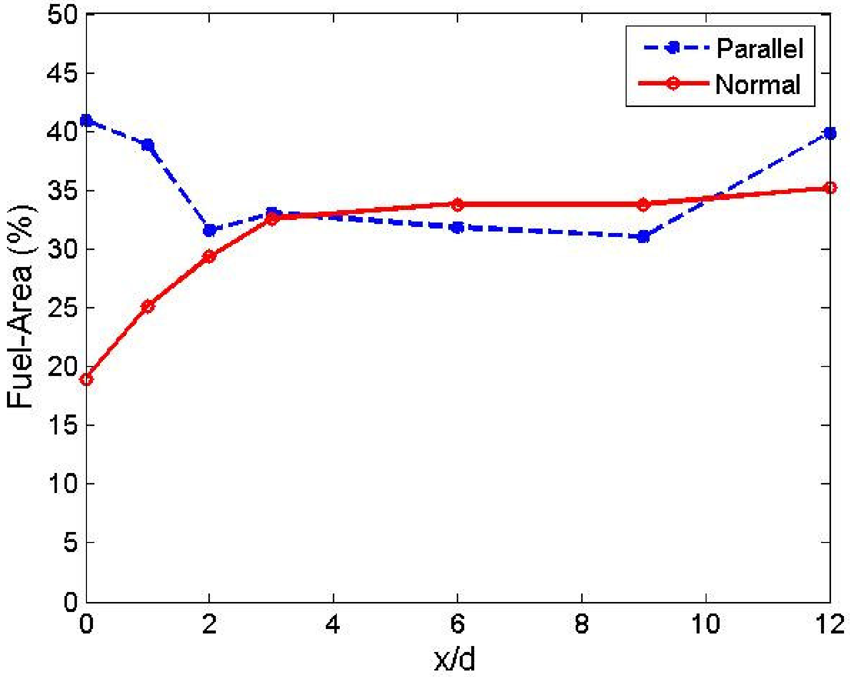

Figure 4.25: Fuel-area versus axial location with $\dot{m}_{\text{fuel}}$ = 1.98x10^{-3} kg/s.

4.3 Fin-Guided Studies

4.3.1 Results

4.3.1.1 Pressure Losses

Pressure traces for the test conditions described in were acquired using the Scanivalve DSA described earlier. Figure 4.26 and Figure 4.27 provide a summary of the tests conducted for the 45° and 90° Fin-Guided injection schemes respectively. The *x*-axis has been normalized with the injection orifice diameter, *d*, and the value *x/d*=0 is the location of the injector in the combustor. The *x/d*=0 location also coincides with the start of a second 3.5° expansion along the top and bottom walls as shown in the diagrams above the pressure traces.

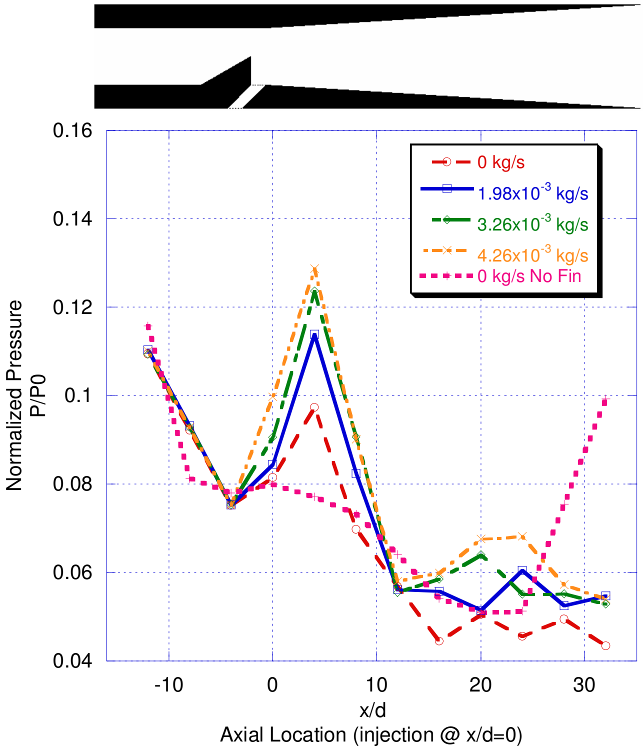

Figure 4.26: Normalized wall pressure distribution for all 45° Fin-Guided tests.

All of the 45° Fin-Guided injection pressure traces shown in Figure 4.26 are initially decreasing; this is due to the flow accelerating in the expansion zone upstream of the fin and injection point. The increase in the static pressure downstream of the fin is caused by the oblique shock induced by the fin and injected fuel column impinging on the crossflow. The oblique shock is visualized in the Schlieren images in the following section. The Fin-Guided zero fuel massflow condition, plotted in the dashed red line, shows the pressure rise associated with the fin when compared to the no fin, zero fuel condition. Comparing the zero fuel pressure trace with the pressure traces of the conditions in which fuel is injected, the pressure rise associated with the fuel injection column can be examined. As a greater massflow of fuel is injected into the crossflow a greater pressure rise occurs. The increase in pressure for these cases is a direct result of the increased flow blockage created by the fuel column. The pressure trace further downstream of the injection the pressure begins to decrease again, this is because of the supersonic expansion which continues until boundary layer separation effects begin to set in at x/d = 15 and the static pressure begins to rise.

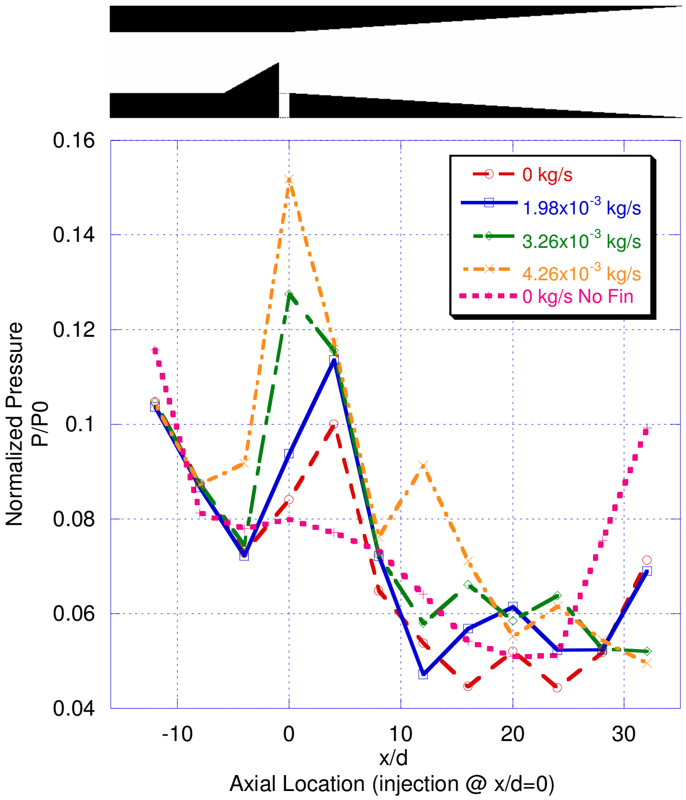

Figure 4.27: Normalized wall pressure distributions for all 90° Fin-Guided tests.

Similar trends are noticed with the pressure traces for 90° Fin-Guided injection, as shown in Figure 4.27. As fuel massflow is increased the pressure rise becomes greater as seen with the 45° injection; however the increase is much more dramatic. The 90° injection increases the fuel columns ability to penetrate the crossflow, creating more blockage and a greater pressure rise. Downstream of the pressure spike incurred from the fin and the blockage from the fuel column the pressure decreases again, however it is noted that the onset of boundary layer separation effects occurs earlier than for the 45° injection cases; *x/d* = 8 versus *x/d*=15 for the 45° cases. The added axial momentum from the 45° fuel injection is able to keep the boundary layer from separating longer than the 90° injection case where there is no added axial momentum from the fuel injection. It is also noticed that the pressure traces at both injection angles are very similar for fuel massflow at 0 kg/s and 1.98x10^{-3} kg/s, however fuel massflow above this cause the pressure rise in the 90° injection to propagate upstream. Similar pressure traces are expected for the zero fuel cases since the geometry of the two combustors is nearly identical, but it is not as intuitive for the case when fuel is being injected. Figure 4.28 and Figure 4.29, which compare the two fin-aided injection schemes along with the normal injection without a fin scheme for fuel massflow of 1.98x10^{-3} kg/s and 4.26x10^{-3} kg/s respectively are used for closer examination.

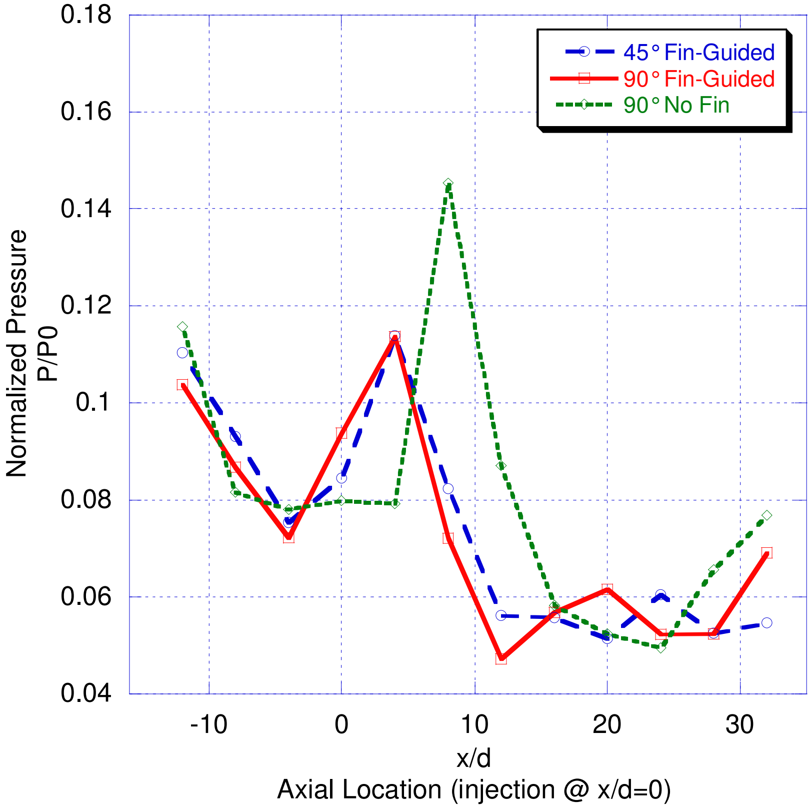

Figure 4.28: Wall pressure distributions for all Fin-Guided and normal injection schemes with $\dot{m}_{\text{fuel}}$ = 1.98x10^{-3} kg/s.

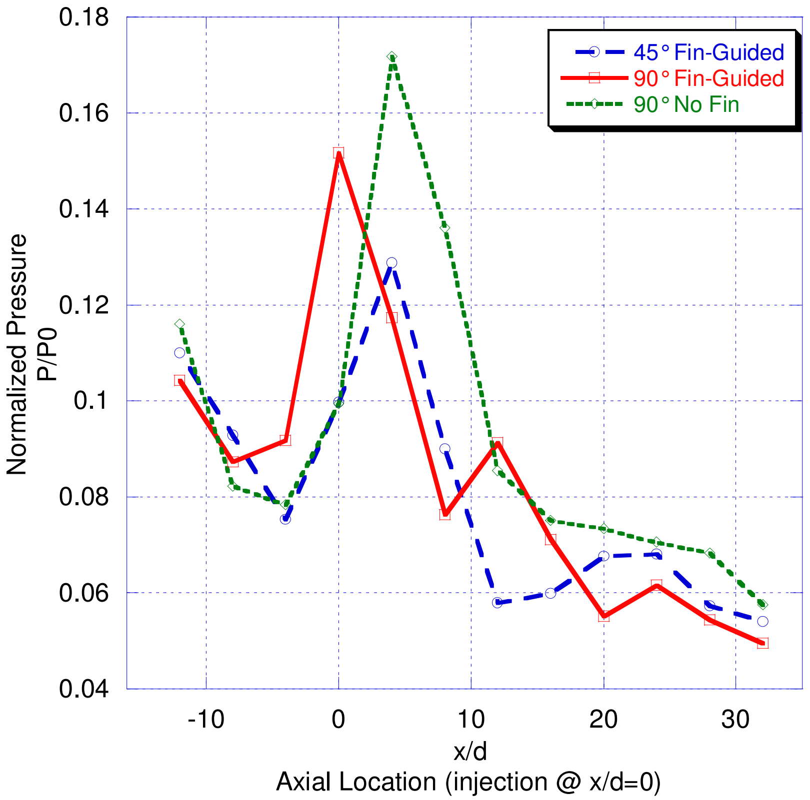

Figure 4.29: Wall pressure distributions for all Fin-Guided and normal injection schemes with $\dot{m}_{\text{fuel}}$ = 4.26x10^{-3} kg/s.

In Figure 4.28 the pressure trace for the 45° injection falls nearly on top of the 90° pressure trace, while in Figure 4.29 the pressure spike for the 90° injection case is much greater than that of the 45° injection. In both cases the normal injection without a fin has the highest pressure rise incurring the greatest flow losses. The oblique shock off of the fin is able to reduce the strength of the single bow shock forming from the normal fuel column for the 90° injection schemes. The pressure rise is reduced by 28% as seen in Figure 4.28 and by 13~33% with the higher fuel massflow rate shown in Figure 4.29. It is also noted that there is significant pressure information prorogating upstream of the injection point in the 90° Fin-Guided case, meaning that the fuel column penetrating the crossflow must be interacting the boundary layer on the top surface of the combustor. The fuel column generated by a massflow of $1.98\text{x}10^{-3}$ kg/s must penetrate to similar heights in with both injection angles since the pressure incurred is equal. The injection angle for fuel massflow of $4.26\text{x}10^{-3}$ kg/s has a significant role in the penetration height, as 90° injection provides greater penetration. There is also a secondary pressure rise occurring in the 90° injection case, this could be caused by the fuel column interacting with the boundary layer. Using instantaneous Schlieren images the driving mechanisms behind the pressure traces will be determined.

4.3.1.2 Schlieren

In order to better understand what is happening in the combustor and to visualize the flow structures, instantaneous and time-averaged Schlieren images were collected. Figure 4.30 and Figure 4.31 depict the instantaneous Schlieren images taken for each of the test conditions run using the 45° Fin-Guided tests and 90° Fin-Guided tests respectively.

The flow structures for the condition without fuel injection are the same for both 45° and 90° injection systems, which is expected since the geometries are the same. Reflected compression waves formed at the first geometry change are seen upstream of the fin, as is an incident compression wave coming off of the fin, which is then reflected. Downstream of the fin, where the top and bottom combustor walls begin to expand at 3.5°, expansion waves can be seen. These structures still form in the cases with fuel injection; however they interact with the fuel column to create new structures as well. In the images with fuel injection it is obvious the normal, 90°, injection scheme penetrates further than the 45° injection case, as expected since the fuel has a greater *y*-momentum flux.

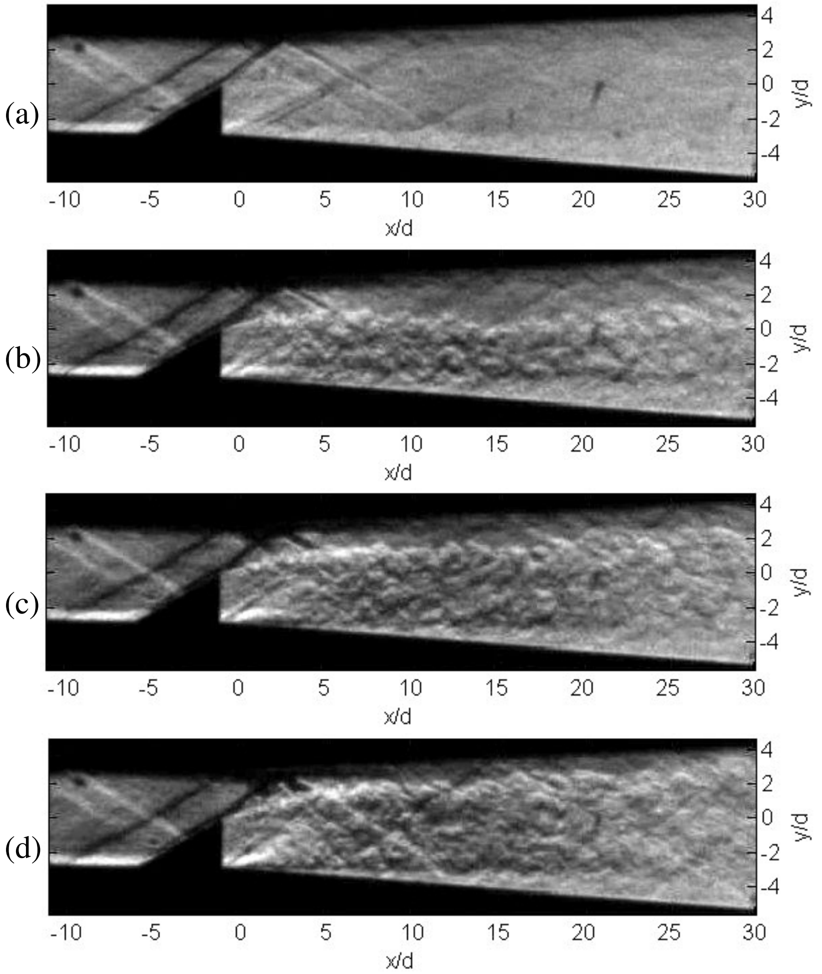

Figure 4.30: 45° Fin-Guided instantaneous Schlieren images: (a) no fuel, (b) $\dot{m}_{\text{fuel}}$ = 1.98x10^{-3} kg/s, (c) $\dot{m}_{\text{fuel}}$ = 3.26x10^{-3} kg/s, (d) $\dot{m}_{\text{fuel}}$ = 4.26x10^{-3} kg/s.

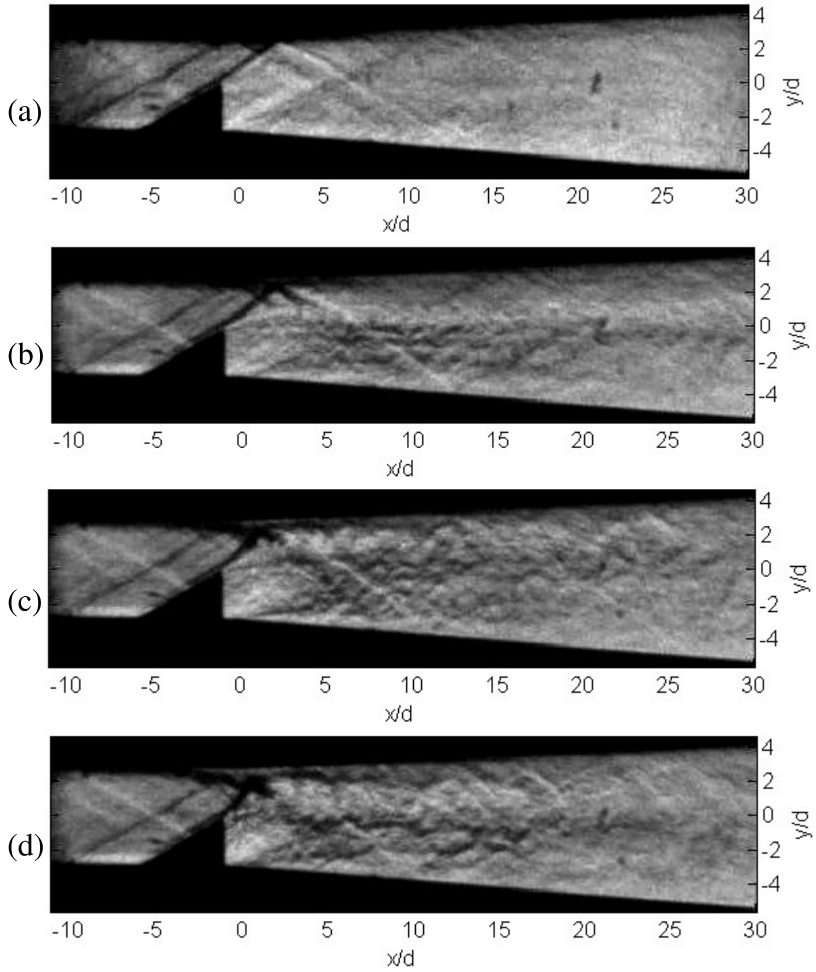

Figure 4.31: 90° Fin-Guided instantaneous Schlieren images. (a) no fuel, (b) $\dot{m}_{\text{fuel}}$ = 1.98x10^{-3} kg/s, (c) $\dot{m}_{\text{fuel}}$ = 3.26x10^{-3} kg/s, (d) $\dot{m}_{\text{fuel}}$ = 4.26x10^{-3} kg/s.

For the condition (b), in Figure 4.30 and Figure 4.31, with fuel massflow at 1.98x10^{-3} kg/s there is not a significant difference in the fuel penetration, which explains the near equal pressure rise for both injection schemes. However, with fuel massflow at 3.26x10^{-3} kg/s and 4.26x10^{-3} kg/s, we notice that while both designs achieve greater penetration height, the 90° injection penetrates deep enough to begin interacting with the boundary layer on the top surface of the combustor. The interaction between the compression shock off of the fin, the fuel column and boundary layer is easily visualized in test condition (d), fuel massflow at 4.26x10^{-3} kg/s, with the 90° injector. The interaction between these three elements is the cause for the large pressure rise upstream of the injector as information is being propagated through the subsonic boundary layer. It also appears as thought the boundary layer separates where the fuel column impinges before reattaching, causing the secondary pressure rise noted in the pressure traces.

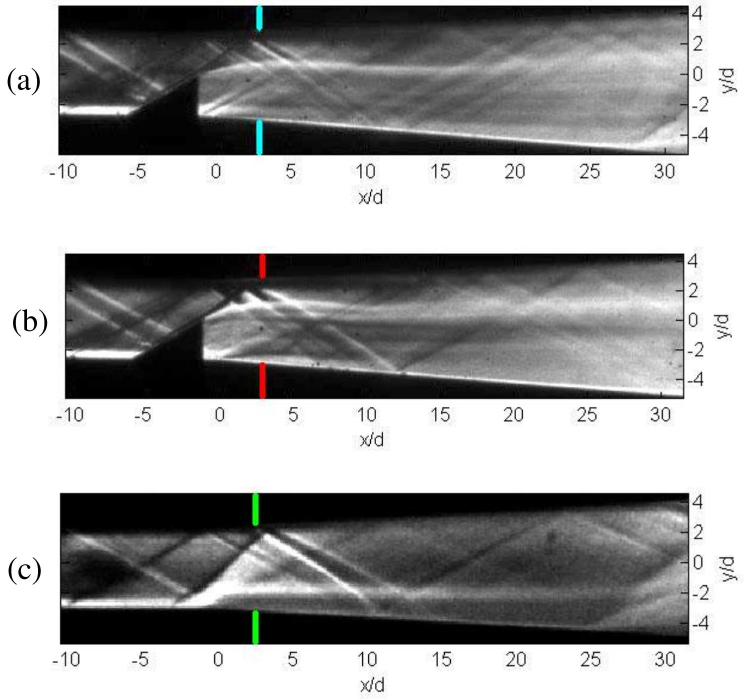

Figure 4.32: Time-averaged Schlieren images, $\dot{m}_{\text{fuel}}$ = 1.98x10^{-3} kg/s. (a) 45° Fin-Guided injection, (b) 90° Fin-Guided injection, (c) normal injection without fin.

Figure 4.32 depicts time-averaged Schlieren images for both Fin-Guided injection schemes with fuel massflow at 1.98x10^{-3} kg/s as well as normal injection without a fin. The averaged Schlieren images will be used to examine the fuel penetration characteristics for the injection schemes. The Schlieren images show Fin-

Guided 90° injection is able to achieve the greatest penetration height, while normal injection without a fin shows the poorest performance. Figure 4.33 verifies the greater penetration with Fin-Guided 90° injection by using Matlab to calculate the image intensity. The color bands in Figure 4.32 represent the *x*/*d*=3 location used in Figure 4.33.

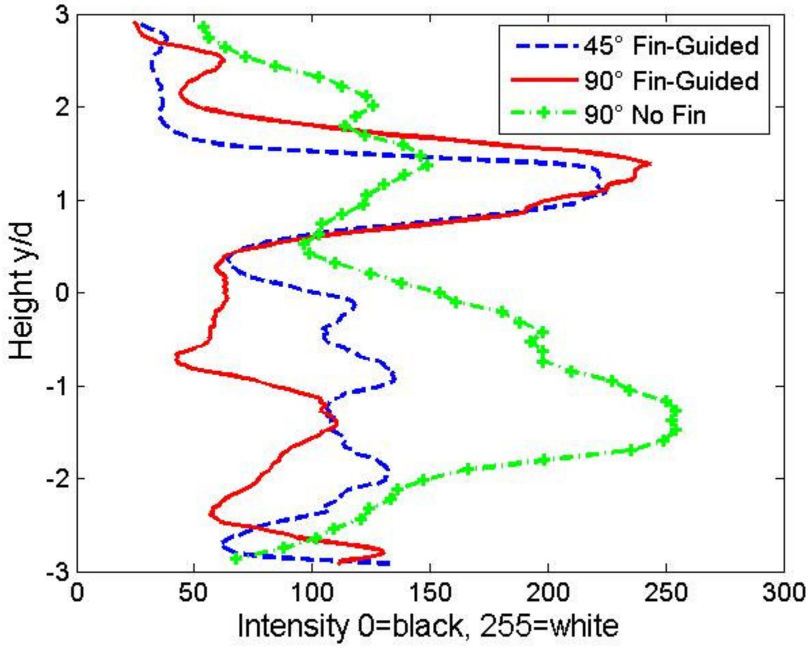

Figure 4.33: Intensity profile of time-averaged Schlieren images at *x*/*d*=3 for Fin-Guided and normal injection schemes.

Using the technique used to generate Figure 4.33, Figure 4.34 shows the fuel penetration height throughout the first 12 orifice diameters downstream of the injector. The black bands in Figure 4.34 represent the combustor walls. It is clear that the Fin-Guided injection schemes penetrate the crossflow significantly greater than the normal injection alone. A penetration increase of 100% is achieved with 45° injection and 120% with 90° injection with the fin. The 90° Fin-Guided injection achieves the greatest initial fuel penetration however the additional fuel penetration for both Fin-Guided injection methods is nearly the same. The slope and trend of the two Fin-Guided fuel injection angles are nearly identical. Meaning that though the 90° injection is able to penetrate into the crossflow deeper than the 45° injection, it does relate to an increase in penetration rate further along in the combustor. All injection schemes achieve the most penetration near the injection point, but then slowly level off.

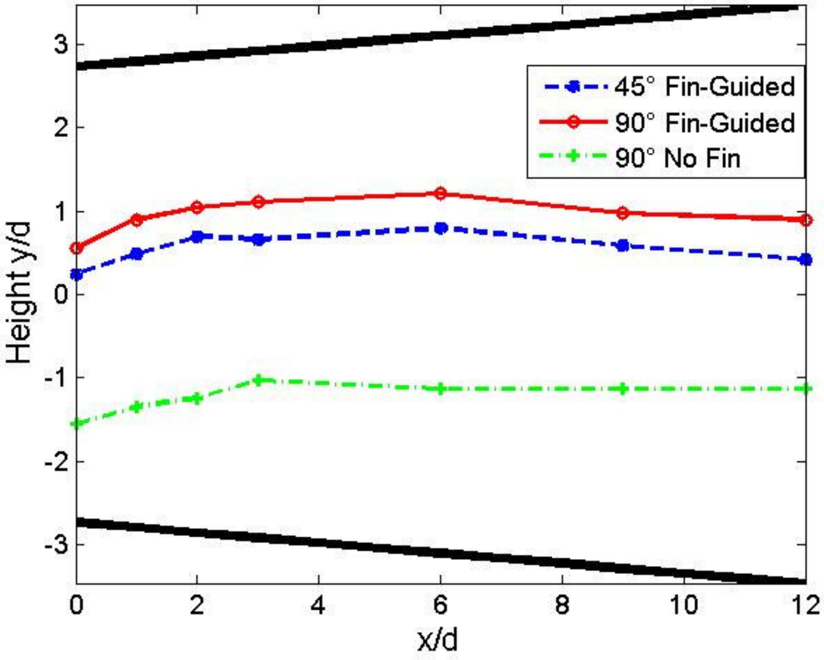

Figure 4.34: Fuel penetration versus axial location for Fin-Guided and normal injection schemes with $\dot{m}_{\text{fuel}} = 1.98\text{x}10^{-3}$ kg/s.

4.3.1.3 Mie-scattering

The technique used to gather Mie-scattering images did not allow testing the exact conditions run for the Schlieren images and the pressure traces, since the massflow of smoke injected into the combustor could not be controlled. Instead of injecting helium at 1.98×10^{-3} kg/s, air seeded with fog was injected using suction. The resulting momentum flux of the air was 4.54×10^{5} N/m^2, making the momentum flux ratio, J, 1.1 for 90° injection and J=0.78 for 45° injection. However, the images obtained are used to provide insight into the rate of spreading achieved for both injection angles and to validate trends found examining the Schlieren images and pressure traces, which are independent of fuel massflow. The pulse of the Solo Nd:Yag laser used in the Mie-scattering images is 3-5 ns full width half maxim, sufficient enough to freeze the flow field for instantaneous images. Figure 4.35 shows instantaneous Mie-scattering images taken at three downstream locations for both of the Fin-Guided injector types.

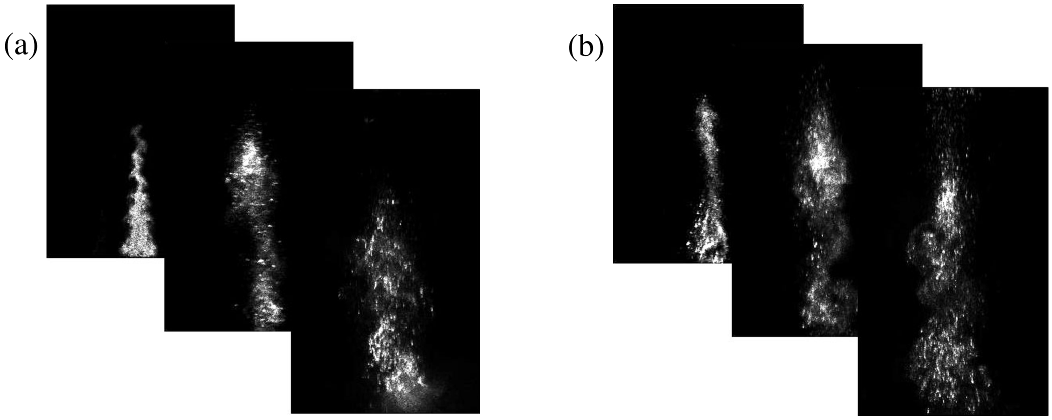

Figure 4.35: Instantaneous Mie-scattering images (a) 45° Fin-Guided, (b) 90° Fin-Guided.

The first image in each sequence was taken at *x/d*=0 followed by images at *x/d*=6 and *x/d*=12. The images show the cross-sectional area the fuel spreads to at various locations in the combustor. Similar images have been collected at 7 locations downstream of the combustor, ranging between *x/d*=0 and *x/d*=12.

Time-averaged Mie-scattering images are shown in Figure 4.36 and Figure 4.37 for the 45° and 90° Fin-Guided schemes respectively. The averaged images were obtained by taking the mean of fifty instantaneous Mie-scattering images. The averaged images show the penetration of the fuel jet at the various locations, the lateral spreading and the flow structures of the fuel jet in the near-field (0-3*d*) as well as the far-field (beyond 3*d*). The combustor height and width have been normalized with the injector diameter in the images. The color scheme has been altered for easier visualization. The bands at the top and bottom of the images are compensating for the changing aspect ratio of the combustor, and do not have physical meaning.

While the exact fuel massflow is not the same as used for the Schlieren tests, the Mie-scattering images validate the trends discovered earlier with the 45° Fin-Guided injection. The fuel penetration height increases until about *x/d*=3 before it levels off. The fuel is concentrated at the bottom of the fuel column. In the near-field images there is a strong concentration of fuel which moves from the center of the column to the top, this is the fuel which is continuing to travel at 45° after the injection. There is very little lateral spreading, most of which occurs in the wake of the fin. The initial fuel plume at *x/d*=0 is in almost the exact same shape of the fin, which then transforms into a column until finally taking on the shape seen in the *x/d*=9 and *x/d*=12 images.

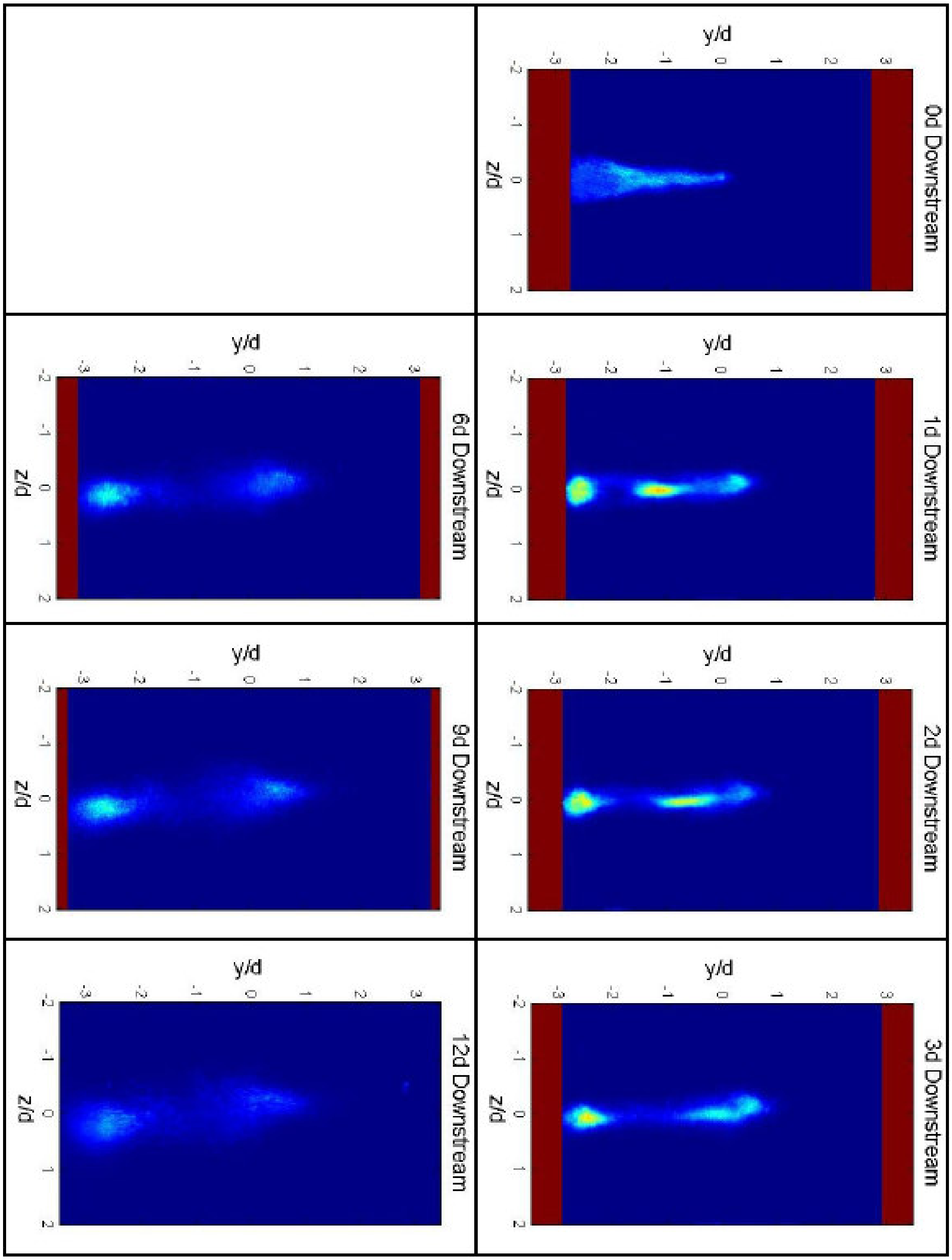

Figure 4.36: Time-averaged Mie-scattering images for 45° Fin-Guided tests.

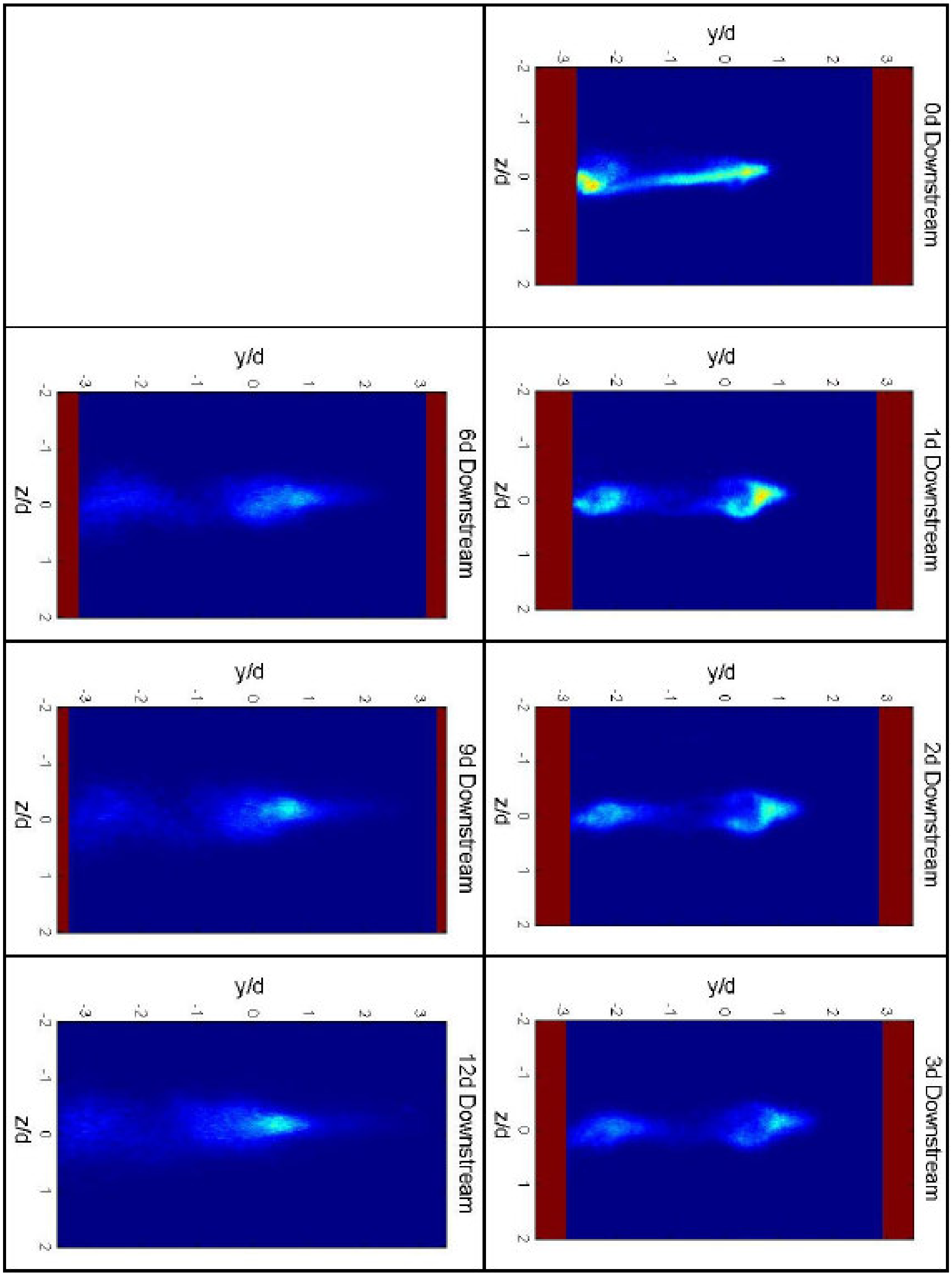

Figure 4.37: Time-averaged Mie-scattering images for 90° Fin-Guided tests.

The same trend found in the average Schlieren images is also found examining Figure 4.37 for the Mie-scattering image for 90° injection; the penetration height increases up to *x/d*=6 before leveling off and coming down a little. As with the Schlieren tests we can see that the fuel has achieved significantly greater penetration when injected at 90° versus 45°. It is also noticed that the highest areas of fuel concentration are at the bottom of the fin and the very top of the fuel column. However, the fuel is lifted away from the bottom combustor wall further in the 90° injection and disperses quicker than with the 45° injection method, which avoids flashback in combustion and overheating the combustor wall. There also appear to be horseshoe vortices forming at the crest of fuel column and the base in the near-field. As with the 45° injection the initial shape of the fuel plume at *x/d*=0 takes on the shape of fin. There is very little lateral spreading in the near-field, where the plume takes on the shape of a column, it is not until the fuel is 6 diameters downstream of the injector that there is any real lateral spreading. The lateral spreading that does occur is, like the 45° cases, limited to the wake of the fin.

By using Matlab to process the Mie-scattering images the cross-sectional area of the combustor occupied by fuel was determined and is plotted as a percentage of the total cross-sectional area versus the axial location, *x/d*, in Figure 4.38. Injection at 90° provides for a greater initial fuel area than 45° injection, however much like the penetration height, Figure 4.34, additional fuel spreading downstream of the fin is the same as with the 45° injection. The spreading occurs at nearly the exact same rate and follows the same trend. The average rate of spreading for both injection methods are nearly identical. The 90° injection scheme had a rate of growth of approximately

1.6% per orifice diameter, while injection at 45° had a rate of growth of 1.7% per orifice diameter. The additional spreading of the fuel is achieved primarily as a mechanism of the wake caused by the fin, since the fin used is the same for both injection angles, the rate of spreading is the same.

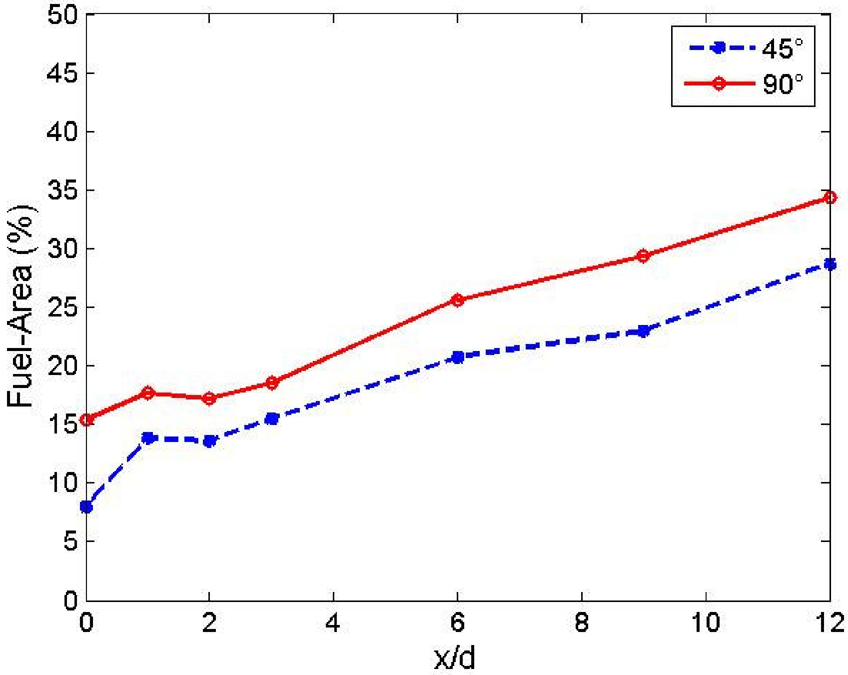

Figure 4.38: Fuel-area versus axial location for Fin-Guided tests.

5 Summary and Concluding Remarks

5.1 Supersonic Combustor Characterization

A characterization of a three dimensional supersonic combustor was performed for a range of core equivalence ratios utilizing a fuel rich pilot flame for ignition and flame holding. Through wall pressure measurements it was found that optimum combustor performance came from a core equivalence ratio of 0.25. The reason for this was theorized to be that the pilot flame and fuel injection only influenced about 25-30% of the combustor cross-sectional area. Ultimately this leads to a local equivalence ratio near unity. The theory is supported by high-speed images of the flame, chemiluminescence data, and analysis of jet penetration from empirical data. Furthermore, C_2* and CH* chemiluminescence intensity data supported this finding, as the peak and average intensity occurred in the neighborhood of Φ = 0.2~0.25. The performance of the combustor suffered because of the weak fuel-air penetration that was achieved. If the fuel was able to penetrate into a larger area of the combustor, performance would have increased. However, if normal injection was used to penetrate fuel throughout the entire combustor crossflow the pressure losses would have been very significant, decreasing the total efficiency of the engine. Therefore in order to enhance the combustor performance new injection schemes must be investigated. This work will serve as a baseline for future comparison with injector design and novel combustor geometry.

5.2 Fuel Injection Studies

5.2.1 Baseline Fuel Injection Schemes

A nonreacting study comparing normal and parallel injection has been conducted in a supersonic combustor using choked injection of helium into supersonic air stream. Mixing effectiveness was assessed from both Schlieren images of the combustor side view showing the extent of the simulated fuel penetration and planar Mie-scattering images of the cross-sectional view showing the fuel dispersion. Also, wall pressure along the combustor top wall was measured to evaluate the flow loss caused by the injection schemes.

In both injection schemes, the static pressure was raised significantly above the isentropic value suggesting substantial momentum loss. While the pressure rise in the normal injection case was directly related to the fuel momentum flux thus indicating relevance to mixing, the ramped parallel injection incurred a much higher pressure rise, which was independent of the fuel momentum flux. This suggests that the ramp geometry in parallel injection should be optimized to minimize the static pressure rise or the momentum loss. The maximum pressure rise associated with normal injection was only 31-38% of the ramped parallel injection case, depending on fuel momentum flux.

Schlieren images of normal injection revealed that the fuel penetration depth was increased with the fuel momentum flux as expected. Increased fuel penetration caused more blockage of the incoming airflow which would result in greater shock strength causing static pressure rise downstream. The flow field associated with the ramped parallel injection, however, was mostly independent of the fuel momentum flux, suggesting the extent of mixing was confined within the wake of the ramp. The parallel mixing was dominated by the injector ramp and the flow images did not show much variation between different fuel momentum cases. Figure 5.1 illustrates the trade offs between pressure rise and penetration height for both injection schemes.

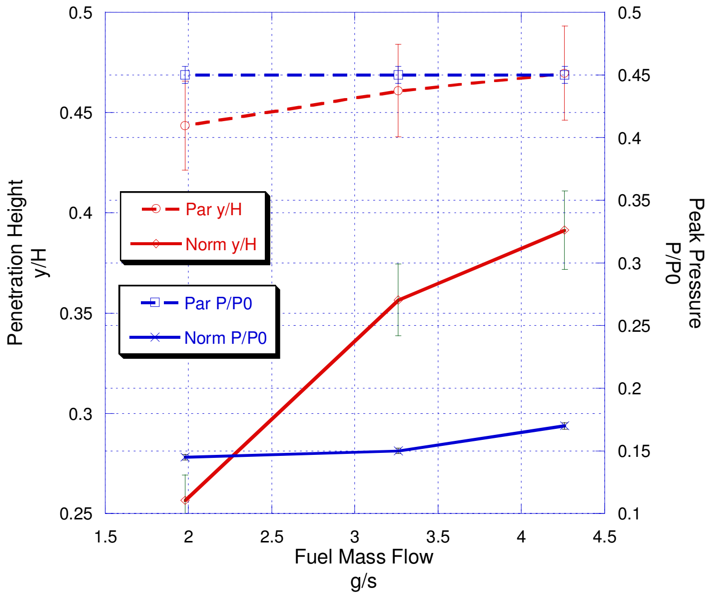

Figure 5.1: Penetration height and pressure rise trade off for normal and parallel injection.

The planar Mie-scattering images combined with Schlieren images showed that the ramped parallel injector and the associated wake dispersed fuel more rapidly in the near-field. However, as the fuel traveled downstream in the combustor, the rate of mixing appeared less in the parallel injector case than in the normal injection case. While the penetration of the normal injector is not as large initially as the parallel injector, the fuel is able to reach about the same penetration in about 10-20 injector diameters downstream.

5.2.2 Fin-Guided Cases

A nonreacting study comparing Fin-Guided 45° and 90° fuel injection has been conducted in a supersonic combustor using choked injection of helium into supersonic air stream. Mixing effectiveness was assessed from both Schlieren images of the combustor side view showing the extent of the simulated fuel penetration and planar Mie-scattering images of the cross-sectional view showing the fuel dispersion. Also, wall pressure along the combustor top wall was measured to evaluate the flow loss caused by the injection schemes.

In both injection schemes, the static pressure was raised above the isentropic value suggesting momentum loss. The pressure rise for Fin-Guided cases was similar for low fuel massflow, where penetration heights were similar and the majority of the pressure rise was associated with the fin. At greater massflow, above 3.26×10^{-3} kg/s, the pressure rise in 90° Fin-Guided fuel injection is significantly greater than its 45° injection counterpart, because the penetration height is also greater. The fuel column penetrates to the boundary layer on the top combustor wall, causing a large pressure rise, as well as sending pressure rises upstream, this should be avoided. Both Fin-Guided fuel injection schemes suffered significantly lower flow losses then normal fuel injection without a fin. The oblique shock from the fin is able to reduce the strength of the normal shock forming due to the fuel column by 13-33% depending on massflow and fuel injection angle.

Schlieren images revealed that the fuel penetration depth was increased with the fuel momentum flux as expected. Increased fuel penetration caused more blockage of the incoming airflow which would result in greater shock strength causing static pressure rise downstream. Fin-Guided fuel injection achieved over 100% greater fuel penetration than normal injection without a fin. The 90° Fin-Guided fuel injection achieved greater penetration than 45° Fin-Guided injection, but did not experience a greater rate of penetration. The 45° injection was able to reach the top of combustor at higher massflow, with lower flow losses and pressure rise. The difference in penetration height is experience at the injection port.

The planar Mie-scattering images combined with Schlieren images showed that the penetration height and fuel-area trends are very similar for both Fin-Guided injection angles. The difference in penetration height and fuel area does not grow or shrink as you move downstream of the injector. The difference between injection angle performances is realized at the injection point. Both Fin-Guided injection angles demonstrate exceptional penetration, but poor lateral spreading which takes place predominantly in the wake of fin. It is possible that using a fin slightly wider than the injection orifice will increase the amount of lateral spreading. The Fin-Guided 90° injection is better at lifting fuel away from bottom wall; avoiding flashback during combustion and over heating combustor walls.

While both Fin-Guided injection schemes outperformed normal injection without a fin by achieving greater penetration heights, as well as lower flow losses, there exists trade offs between injection at 45° and 90°. The 90° injection is able to penetrate at greater depths and allows for slightly greater fuel-area spreading. While the 45° injection achieves slightly lower penetration heights with lower pressure rises and flow loss. The 45° injection has the added advantage of being able to add axial momentum to the combustor creating partial thrust. Fin-Guided fuel injection performance could be further increased if the injection angle behind the fin is optimized. The fin can be used to place fuel at any desired location within the combustor, and when utilized with many other fins can be used to introduce fuel throughout an entire combustor area.

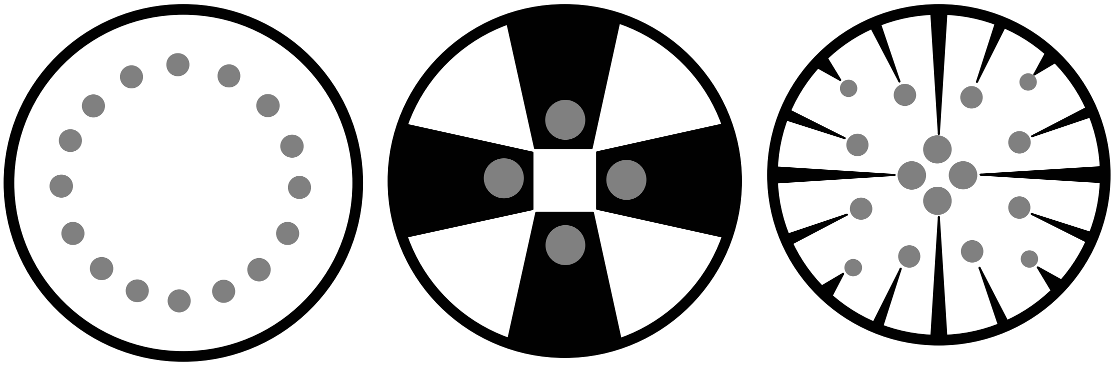

Figure 5.2: Fuel injection concepts (left to right) wall injection, ramped parallel injection, Fin-Guided injection.

Figure 5.2 shows fuel distributions of three possible fuel injection techniques, the combustor and injector geometry is shown in black, while fuel columns are shown in grey. The left shows wall jet injection, the penetration depth of the fuel is not very significant, any further fuel injection will come at high flow losses as shown in this study. The second injection scheme is using ramped parallel injection. While the fuel is now injected to the center of the combustor, it comes at a very large flow blockage, which translates to large flow losses. The third injection scheme is the Fin-Guided wall injection. An array of different sized fins is used to inject fuel at multiple locations within the combustor, evenly distributing the fuel for efficient combustion. It is this authors belief that such an array can be used to solve the mixing problem in inward turning combustors and usher in the age of routine hypersonic airbreathing flight.

5.3 Contribution

The significant contributions of these experimental studies are:

- The characterization of a supersonic combustor with an aspect ratio of one was conducted. The results of the characterization can be used as a baseline for future combustor characterizations using novel geometries or fuel injection schemes. The performance data has already been used to motivate investigations into fuel injection enhancements.
- The investigation and comparison of normal and parallel injection system has been studied in a supersonic flow. The study provided insight into future design considerations for injection schemes to be employed in low aspect ratio supersonic combustors for which penetration is critical. The data collected was used to determine the positive contributions to mixing enhancement of each scheme. These positive characteristics have since been used to create a novel fuel injection scheme, Fin-Guided injection.
- The development and study of a novel fuel injection scheme has been established. Fin-Guided fuel injection has been introduced as a possible solution to the mixing problems associated with low aspect ratio combustors, as found in inward turning vehicle concepts. Fin-Guided injection has been shown to efficiently and effectively mix fuel into a low

aspect ratio supersonic combustor. The Fin-Guided injection has been shown to reduce flow losses by 13-30% while increasing fuel penetration by 100-120%. This scheme can be used to inject fuel with pinpoint accuracy to any location within a combustor and significantly enhance mixing and combustion while reducing flow losses.

5.4 Future Work

The work presented provides many new avenues for which future work can continue. The author suggests the following:

- Fin-Guided injection has been shown to not only improve fuel penetration, but also reduce flow losses associated with injection without pylons. Angling the fuel injection downstream of the fin has been shown to have similar results as the transverse injection downstream of the fin, but also adds fuel momentum to the creation of thrust. Optimization of the fin size and injection angle should be conducted to determine what configuration works best.
- It is the hope of this author that Fin-Guided injection be implemented as an array. With multiple fins, of varying size be used to injection fuel uniformly within a combustor. The flow interaction between multiple fins in close proximity and fuel injection must be investigated before Fin-Guided injection scheme can be confidently employed in a supersonic combustor.
- Once cold flow studies have been conducted to optimize fin size and injection angle, and the flowfield and aerodynamic effects of utilizing multiple Fin-

Guided injectors has been investigated, the performance a Fin-Guided injection scheme should be studied in reacting combustor tests. The final design application for Fin-Guided injection should be to improve the combustion efficiency in scramjets. In order to validate this scheme, reacting tests must be investigated in which arrays of Fin-Guiding injectors are employed to evenly distribute fuel.

6 Appendices

6.1 Appendix A: Supersonic Combustion Rig

Figure 6.1 through Figure 6.5 are the detailed CAD schematics for supersonic combustion rig designed by Zang.[31]

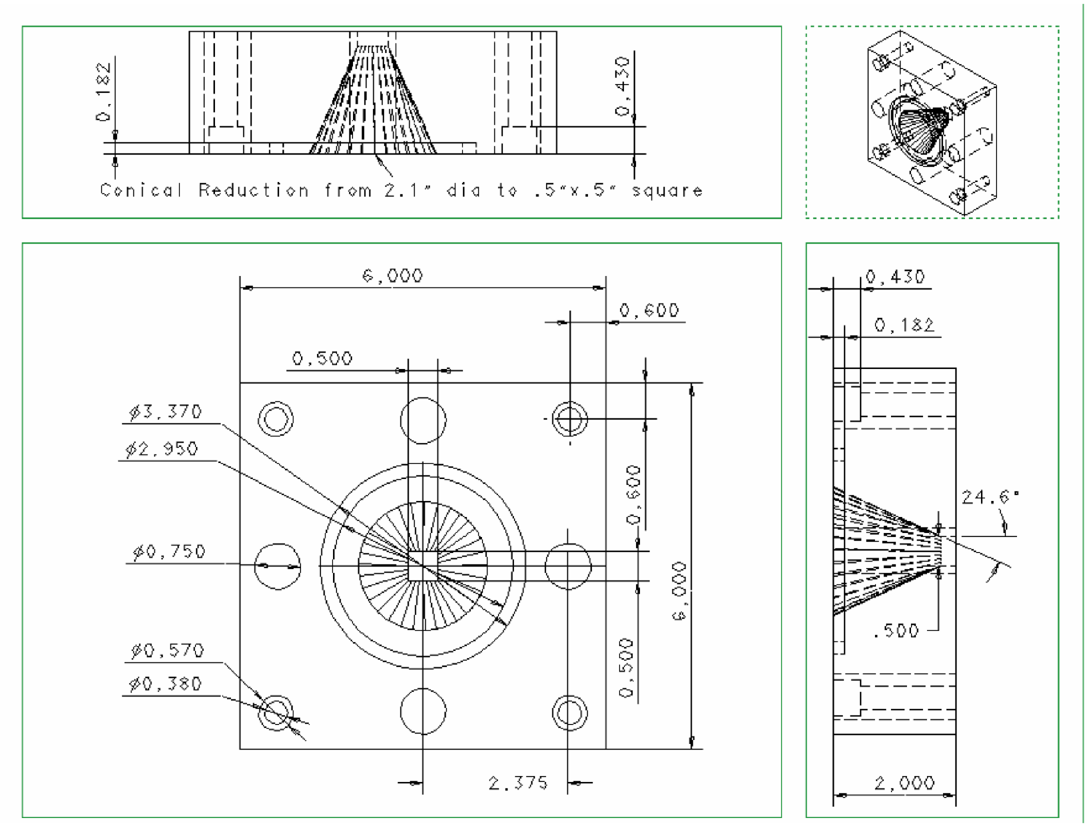

Figure 6.1: Transition block schematic for supersonic combustion rig.

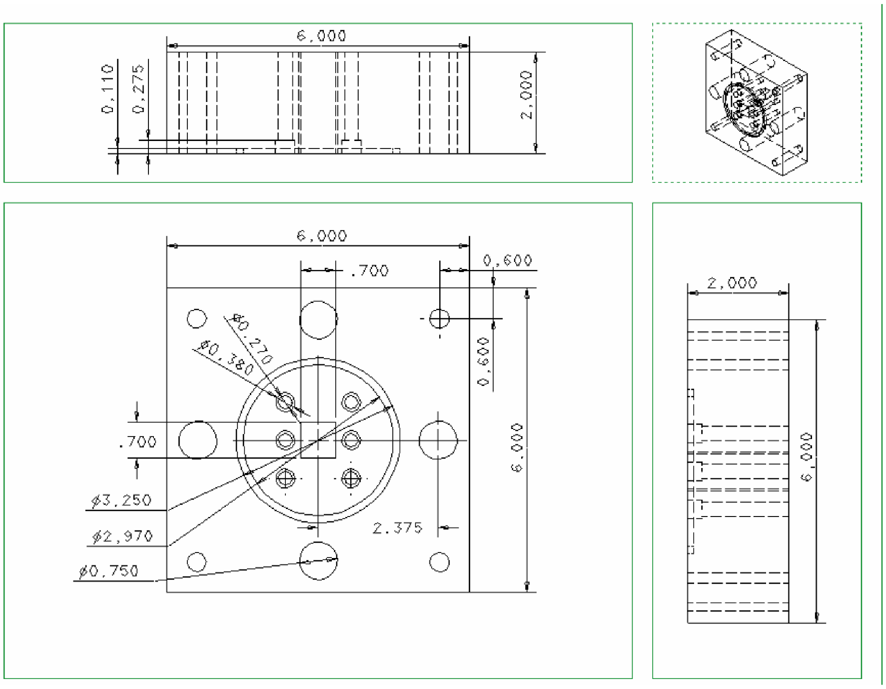

Figure 6.2: Front block schematic for supersonic combustion rig.

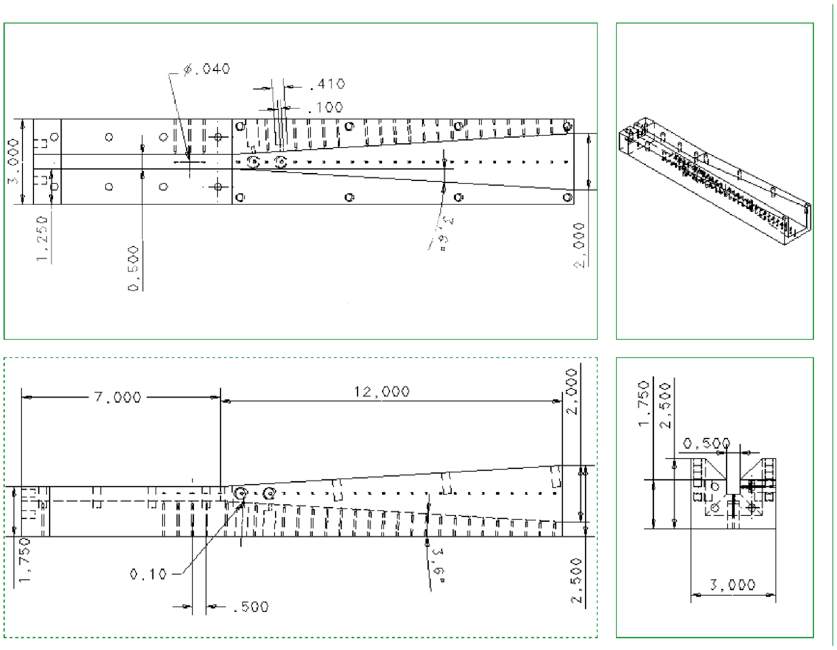

Figure 6.3: Combustion block schematic for supersonic combustion rig.

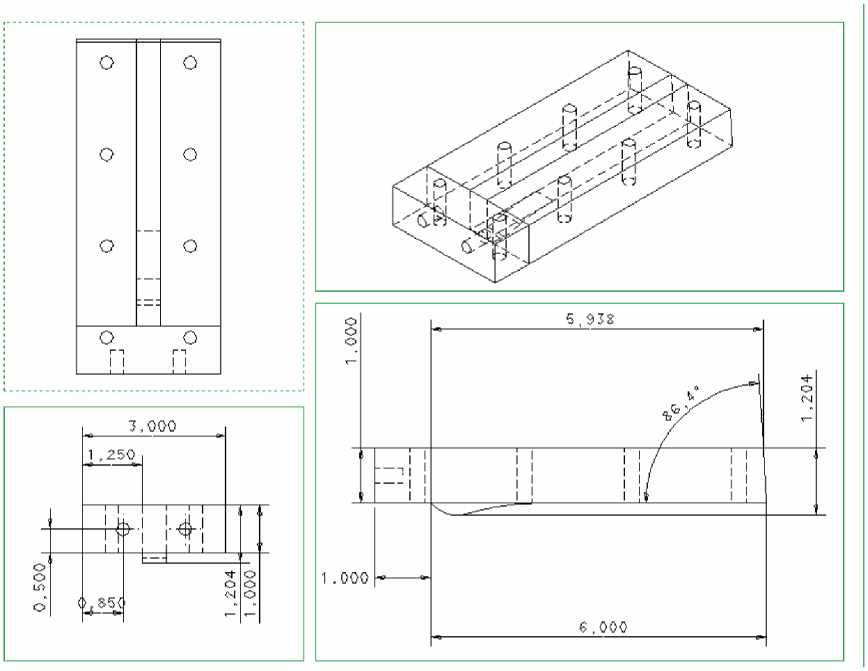

Figure 6.4: Nozzle plate schematic for supersonic combustion rig.

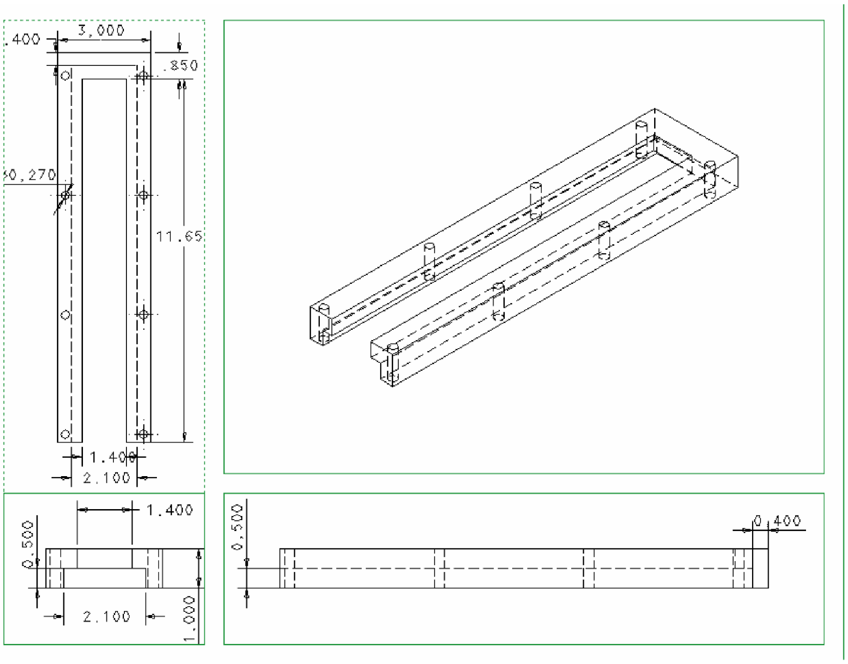

Figure 6.5: Window holder schematic for supersonic combustion rig.

6.2 Appendix B: Fuel Injection Enhancement Rig

Figure 6.6 through Figure 6.13 are the detailed CAD schematics for the different components of the fuel injection enhancement rig.

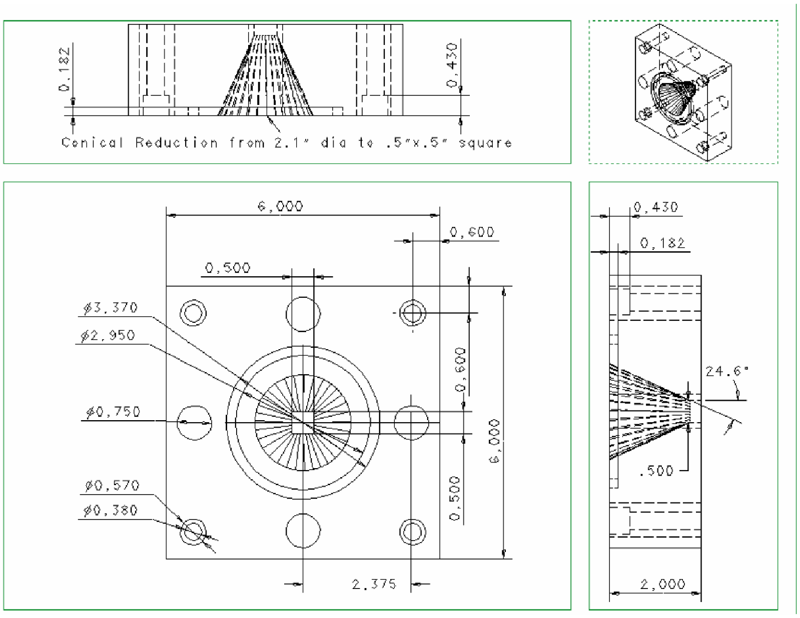

Figure 6.6: Transition block for fuel injection enhancement rig.

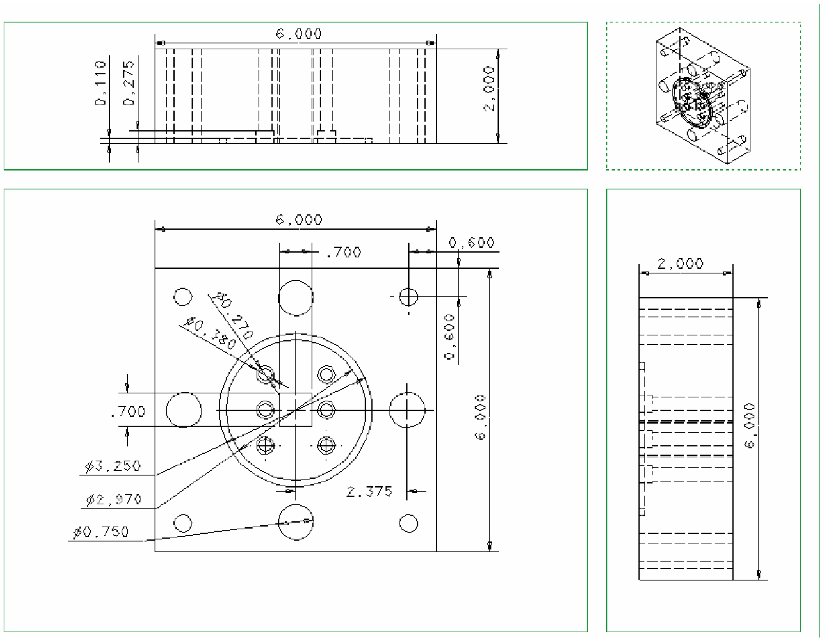

Figure 6.7: Front block for fuel injection enhancement rig.

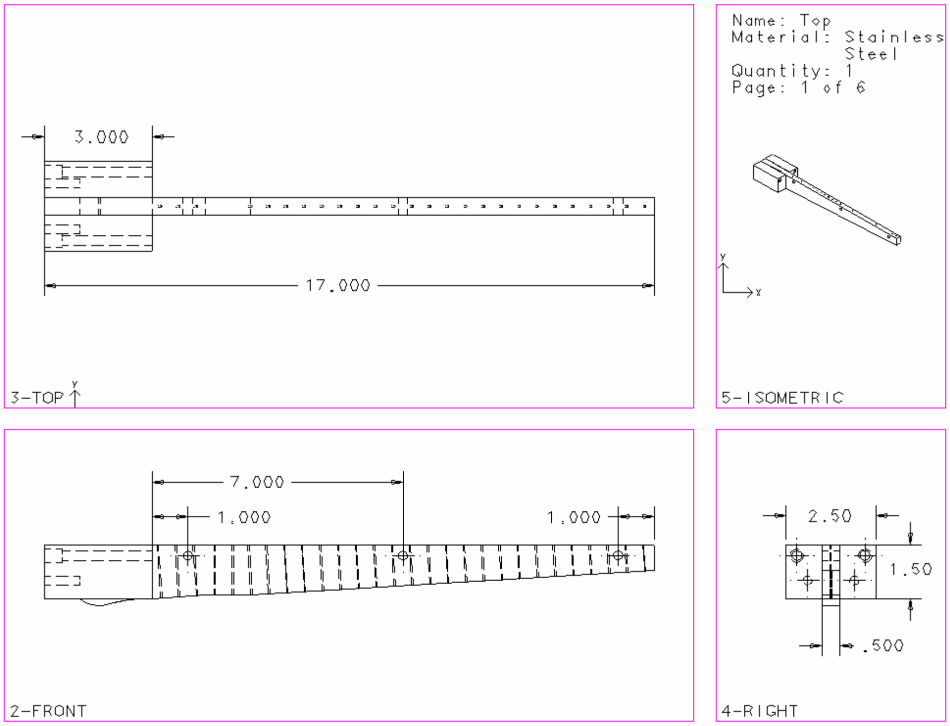

Figure 6.8: Top plate/nozzle plate for fuel injection enhancement rig.

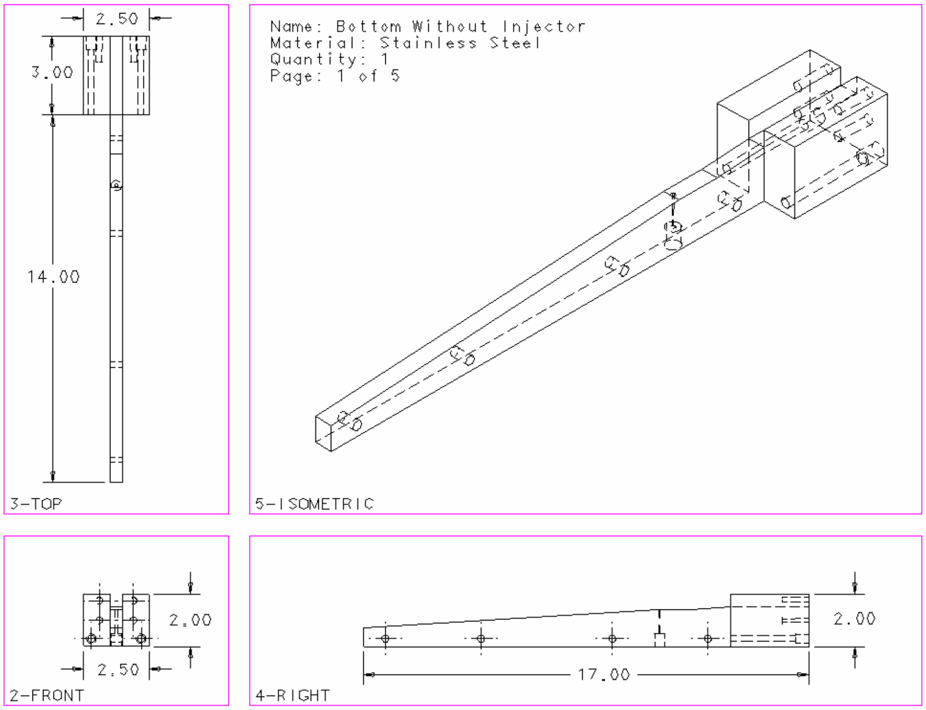

Figure 6.9: Transverse bottom plate schematic for fuel injection enhancement rig.

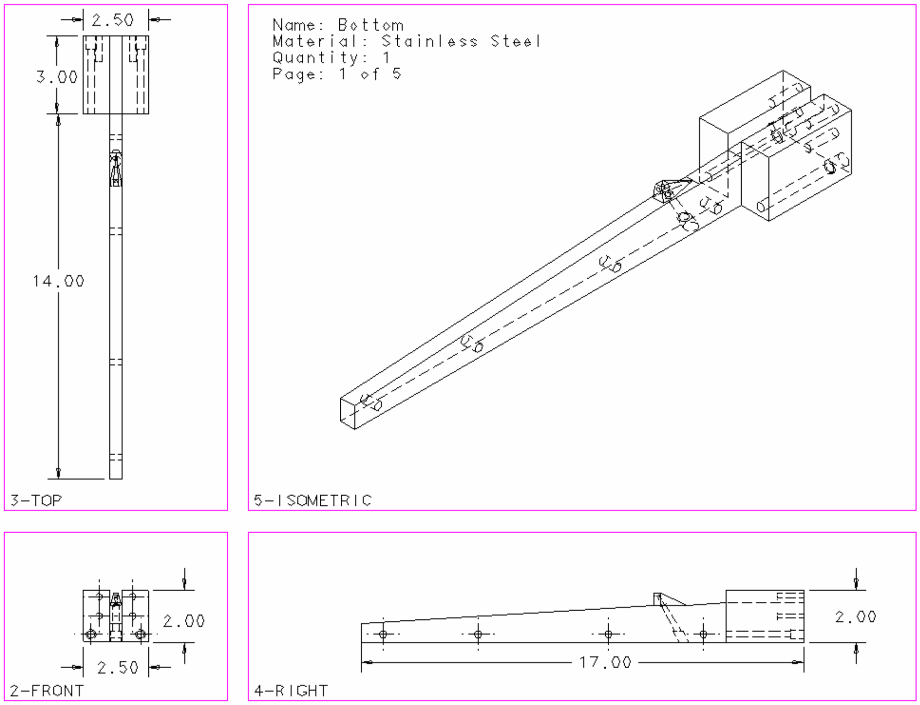

Figure 6.10: Ramped parallel bottom plate schematic for fuel injection enhancement rig.

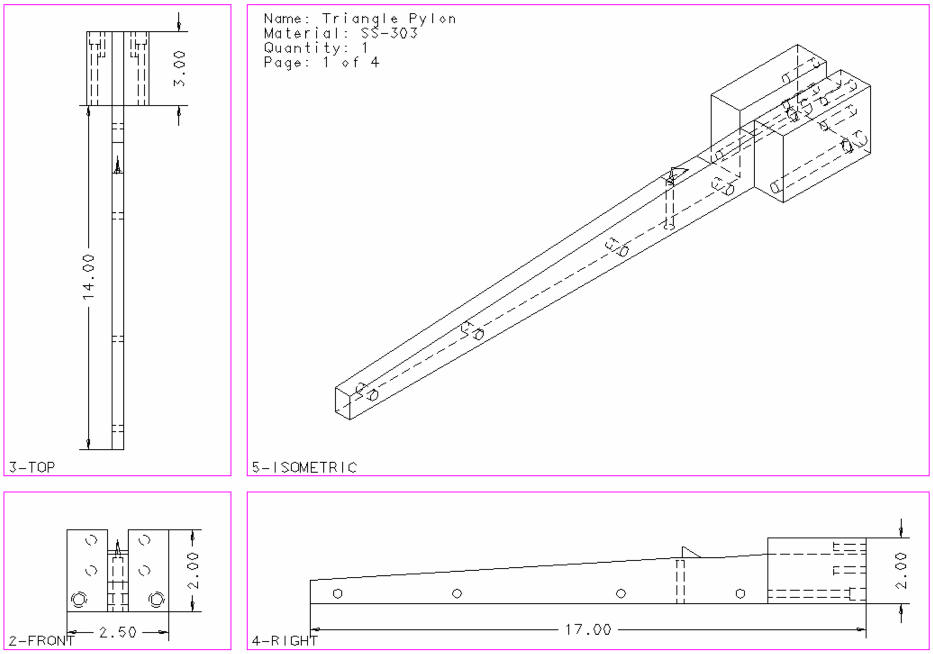

Figure 6.11: 90° Fin-Guided bottom plate schematic for fuel injection enhancement rig.

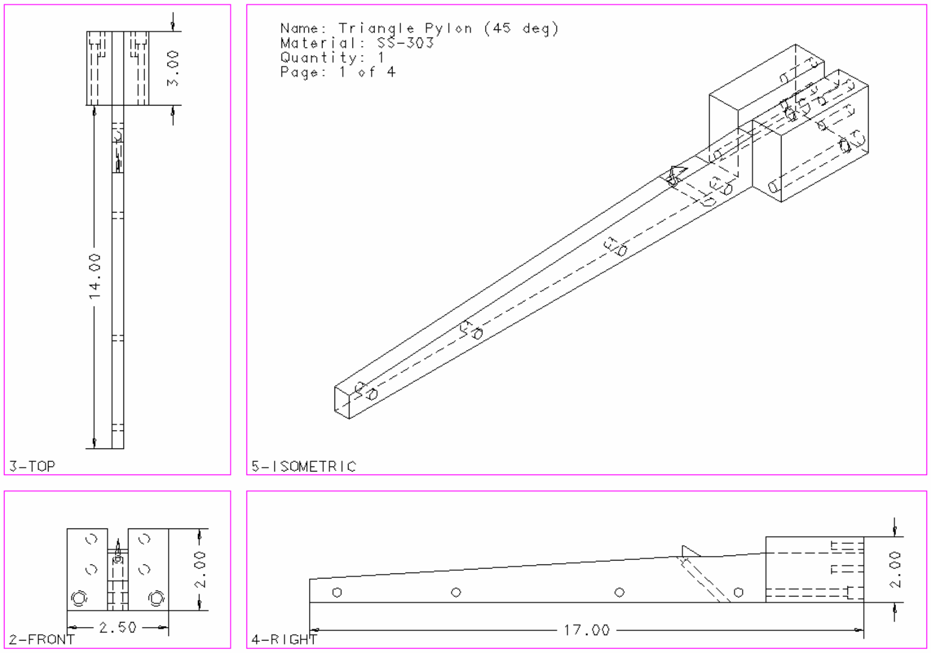

Figure 6.12: 45° Fin-Guided bottom plate schematic for fuel injection enhancement rig.

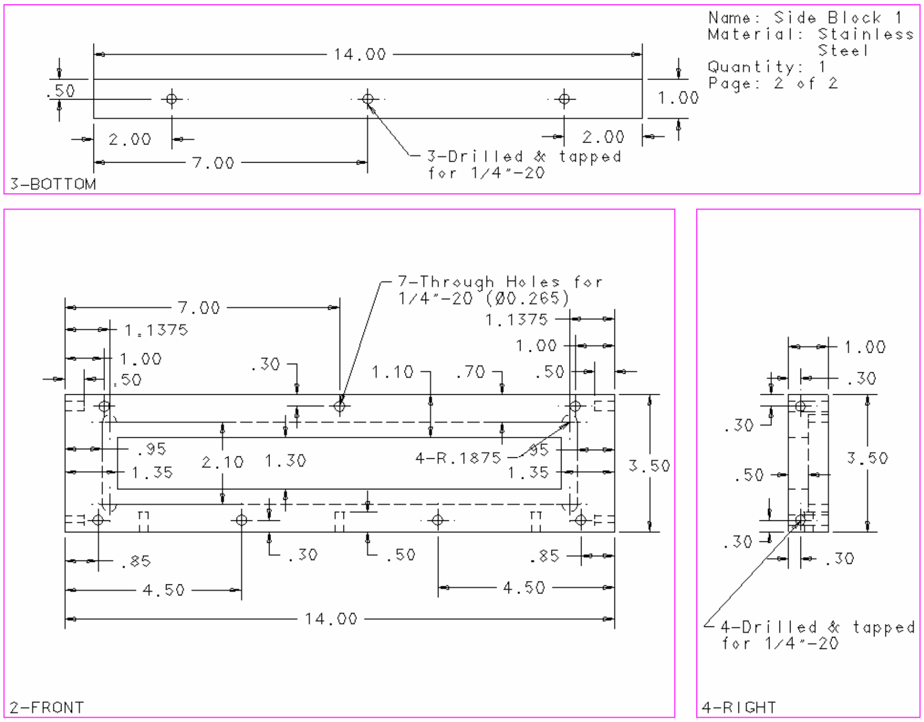

Figure 6.13: Window holder schematic for fuel injection enhancement rig.

7 BIBLIOGRAPHY

1. McClinton, C. R., “X-43-Scramjet Power Breaks the Hypersonic Barrier,” 44th AIAA Aerospace Sciences Meeting and Exhibit, AIAA 2006-1, January 2006.
2. Bilardo, V.J.; Hunt, J.L.; Lovell, N.T.; Maggio, G.; Wilhite, A.W.; and McKinney, L.E.: The Benefits of Hypersonic Airbreathing Launch Systems for Access to Space. AIAA 2003-5265. July 2003, Huntsville, AL.
3. Curran, E.T., “Scramjet Engines: The First Forty Years,” Journal of Propulsion and Power, Vol. 17, No.6, Nov-Dec 2001, pp. 1138-1148.
4. Dugger, G.L., “Recent Advances in Ramjet Combustion,” ARS Journal, Vol. 29, No. 11, 1959, pp. 819-827.
5. Weber, R.J., “A Survey of Hypersonic-Ramjet Concepts,” American Rocket Society, Paper 875-59, 1959.
6. Roy, M.M., “Moteurs Thermiques,” Comtes Rendus de l’ Academie des Sciences, Vol. 222, No.1, 1946; see also Royal Aircraft and Establishment Library Translation 112, 1946.
7. Ferri, A., “Discussion on M. Roy’s Paper Propulsion Supersonique par Turboreacteurs et par Statoreacteurs,” Advances in Aeronautical Sciences, Vol. 1, Pergamon, Oxford, England, U.K., 1959, pp. 79-112.
8. Ferri, A., Libby, P.A., and Zakkay V., “Theoretical and Experimental Investigations of Supersonic Combustion,” Proceedings of the International Council of the Aeronautical Sciences, Third Congress, Stockholm, 1962. Spartan, New York, 1964, pp. 1089-1155.

9. Curran, E.T., “Scramjet Engines: The First Forty Years,” Journal of Propulsion and Power, Vol. 17, No.6, Nov-Dec 2001, pp. 1138-1148.
10. Weber, R.J., and MacKay, J.S., “An Analysis of Ramjet Engines using Supersonic Combustion,” NACA TN 4386, Sept. 1958.
11. Dugger, G. L., “Comparison of Hypersonic Ramjet Engines with Subsonic and Supersonic Combustion,” High Mach Number Airbreathing Engines, Pergamon, Oxford, England, U.K., 1961, pp. 84–110.
12. Billig, F. S., “Overview of Propulsion Performance,” AGARD Conf. on Future Aerospace Technology in the Service of the Alliance, Vol. 3: Sustained Hypersonic Flight Paper C33, April 1997.
13. Billig, F.S., “SCRAM – A Supersonic Combustion Ramjet Missile,” at 29th AIAA/SAE/ASME/ASEE Joint Propulsion Conference, AIAA 93-2329, June 1993.
14. Billig, F.S., and Kothari, A.P., “Streamline Tracing: Technique for Designing Hypersonic Vehicles,” Journal of Propulsion and Power, Vol. 16, No. 3, May-June 2000. pp 465-471.
15. Molder, S., and Szpiro, E., “Busemann Inlet for Hypersonic Speeds,” Journal of Spacecraft and Rockets, Vol. 3, No. 8, 1966, pp. 1303-1304.
16. Hunt, J., and Rausch, V., “Airbreathing Hypersonic Systems Focus at NASA Langley Research Center,” 8th AIAA International Space Planes and Hypersonic Systems and Technologies Conference, Norfolk, VA, Apr. 27-30, 1998, AIAA 1998-1641.
17. Molder, S., “Internal, Axisymmetric, Conical Flow,” AIAA Journal, Vol. 5, No.

7, 1967, pp. 1252-1255.

18. Molder, S., and D'Souza, N., "Applicability of Hypersonic Small-Disturbance Theory and Similitude to Internal Hypersonic Conical Flows," Journal of Spacecraft and Rockets, Vol. 7., No. 2, 1970, pp. 149-154.
19. Lewis, M., "A Hypersonic Propulsion Airframe Integration Overview (Invited)," 39th AIAA/ASME/SAE/ASEE Joint Propulsion Conference and Exhibit, Huntsville, Alabama, July 20-23, 2003, AIAA 2003-4405.
20. Billig, F., Jacobsen, L., "Comparison of Planar and Axisymmetric Flowpaths for Hydrogen Fueled Space Access Vehicles," 39th AIAA/ASME/SAE/ASEE Joint Propulsion Conference and Exhibit, Huntsville, Alabama, July 20-23, 2003, AIAA 2003-4407.
21. Kothari, A. P., Tarpley, C., McLaughlin, T., Babu, S., and Livingston, J.W., "Hypersonic Vehicle Design Using Inward Turning Flow Fields," ASME, SAE, and ASEE, Joint Propulsion Conference and Exhibit, 32nd, Lake Buena Vista, FL, July 1-3, 1996, AIAA 1996-2552.
22. Billig, F., Baurle, R., Tam, C., and Wornom, S., "Design and Analysis of Streamline Traced Hypersonic Inlets," AIAA International Space Planes and Hypersonic Systems and Technologies Conference, 9th, Norfolk, VA, Nov. 1-5, 1999, AIAA 1999-4974.
23. Lewis, M., Boyd, I., Cockrell, C., "Aerodynamics for Optimal Engine-Integrated Airbreathing Launcher Configurations," 40th AIAA/ASME/SAE/ASEE Joint Propulsion Conference and Exhibit, Fort Lauderdale, Florida, July 11-14, 2004, AIAA 2004-3983.

24. Van Griethuysen, V.J., Glickstein, M.R., Petley, D.H., Gladden, H.J., and Kubik, D.L., "High-Speed Flight Thermal Management," Developments in High-Speed-Vehicle Propulsion Systems, Edited by Murthy, S.N.B, and Curran, E.T., Progress in Astronautics and Aeronautics Series, Vol. 165, 1996, pp. 517-579
25. Kothari, A. P., Tarpley, C., Raghavan, V., and Livingston, J., "Comparison of Inward and 2D HTHL/VTHL and SSTO/TSTO Vehicles for Access-to-Space and Impact of Unit Structural Weight Growth," 51st JANNAF Propulsion Meeting, Lake Buena Vista, FL, 2002.
26. Dissel, A., Kothari, A. P., Raghavan, V., Lewis, M., "Comparison of HTHL and VTHL Airbreathing and Rocket Systems for Access to Space," 40th AIAA/ASME/SAE/ASEE Joint Propulsion Conference and Exhibit, Fort Lauderdale, Florida, July 11-14, 2004. AIAA-2004-3988.
27. Tarpley, C., Kothari, A. P., Raghavan, V., and Petley, D., "Engine Off-Design Performance Results Using SRGULL for and Inward-Turning RBCC SSTO Vehicle," 1998 JANNAF Propulsion Meeting, Cleveland, OH, 1998.
28. Tarpley, C., and Kothari, A. P., "Effect of Trimmed Flight on Inward-Turning SSTO RLV GTOW." 12th AIAA International Space Planes and Hypersonic Systems and Technologies Conference, Norfolk, VA, Dec. 15-19, 2003, AIAA 2003-6995.
29. Cutler, A.D., Diskin, G.S., Danehy, P.M., Drummond, J.P., "Fundamental Mixing and Combustion Experiments for Propelled Hypersonic Flight," 38th AIAA/ASME/SAE/ASEE Joint Propulsion Conference and Exhibit, AIAA 2002-3879, July 2002.

30. Cutler, A.D., Danehy, P.M., O'Byrne, S., Rodriguez, C.G., Drummond, J.P. "Supersonic Combustion Experiments for CFD Model Development and Validation (Invited)" at 42nd Aerospace Sciences Meeting and Exhibit, AIAA 2004-266, January 2004.
31. Zang, A.H., Fuel Injection in Scramjets: Mixing Enhancement and Combustion Characterization Experiments, M.S. thesis, Univ. of Maryland, College Park, MD, 2005.
32. Seiner, J.M., Dash, S.M., and Kenzakowski, D.C., "Historical Survey on Enhanced Mixing in Scramjet Engines," Journal of Propulsion and Power, Vol. 17, No. 6, 2001, pp. 1273-1286.
33. E.T. Curran, S.N.B Murthy, "Scramjet Propulsion"; Progress in Astronautics and Aeronautics, V. 189, 2001.
34. I.W. Kay, W.T. Peschke, R.N. Guile, "Hydrocarbon-Fueled Scramjet Combustor Investigation," Journal or Propulsion and Power, Vol. 8, No.2, 1992, pp. 507-512.
35. M.B. Colket, L.J. Spadaccini, "Scramjet Fuels Autoignition Study," Journal of Propulsion and Power, Vol. 17, No.2, 2001, pp. 315-323.
36. Tishkoff, J.M., Drummond, J.P., and Edwards, T., "Future Directions of Supersonic Combustion Research: Air Force/NASA Workshop on Supersonic Combustion," 35th Aerospace Sciences Meeting & Exhibit, AIAA 1997-1017, January 1997.
37. Ferri, A., "Review of Problems in Application of Supersonic Combustion," Journal of the Royal Aeronautical Society, Vol. 68, No. 645, 1964, pp. 575-595.
38. Cain, T., and Walton, C., "Review of Experiments on Ignition and Flameholding

in Supersonic Flow," 38th AIAA/ASME/SAE/ASEE Joint Propulsion Conference & Exhibit, AIAA 2002-3877. July 2002.

39. Weidner, E.H., and Drummond, J.P., "Numerical Study of Staged Fuel Injection for Supersonic Combustion," AIAA Journal, AIAA 1981-1468R, Vol. 20, No. 10, pp. 1426-1431.
40. Fuller, R.P., Wu, P.-K., Nejad, A.S., Schetz, J.A., "Fuel-Vortex Interactions for Enhanced Mixing in Supersonic Flow," AIAA/ASME/SAE/ASEE 32nd Joint Propulsion Conference and Exhibit, AIAA Paper 96-2661.
41. Heiser, W.H., and Pratt, D.T., et al., "Hypersonic Airbreathing Propulsion," AIAA Education Series, AIAA, 1994.
42. Gutmark, E.J., Schadow, K.C., and Yu, K.H., "Mixing Enhancement in Supersonic Free Shear Flows," Annual Review of Fluid Mechanics, Vol. 27, 1995, pp. 375-417.
43. Brown, G.L., and Roshko, A., "On Density Effects and Large Structure in Turbulent Mixing Layers," Journal of Fluid Mechanics, Vol. 64, part 4, pp. 775-816.
44. Slessor, M.D., Bond, C.L. and Dimotakis, P.E., "Turbulent Shear Layer Mixing at High Reynolds Numbers: Effects of Inflow Condition," Journal of Fluid Mechanics, Vol. 376, 1998, pp. 115-138.
45. Dimotakis, P.E., "The Mixing Transition in Turbulent Flows," Journal of Fluid Mechanics, Vol. 409, 2000, pp. 69-98.
46. Papamoschou, D., "Structure of the Compressible Turbulent Shear Layer," AIAA Journal, Vol. 29, No. 5, 1991. pp 680-681.

47. Papamoschou, D., and Roshko, A., “The Compressible Turbulent Shear Layer: an Experimental Study,” Journal of Fluid Mechanics, Vol. 197, 1988, pp. 453-477.

48. Kutschenreuter, P., “Supersonic Flow Combustors,” Scramjet Propulsion, Edited by Curran, E.T. and Murphy, S.N.B., Progress in Astronautics and Aeronautics Series, Vol 189, 2000, pp. 513-567.

49. Anderson, J. D., Jr., “Fundamentals of Aerodynamics,” McGraw-Hill, New York, 2007.

50. Orth, R. C., Schetz, J. A., and Billig, F. S., "The Interaction and Penetration of Gaseous Jets in Supersonic Flow," NASA CR-1386, July 1969.

51. Brown, G.L., and Roshko, A., “On Density Effects and Large Structure in Turbulent Mixing Layers,” Journal of Fluid Mechanics, Vol. 64, part 4, pp. 775-816.

52. Ben-Yakar, A., and Hanson, R.K., “Cavity Flame-Holders for Ignition and Flame Stabilization in Scramjets: An Overview,” Journal of Propulsion and Power, Vol. 17, No. 4, 2001, pp. 869-877.

53. Rogers, R.C., “Model of Transverse Fuel Injection in Supersonic Combustors,” AIAA Journal, Vol. 18, No. 3, 1979, pp. 294-301.

54. Gruber, M.R., Nejad, A.S., Chen, T.H., and Dutton, J.C., “Mixing and Penetration Studies of Sonic Jets in a Mach 2 Freestream,” Journal of Propulsion and Power, Vol. 11, No. 2, March-April 1995. pp. 315-323.

55. Yu, K.H., Wilson, K.J., and Schadow, K.C., “Effect of Flame-Holding Cavities on Supersonic-Combustion Performance,” Journal of Propulsion and Power, Vol.

17, No. 4, 2001, pp. 1288-1295.

56. Yu, K.H., Wilson, K.J., Smith, R.A., and Schadow, K.C., "Experimental Investigation on Dual-Purpose Cavity in Supersonic Reaction Flow," 36th Aerospace Sciences Meeting & Exhibit, AIAA 1998-0723, January 1998.
57. Yu, K.H., Wilson, K.J., and Schadow, K.C., "On the use of Combustor Wall Cavities for Mixing Enhancement," 3rd ASME/JSME Joint Fluids Engineering Conference, FEDSM 1999-7255, July 1999.
58. Jacobsen, L.S., Schetz, J.A., Ng, W.F., "Flowfield near a Multiport Injector Array in a Supersonic Flow," 34th AIAA/ASME/SAE/ASEE Joint Propulsion Conference, AIAA-1998-3126.
59. Rowan, S.A., Paull, A., "Performance of a Scramjet Combustor with Combined Normal and Tangential Fuel Injection," Journal of Propulsion and Power, Vol. 22, No. 6, 2006. pp. 1334-1338.
60. Rogers, R.C., Capriotti, D.P., and Guy, R.W., "Experimental Supersonic Combustion Research at NASA Langley," AIAA 98-2506, 1998.
61. Donohue, J.M., McDaniel, J.C., "Complete Three-Dimensional Multiparameter Mapping of a Supersonic Ramp Fuel Injector Flowfield," AIAA Journal, Vol. 34, No. 3, 1996, pp. 455-462.
62. Northam, G.B., Capriotti, D.P., Byington, C.S., and Greenberg, I., "Mach 2 and Mach 3 Mixing and Combustion in Scramjets," AIAA/ASME/SAE/ASEE 27th Joint Propulsion Conference, AIAA-91-2394, 1991.
63. Fuller, R.P., Wu, P.-K., Nejad, A.S., Schetz, J.A., "," AIAA/ASME/SAE/ASEE 32nd Joint Propulsion Conference and Exhibit, AIAA Paper 96-2661.

64. Schumacher, J., and Sislian, J.P., “Evaluation of Hypersonic Fuel/Air Mixing Performance by Cantilevered Ramp Injectors,” 36th AIAA/ASME/SAE/ASEE Joint Propulsion Conference and Exhibit, AIAA 2000-3468, 2000.

65. Montes, D. R., King, P. I., Gruber, M. R., Carter, C. D., Hsu, K., “Mixing Effects of Pylon-Aided Fuel Injection Located Upstream of a Flameholding Cavity in Supersonic Flow,” 41st AIAA/ASME/SAE/ASEE Joint Propulsion Conference & Exhibit, AIAA 2005-3913, July 2005.

66. Livingston, T., and Segal, C., “Penetration and Spreading of Liquid Jets in an External-Internal Compression Inlet,” AIAA Journal, Vol. 38 No.6, 2000, pp. 989-994.

67. Owens, M.G., Mullagiri, S., and Segal, C., “Effects of Fuel Preinjection on Mixing in Mach 1.6 Airflow,” Journal of Propulsion and Power, Vol. 17, No. 3, 2001, pp. 605-610.

68. Gouskov, O., Kopchenov, V., Lemkov, V. E., Vinogradov, V., and Waltrup, P.J., “Numerical Researches of Gaseous Fuel Pre-Injection in Hypersonic 3-D Inlet,” Journal of Propulsion and Power, Vol. 17, No. 6, 2001, pp. 1162-1169.

69. Mayinger, F., “Optical Measurements: Techniques and Applications,” Springer-Verlag, 1994, pp. 356.

70. Messersmith, N.L., Dutton, J.C., and Krier, H., “Experimental Investigation of Large Scale Structures in Compressible Mixing Layers,” at 29th Aerospace Sciences Meeting, AIAA 91-0244, January 1991.

71. Clemens, N.T., Mungal, M.G., Berger, T.E., and Vandsburger, U., “Visualizations of the Structure of the Turbulent Mixing Layer under Compressible Conditions,”

at 28th Aerospace Science Meetings, AIAA 90-0500, January 1990.

72. Clumpner, J.A., “Light Scattering from Ethyl Alcohol Droplets Formed by Homogeneous Nucleation,” Journal of Chemical Physics, Vol. 55, No. 10, pp. 5042-5045.